الجمهورية الجزائرية الديمقراطية الشعبية

وزارة التعليم العالي والبحث العلمي

Université Dr YAHIA FARES de Medea

Faculté des Sciences et de la Technologie

Département de Génie Électrique

THÈSE

En vue de l'obtention du diplôme de

Doctorat LMD en Electronique

Spécialité : Cryptographie et Protection du Contenu

Présenté par :

AZZOUZ Abdallah

THÈME :

Contribution à l'amélioration des systèmes intelligents de surveillance sécurisés des soins de santé basés sur l'IoT et l'intelligence artificielle

Soutenue publiquement le: 30/06/2024

Devant le jury composé de:

M. BOUHEDDA Mounir	Pr. Université de Medea	Président
M. BENGHERBIA Billel	MCA Université de Medea	Directeur de thèse
M. WIRA Patrice	Pr. Université de Haute Alsace	Co-directeur de thèse
M. RABEHI Abdelaziz	MCA Université de Djelfa	Examinateur
M. KARA Réda	MCA Université de Medea	Examinateur

Thèse préparée au sein du:

Laboratoire de recherche Systèmes Electroniques Avancés (LSEA)

Université de Medeia, Algérie

الجمهورية الجزائرية الديمقراطية الشعبية

وزارة التعليم العالي والبحث العلمي

University Dr YAHIA FARES of Medea

Faculty of Science and Technology

Department of Electrical Engineering

THESIS

In preparation for the graduation of

Doctoral LMD in Electronic

Specialty: Cryptography and Content Protection

Presented by:

AZZOUZ Abdallah

THEME:

Contribution to the improvement of intelligent secure healthcare surveillance systems based on IoT and artificial intelligence

Defended on: 06/30/2024

Before the jury composed of:

Mr. BOUHEDDA Mounir	Pr. University of Medea	President
Mr. BENGHERBIA Billel	MCA. University of Medea	Thesis Supervisor
Mr. WIRA Patrice	Pr. University of Haute Alsace	Thesis Co-supervisor
Mr. Rabehi Abdelaziz	MCA.University of Djelfa	Examiner
Mr. Kara Réda	MCA. University of Medea	Examiner

Thesis prepared within the:

Research Laboratory in Advanced Electronics Systems (LSEA)

University of Médéa, Algeria

Dedicated to my father, may his soul rest in peace

Acknowledgment

Primarily, this project owes its success to the exceptional support of my supervisor, Dr. Billel BENGHERBIA, Lecturer at the Faculty of Technology, Dr. Yahya Fares Medea University. I deeply admire his ability to identify captivating and pioneering avenues for scientific exploration, as well as his unwavering dedication to guiding and assisting individuals within his Research Laboratory in Advanced Electronics Systems (LSEA).

I'd also like to express my deep gratitude to the Doctoral Formation Committee for their consistent support during my years of training. I had the privilege of having Mr. Patrice WIRA as my assistant thesis supervisor. Pr. Patrice WIRA is a distinguished professor at the Institute of Research in Computer Science, Mathematics, Automation, and Signal (IRIMAS) at the University of Haute-Alsace, France.

This project would not have been possible without the in-depth discussions with colleagues in my laboratory. I eagerly anticipate the future endeavours of all of you and the collaborations that lie ahead!

I am profoundly thankful to the distinguished members of the panel for their invaluable oversight and contributions to this work. My deepest appreciation goes to Professor BOUHEDDA Mounir from the University of Medea, whose guidance as the Chairperson was instrumental; to Dr. Rabehi Abdelaziz, MCA at the University of Djelfa, whose keen insights and rigorous examination honed the sharpness of this study; and to Dr. Kara Réda, MCA at the University of Medea, whose expertise and thoughtful scrutiny have enriched the academic rigor of this thesis. Your collective wisdom has not only elevated the quality of my work but also inspired a broader scope of exploration and intellectual curiosity.

I would like to extend my sincere gratitude to Mr. Abdelhafid Tobbal, a PhD student at the LSEA laboratory, university of Medea, for his unwavering cooperation and dedicated assistance throughout these endeavours. His invaluable contributions and tireless efforts in the laboratory were instrumental in implementing the programs utilized in this thesis. I truly appreciate his commitment and support.

I would like to highlight the exceptional contributions of Dr. Nail ALAOUI, who has been by my side throughout my academic voyage, providing unwavering support during my

most challenging moments. Additionally, I am grateful for the invaluable guidance and wealth of experience shared by Dr. Abdelkerim SOUAHLIA, who generously offered his insights and knowledge.

I offer this work in tribute to all diligent individuals who burn with determination, like a candle, to light the way through the darkest hours of the night.

Last but not least, I want to express my gratitude to all those who have directly or indirectly contributed to the completion of this project. I thank each and every one of you sincerely.

Abstract

The integration of the Internet of Things (IoT) and Artificial Intelligence (AI) is revolutionising healthcare systems. This thesis examines their combined impact on enhancing healthcare surveillance, with a particular focus on Electrocardiogram (ECG) signal analysis. We introduce a novel approach that utilises Particle Swarm Optimisation (PSO) and Wavelet Transform (WT) to reduce noise in ECG signals and eliminate artifacts such as muscle activity, White Gaussian Noise (WGN), baseline wander, and Power Line Interference (PLI). Additionally, the Genetic Algorithm (GA) is employed alongside WT for similar purposes, demonstrating superior performance compared to current advanced noise reduction methods. The methods were validated using the widely recognized and publicly accessible MIT-BIH dataset.

Moreover, ECG signals are converted from 1D to 2D matrices, with features extracted via Discrete Wavelet Transform (2D-DWT). These matrices are then classified using Convolutional Neural Networks (CNNs) to accurately detect heart abnormalities.

Lastly, we implemented these methods on an ESP32 board to illustrate their practical application, highlighting the transformative potential of IoT and AI in medical diagnosis and healthcare monitoring.

Keywords: IoT, AI, Healthcare, ECG, WT, Noise, CNN, GA, PSO, Node-RED.

Résumé

L'intégration de l'Internet des objets (IoT) et de l'intelligence artificielle (AI) révolutionne les systèmes de santé. Cette thèse examine leur impact combiné sur l'amélioration de la surveillance médicale, avec un accent particulier sur l'analyse des signaux électrocardiographiques (ECG). Nous présentons une approche novatrice qui utilise l'optimisation par essaim de particules (PSO) et la transformation en ondelettes (WT) pour réduire le bruit dans les signaux ECG et éliminer les artefacts tels que l'activité musculaire, le bruit blanc gaussien (WGN), les dérives de la ligne de base et les interférences des lignes électriques (PLI). De plus, l'algorithme génétique (GA) est employé en combinaison avec la WT pour des objectifs similaires, démontrant une performance supérieure par rapport aux méthodes avancées actuelles de réduction de bruit. Les méthodes ont été validées à l'aide de l'ensemble de données MIT-BIH, largement reconnu et accessible au public.

En outre, les signaux ECG sont convertis de matrices 1D à des matrices 2D, avec des caractéristiques extraites via la transformation en ondelettes discrète (2D-DWT). Ces matrices sont ensuite classées à l'aide de réseaux de neurones convolutifs (CNN) pour détecter avec précision les anomalies cardiaques.

Enfin, nous avons implémenté ces méthodes sur une carte ESP32 pour illustrer leur application pratique, soulignant le potentiel transformateur de l'IoT et de l'IA dans le diagnostic médical et la surveillance de la santé.

Mots clés : IdO, IA, Soins de santé, ECG, Transformée d'Ondelettes, Bruit, Réseau de Neurones Convolutifs, AG, OEP, Node-RED.

ملخص

إن دمج إنترنت الأشياء (IoT) والذكاء الاصطناعي (AI) يحدث ثورة في أنظمة الرعاية الصحية. تدرس هذه الأطروحة تأثيرهما المشترك على تحسين مراقبة الرعاية الصحية، مع التركيز بشكل خاص على تحليل إشارة تخطيط القلب (ECG). نقدم نهجًا جديدًا يستخدم تحسين سرب الجسيمات (PSO) وتحويل المويجات (WT) لتقليل الضوضاء في إشارات تخطيط القلب وإزالة الضوضاء مثل نشاط العضلات والضوضاء البيضاء الغاوسية (WGN) والتجول الأساسي وتداخل خطوط الطاقة (PLI). بالإضافة إلى ذلك، يتم استخدام الخوارزمية الجينية (GA) جنبًا إلى جنب مع تحويل المويجات لأغراض مماثلة، مما يدل على الأداء المتفوق مقارنة بطرق الحد من الضوضاء المتقدمة الحالية. تم التحقق من صحة الطرق باستخدام مجموعة بيانات MIT-BIH المعروفة على نطاق واسع والتي يمكن الوصول إليها بسهولة.

علاوة على ذلك، يتم تحويل إشارات تخطيط القلب من مصفوفات أحادية الأبعاد إلى مصفوفات ثنائية الأبعاد، مع استخراج الميزات عبر تحويل الموجات المنفصلة (2D-DWT). يتم بعد ذلك تصنيف هذه المصفوفات باستخدام الشبكات العصبية التلافيفية (CNNs) للكشف بدقة عن امراض القلب.

وأخيرًا، قمنا بتنفيذ هذه الأساليب على لوحة ESP32 لتوضيح تطبيقها العملي، وتسليط الضوء على الإمكانات التحويلية لإنترنت الأشياء والذكاء الاصطناعي في التشخيص الطبي ومراقبة الرعاية الصحية.

كلمات مفتاحية : إنترنت الأشياء، الذكاء الاصطناعي، الرعاية الصحية، تخطيط القلب، التحويل المويجي، الضوضاء، الشبكات العصبية التلافيفية، الخوارزمية الجينية، تحسين سرب الجسيمات، نود-ريد

List of publications

The research work of this thesis has led to the following publications:

Journals

International Publications (WOS)

[1] A. Azzouz, B. Bengherbia, P. Wira, N. Alaoui, A. Souahlia, M. Maazouz, H. Hentabeli, An efficient ECG signals denoising technique based on the combination of particle swarm optimisation and wavelet transform, Heliyon. (2024) e26171. https://doi.org/https://doi.org/10.1016/j.heliyon.2024.e26171.

International Publications (Scopus)

[2] A. Azzouz, B. Bengherbia, P. Wira, N. Alaoui, A. Souahlia, The Effectiveness of Optimal Discrete Wavelet Transform Parameters Obtained Using the Genetic Algorithm for ECG Signal Denoising., Rev. d'Intelligence Artif. 37 (2023). https://doi.org/10.18280/ria.370602.

Conferences

International Conferences (IEEE):

[1] A. Azzouz, B. Bengherbia, P. Wira, N. Alaoui, A. Souahlia, ECG Signal Denoising Based on Wavelet Transform and Genetic Algorithm, in: 2023 Int. Conf. Adv. Electron. Control Commun. Syst., 2023: pp. 1–6. https://doi.org/10.1109/ICAECCS56710.2023.10105043.

Table of Contents

Acknowledgement
Table of Contents
List of Figures
List of Tables
Acronyms

Chapter I

General Introduction

I.1- Problematic 1
I.2- Motivation 2
I.2.1- Healthcare development 2
I.2.2- Healthcare 2
I.2.3- IOT in Healthcare 3
I.2.3.1- Remote Patient Monitoring 3
I.2.3.2- Smart Healthcare Devices 3
I.2.3.3- Predictive Analytics for Disease Prevention 3
I.2.3.4- Security and Privacy Challenges 4
I.2.4- AI in Healthcare 4
I.2.4.1- Diagnostic Assistance 4
I.2.4.2- Predictive Analytics 5
I.2.4.3- Robotic Surgyre 6
I.2.4.4- Virtual Health Assistants 6
I.3- Contributions 6
I.4- The organisation of the manuscript 7

Chapter II

An Introduction to Biomedical Signal Fundamentals and Filtering-Based Wavelet Transforms wavelet

II.1-Introduction 8
II.2- Biomedical signal basics 8
II.2.1- Phonocardiogram (PCG) 9
II.2.2 - Electroencephalogram (EEG) 10
II.2.3 - Electrocardiogram (ECG) 11

II.2.4 - ECG with predominant noises 13
II.2.4.1- ECG signal with PLI 14
II.2.4.2 - ECG signal with AWGN 14
II.2.4.3 - ECG signal with BW 14
II.3- Evolution of Wavelet Transform 15
II.3.1- The Fourier transform 15
II.3.2 - Short Time Fourier Transform (STFT) 16
II.3.3- Wavelets 17
II.4- Comparative Visualisation 20
II.5- Wavelet transforms 22
II.5.1 - Continuous WT (CoWT) 22
II.5.2 - Discrete wavelet transforms (DWT) 24
II.6- DWT implementation 24
II.6.1 - Multiresolution Analysis (MRA) 25
II.6.2 - Filter banks 27
II.6.2.1 - Down- and upsampling 27
II.6.2.2 - Perfect reconstruction 28
II.7- Conclusion 30

Chapter III

IoT and AI in Healthcare

III.1-Introduction 31
III.2- The Internet of Things in Healthcare 31
III.3- The data in the field of health 35
III.3.1- clinical data 35
III.3.2- Patient monitoring 36
III. 4- AI in Healthcare 38
III.4.1- The Metaheuristic Optimisation Algorithms 38
III.4.2- Optimisation Problem 39
III.4.2.1- Formulation of the optimisation problem 39
III.4.2.2- Classification of optimisation problems 40
III.4.2.3- Inspiration of Metaheuristics 41
III.4.3- Optimisation Algorithms for WT in biomedical signals 42
III.4.3.1- ECG noise reduction by WT 42
III.4.3.2- Genetic Algorithm (GA) 46
III.4.3.3- Particle Swarm Optimisation (PSO) 47
III.4.4- Disciplines and components of AI 49
III.4.4.1- Convolutional Neural Networks 52
III.4.4.2- The Convolution Operation 52

III.4.4.3- Characteristics of the Convolution Operation 55
III.4.4.4- Functions and Variants 57
III.4.4.5- Receptive Field Calculation 60
III.4.4.6- Convolutional Neural Network Architectures 60
III.4.4.7- A Basic CNN Architecture 61
III.4.4.8- Classification of images using deep learning 61
III.4.4.9- Measures to assess the performance of the classification system 62
III.5- Conclusion 64

Chapter IV

Experimental Results and Performance Evaluation

IV.1-Introduction 65
IV.2- PSO and WT for noise reduction in ECG signals 65
IV.2.1- Results and Discussions 72
III.2.1.1- AWGN Removal 72
IV.2.1.2- PLI removal 76
IV.3- ECG signal denoising using the proposed GA-WT 81
IV.3.1-AWGN noise removal 85
IV.3.1- PLI noise removal. 86
IV.4- CNN-based ECG Signal Classification 89
IV.4.1- Data Collection 89
IV.4.2- Data pre-processing. 90
IV.4.3- The Two Dimensions Discrete Wavelet Transform (2D DWT). 92
VI.4.3.1- Data segmentation. 94
VI.4.3.2- 2D-DWT test on a single signal. 95
VI.4.3.3- Display a sample image from CHF ARR NSR Class. 96
IV.4.4- Proposed CNN architecture 97
IV.4.5- CNN Model evaluation. 99
VI.4.5.1- Model with clean signal. 102
VI.4.5.2- Model with noisy signal. 103
VI.4.5.3- Model with denoised signal. 105
VI.4.5.4- Result and discussion. 106
VI.5- Conclusion 107

Chapter V

Design and Implementation of an IoT-based ECG signal Monitoring System

V.1- Introduction 108
V.2- Proposed approach for ECG signal monitoring..... 108
V.3- Experimental Circuit 109
V.3.1- Essential Components 110
V.3.1.1- The ESP32-S3 110
V.3.1.2- The AD8232 sensor 111
V.3.1.3- Jumper Wires and Breadboard 111
V.3.1.4- Connections 111
V.3.2- Software Implementation. 113
V.3.2.1- Programming the ESP32 113
V.3- Developed Electronic Board..... 113
V.4 -Hardware implementation. 114
V.4.1- Acquire and test data 114
V.4.2- TensorFlow Lite Model. 115
V.4.3- Node-RED Server. 115
V.4.3.1- Account Creation on FlowFuse for Node-RED Integration ... 115
V.4.3.2- Node-RED Editor 116
V.4.3.3 -Header..... 117
V.4.3.4- Palette. 117
V.4.3.5- Workspace. 118
V.4.3.6 -Sidebar 118
V.4.3.7- Setting Up Node-RED 118
V.4.3.8- Node-RED Workflow:..... 119
V.4.3.9 -Data Flow 120
V.5- Diagnostic results 120
V.6 -Conclusion 122

Chapter VI

General Conclusion and Perspectives

General Conclusion and perspectives 123
Bibliography 125

List of Figures

Figure I.1: Overview of the progress, challenges, and opportunities for AI in health..... 5
Figure I.2: Opportunities for the development of AI algorithms..... 5
Figure II.1: PCG signal acquisition during the recording process..... 10
Figure II.2: Acquisition of EEG signals during the recording procedure..... 11
Figure II.3: ECG signal acquisition during the recording process 12
Figure II.4: A one-cycle ECG..... 13
Figure II.5: (a) The original signal, (b) signal polluted with PLI 14
Figure II.6: (a) the original signal, (b) the signal with AWGN 14
Figure II.7: (a) clean ECG (b) ECG with BW. 15
Figure II.8: A left thumb fingerprint digitized by the FBI. The original image is on the left.19
Figure II.9: The time-frequency graph of the Fourier Transform. 21
Figure II.10: Time-frequency illustration of the STFT. 21
Figure II.11: Time-frequency illustration of the Wavelet Transform..... 22
Figure II.12: Morlet wavelet..... 22
Figure II.13: scaling and wavelet basis-spanned nested vector spaces..... 25
Figure II.14: Filter bank with two channels..... 27
Figure III.1: Aspects of the current city related to IoT..... 32
Figure III.2: Chronological history of the emergence of IoT 32
Figure III.3: IoT in healthcare frameworks 34
Figure III.4: Compliance tracking and related equipment..... 37
Figure III.5: ECG denoising process 43
Figure III.6: Details and approximations coefficients 44
Figure III.7: Hard and soft thresholding techniques..... 45
Figure III.8: Operation crossover 47
Figure III.9: Full representation of AI subsets 49
Figure III.10: Types of machine learning algorithms..... 50
Figure III.11: Representation of a mathematical model of artificial neurons 51
Figure III.12: 2D discrete convolution visualisation operation..... 53
Figure III.13: Original image with vertical and horizontal edge detection 54
Figure III.14: Exploring Non-linear Activation: Applying ReLu to Image Transformation . 54
Figure III.15: Multi-Filter Learning in Convolutional Neural Networks..... 56

List of Figures

Figure III.16: Organised Feature Maps in Convolutional Neural Networks 56

Figure III.17: Exploring Padding Operations in Convolutional Neural Networks..... 58

Figure III.18: Visualising Pooling Effects: Maximum Pooling with 2x2 Dimensions and Stride 2 58

Figure III.19: Stride Operation (Stride of 2)..... 59

Figure III.20: Unveiling CNN Architecture - From Convolutional Feature Extraction to Multilayer Perceptron Classification..... 61

Figure III.21: Deep Learning (CNN)..... 62

Figure IV.1: The proposed PSO-WT method 69

Figure IV.2: ECG denoising procedure 70

Figure IV.3: PSO-optimal WT parameter selection for ECG signal noise removal..... 71

Figure IV.4: (a) Illustration of the clean ECG signal (one sample), (b) ECG signal corrupted with noise at SNRinput = 10 dB, (c) Denoised ECG signal obtained using the proposed technique (φ = sym3, β = soft, λ = rigsure, L = 5, and ρ = sln) yielding SNRoutput = 18.24 dB 73

Figure IV.5: illustrates: (a) The relationship between SNRoutput and SNRinput, (b) PRD as a function of SNRinput, (c) MSE varying with SNRinput, (d) SNR Improvement relative to SNRinput, and (e) RMSE with respect to SNRinput 75

Figure IV.6: The improved performance of SNR and PRD for various denoising methods.. 76

Figure IV.7: (a) Original ECG signal, (b) ECG signal corrupted with noise at SNRinput = 10 dB, (c) Denoised ECG signal obtained using the proposed technique (φ = db2, β = hard, λ = rigsure, L = 3, and ρ = mln)..... 77

Figure IV.8: PLI reduction comparison, (a) SNRoutput (f = 50 Hz), (b) SNRoutput (f = 60Hz)..... 81

Figure IV.9: The proposed GA-WT method..... 82

Figure IV.10: (a) Clean, (b) noisy and (c) denoised ECG signal using GA-WT at SNRinput=10dB 84

Figure IV.11: The enhancement in SNR and PRD across different denoising methods 86

Figure IV.12: The three types of ECG signals: a) ARR, b) CHF, and c) NSR. 90

Figure IV.13: Signal segmentation. 91

Figure IV.14: Signal Reshaping into 2D Matrix..... 92

Figure IV.15: Single-level analysis filter bank for 2D DWT 93

Figure IV.16: Three-level decomposition of 2D-DWT. 93

List of Figures

Figure IV.17: Treatment with 2D-DWT and visualisation of the results 94
Figure IV.18: Signal segmentation example..... 95
Figure IV.19: Database distribution..... 95
Figure IV.20: 1D to 2D using 2D-DWT..... 96
Figure IV.21: CHF, ARR and NSR Class..... 96
Figure IV.22: Basic data distribution..... 97
Figure IV.23: Proposed 2D-CNN architecture 98
Figure IV.24: Dataset partitioning into training, validation and test 100
Figure IV.25: Accuracy and losses graphs 101
Figure IV.26: Confusion matrix for the clean signals..... 103
Figure IV.27: Confusion matrix for the noisy signals 104
Figure IV.28: Confusion matrix for the denoised signal 106
Figure V.1: Architecture of the proposed approach for ECG signal monitoring..... 108
Figure V.2: Experimental Circuit for ECG Signal Collection 109
Figure V.3: The ESP32-S3..... 110
Figure V.4: The AD8232 sensor 111
Figure V.5: Figure Jumper Wires..... 111
Figure V.6: IoT ECG Monitoring Breadboard..... 112
Figure V.7: Block diagram of the healthcare improvement system based on IoT and AI.... 112
Figure V.8: The Developed Electronic Board..... 114
Figure V.9: FlowFuse_account 116
Figure V.10: Node RED Editor..... 117
Figure V.11: Examples of nodes that can be found in Node-RED 118
Figure V.12: Workflow for ECG Signal Processing with ESP32 using Node-RED 119
Figure V.13: Example of a diagnostic for a person..... 121
Figure V.14: Detailed Steps and Execution Times 121

List of Tables

Table III.1: Data categories and different data elements 36

Table III.2: Wavelet denoising parameter ranges 44

Table III.3: Threshold selection rules 45

Table III.4: Rescaling methods for wavelet thresholding 46

Table III.5: Summary of commonly employed activation functions in neuron models 51

Table III.6: Evaluation measures 63

Table III.7: Confusion Matrix 64

Table VI.1: The PSO-derived optimal parameters for wavelet denoising of the tested signal 74

Table VI.2: Evaluation of ECG signal denoising efficacy across varying input SNR levels . 74

Table VI.3: Comparative analysis of PLI removal (f = 50Hz) from different ECG signals at different SNRinput levels, evaluated based on SNRoutput as averaged values over 20 segments 79

Table VI.4: Comparative analysis of PLI removal (f = 60Hz) from different ECG signals at different SNRinput levels, evaluated based on SNRoutput as averaged values over 20 segments. 80

Table VI.5: The efficacy of the standard and optimised DWT in terms of SNRout and PRD 83

Table VI.6: Assessing SNR improvements and PRD across varied input SNR values for each ECG record with 50 Hz PLI. 84

Table VI.7: Performance parameters for arrhythmia ECG records tainted by AWGN. 84

Table VI.8: Performance metrics for arrhythmia ECG records corrupted by AWGN 85

Table VI.9: The efficacy of removing PLI (at f = 50Hz) from different ECG signals with varied input SNR levels was assessed using averaged values over 20 segments. 88

Table VI.10: The efficacy of removing PLI (at f = 60Hz) from different ECG signals with varied input SNR levels was assessed using averaged values over 20 segments. 88

Table VI.11: Comparison of PSO-WT and GA-WT Methods 89

Table VI.12: description of the collected data 90

Table VI.13: Images distribution 95

Table VI.14: Analysis of the Layers in the proposed CNN Model 99

Table VI.15: Performance measurement values obtained for each fold of the proposed model 101

Table VI.16: Classification report (clean signals) 102

Table VI.17: Classification report (Noisy signals) 104

Table VI.18: Classification report (denoised signals) 105

Acronyms

1D	1-D One Dimensional
2D	2-D Two Dimensional
ADC	Analogue Digital Converter
AI	Artificial Intelligence
ARR	Cardiac Arrhythmia
BW	Baseline Wander
CHF	Congestive Heart Failure
CNN	Convolutional Neural Networks
CoAP	Constrained Application Protocol
DWT	Discrete Wavelet Transform
ECG	Electrocardiogram
EEG	Electroencephalogram
EHR	Electronic Health Records
ESP32	Espressif Systems Processor 32-bit
FPA	Flower Pollination Algorithm
FSD	Full-Scale Deflection
FT	Fourier Transform
FPGA	Field-Programmable Gate Array
GA	Genetic Algorithm
HSA	Harmony Search Algorithm
HTTP	Hyper Text Transfer Protocol
IHS	Information Processing Services
IoT	Internet of Things
LoRa	Long Range
M2M	Machine to Machine
MRA	Multi-Resolution Analysis
MRI	Magnetic Resonance Image
MQTT	Message Queuing Telemetry Transport
MLP	Multilayer Perceptron
MA	Muscular Movement Artefacts
MSE	Mean Squared Error

Acronyms

NB-IoT	Narrowband Internet of things
NSR	Normal Sinus Rhythm
PCG	Phonocardiogram
PRD	Percentage Root mean square Difference
PSO	Particle Swarm Optimisation
PLI	Power Line Interference
RFID	Radio Frequency Identification
RPM	Remote Patient Monitoring
RMSE	Root Mean Square Error
SIFT	Scale-Invariant Feature Transform
SNR	Signal-to-Noise Ratio
STFT	Short Time Fourier Transform
WT	Wavelet Transform
WGN	White Gaussian Noise
Wi-Fi	Wireless Fidelity

Chapter I

General introduction

I.1 Problematic

The landscape of healthcare monitoring has undergone significant transformation with the advent of technology, mainly through the integration of the Internet of Things (IoT) and Artificial Intelligence (AI) [1]. These advancements have paved the way for more efficient medical monitoring systems, enabling real-time tracking of patients' vital parameters [2]. In this research endeavour, we focus on enhancing a healthcare monitoring system based on IoT and AI, specifically focusing on denoising and classifying Electrocardiogram (ECG) signals [3][4]. Ensuring the reliability of medical monitoring systems is vital for accurate diagnosis. The quality of the captured signals is a significant factor in achieving this. ECG signals, in particular, are crucial for early detection of heart-related problems. However, these signals can be distorted by various noise sources, leading to incorrect diagnoses. The presence of noise in ECG signals can cause errors in classification and interpretation, which can put patients' lives at risk. In this context, the present research aims to significantly enhance the medical monitoring system by explicitly focusing on the denoising of ECG signals. Denoising ECG signals is paramount as it allows for more reliable and accurate information [5], thereby facilitating more precise classification of cardiac anomalies.

The denoising of ECG signals constitutes a critical step in medical monitoring and offers substantial benefits in early diagnosis and patient management [6]. Utilising advanced AI and signal processing techniques, our contribution centres around developing an effective denoising algorithm to improve the quality of ECG signals for more accurate classification of cardiac disorders.

This research is situated within the broader framework of the evolution of medical monitoring technologies, underscoring the importance of ensuring quality data for reliable diagnostics. By concentrating our efforts on the denoising of ECG signals, we aim to bolster practitioners' confidence and enhance patient care quality. The subsequent sections will delve into our research methodology, literature review, and results, providing a

comprehensive understanding of our contribution to improving healthcare monitoring systems [2] .

I.2 Motivation

I.2.1 Healthcare development

The development of healthcare spans centuries, evolving from ancient traditional practices to the establishment of modern medicine in the 19th and 20th centuries. Scientific breakthroughs, including the germ theory of disease and the development of vaccines and antibiotics, revolutionised medical practices [7] .

The post-World War II era witnessed the formation of universal healthcare systems, such as the UK's NHS. At the same time, in the latter half of the 20th century, they brought technological advancements like medical imaging and digital health integration. The 21st century emphasizes patient-centred care, global health initiatives, and the challenges of an ageing population and chronic diseases. Throughout this history, healthcare has adapted to societal changes, technological innovations, and the understanding of holistic health, with ongoing efforts to improve patient outcomes and address emerging global health challenges [1].

I.2.2 Healthcare

Healthcare refers to the organised provision of medical services to individuals or communities to maintain, diagnose, treat, and prevent illness or injury. It encompasses a broad spectrum of services, including primary care, specialised medical treatments, surgery, preventive measures, and health promotion. The development of healthcare involves a historical progression from ancient traditional practices to modern, evidence-based medicine. Over time, healthcare systems have evolved to include advancements such as medical technologies, pharmaceuticals, and digital health solutions. Contemporary healthcare also emphasises patient-centered care, public health initiatives, and global health efforts to address health disparities and promote well-being. The ongoing development of healthcare is driven by scientific research, technological innovation, and a commitment to improving the quality and accessibility of medical services for individuals and communities [7].

I.2.3 IOT in Healthcare

Integrating the IoT into healthcare has emerged as a transformative force, revolutionising how medical services are delivered, monitored, and managed. IoT in healthcare involves the interconnection of medical devices, wearables, sensors, and other healthcare-related systems through a network, enabling seamless data exchange and facilitating enhanced patient care. This convergence of technology holds immense potential for improving efficiency, reducing costs, and ultimately advancing the quality of healthcare services [8].

I.2.3.1 Remote Patient Monitoring:

IoT-enabled remote patient monitoring is a crucial application in the healthcare industry. By using wearable sensors, healthcare providers can consistently collect and transmit real-time health data. This enables proactive and remote monitoring of patients with chronic conditions, leading to timely intervention and individualised care plans. Additionally, remote patient monitoring improves patient outcomes and reduces the burden on healthcare facilities [9].

I.2.3.2 Smart Healthcare Devices:

IoT has given rise to many intelligent healthcare devices that monitor various health parameters. From smart glucose meters and blood pressure monitors to connected inhalers, these devices empower individuals to manage their health actively. The data generated by these devices can be seamlessly integrated into Electronic Health Records (EHRs), providing a comprehensive view of a patient's health status[8].

I.2.3.3 Predictive Analytics for Disease Prevention

The continuous data streams generated by IoT devices in healthcare contribute to accumulating vast datasets. Through the application of advanced analytics and machine learning algorithms, healthcare professionals can leverage this data to identify patterns, predict disease outbreaks, and implement preventive measures. This proactive approach to healthcare holds promise for reducing the incidence of certain diseases and minimising public health risks [10].

I.2.3.4 Security and Privacy Challenges

While the integration of IoT in healthcare offers numerous benefits, it also raises concerns regarding data security and patient privacy. Safeguarding sensitive health information from cyber threats and ensuring secure communication between devices are critical challenges that healthcare organisations must address to maintain the trust of patients and comply with regulatory standards. To conclude, the integration of IoT in healthcare represents a significant change in the industry. It provides unparalleled opportunities to improve patient care, optimise operations, and advance medical research. However, as technology progresses, it is crucial to address security and privacy concerns to unlock the full potential of IoT in revolutionising healthcare [11].

I.2.4 AI in Healthcare

AI has transformed the healthcare sector, offering innovative solutions to improve patient care, diagnostics, treatment, and overall operational efficiency [12]. AI applications in healthcare include:

I.2.4.1 Diagnostic Assistance

AI algorithms are pivotal in meticulously analysing various medical imaging data types, including X-rays, MRIs (Magnetic Resonance Image), and CT (Computed Tomography) scans. These algorithms employ sophisticated pattern recognition and machine learning techniques to assist healthcare professionals in detecting and diagnosing diseases. By scrutinising intricate details within medical images that may be imperceptible to the human eye, AI enhances the precision and efficiency of diagnostic processes. This contributes to more accurate and timely diagnoses and enables clinicians to identify subtle anomalies or early-stage conditions that might go unnoticed through traditional methods. The integration of AI in diagnostic assistance represents a paradigm shift, augmenting the diagnostic capabilities of healthcare practitioners and significantly impacting patient outcomes through improved accuracy and speed in identifying various medical conditions [13].

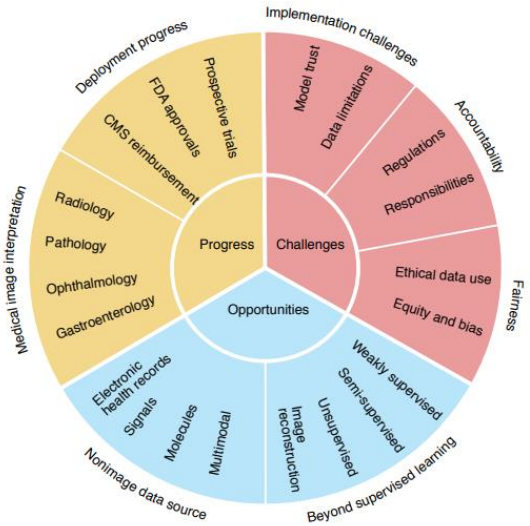


Figure I.1: Overview of the progress, challenges, and opportunities for AI in health [14]

I.2.4.2 Predictive Analytics

AI harnesses the power of patient data analysis to uncover intricate patterns and anticipate potential health issues before they manifest clinically. By scrutinising vast patient information datasets, including medical histories, genetic markers, lifestyle factors, and treatment responses, AI algorithms discern patterns that may indicate an increased risk of specific diseases or health deterioration. This proactive approach empowers healthcare providers to intervene early in the progression of illnesses, implementing preventive measures and personalised interventions. The ability to predict health issues before symptomatic manifestation enhances patient outcomes and reduces the burden on the healthcare system by focusing resources on preventive strategies. Through the application of Predictive Analytics, AI is revolutionising healthcare by ushering in a new era of personalised and pre-emptive medical care, were timely interventions [15].

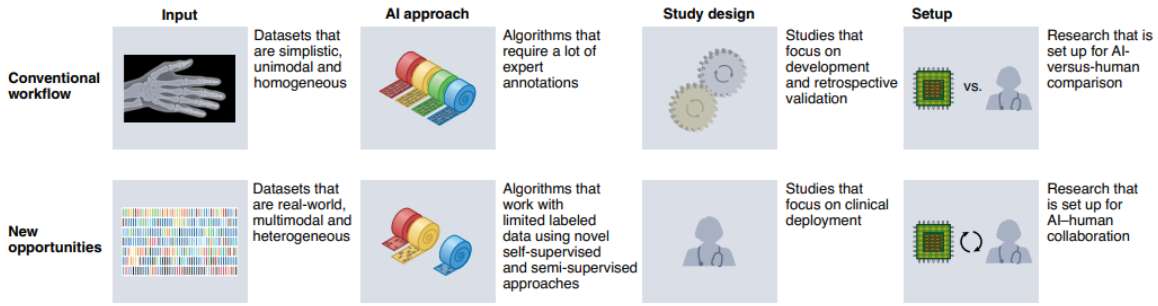


Figure I.2: Opportunities for the development of AI algorithms [14]

I.2.4.3 Robotic Surgyre

AI-driven robotic systems play a pivotal role in aiding surgeons in executing intricate procedures with precision. These systems augment the surgeon's skills, offering heightened accuracy and improved capabilities throughout the surgical process [7].

I.2.4.4 Virtual Health Assistants:

AI-driven virtual assistants and chatbots can provide patients with information, answer queries, and offer essential medical advice. This enhances patient engagement and accessibility to healthcare services. While AI presents immense opportunities in healthcare, ethical considerations, data privacy, and the need for regulatory frameworks are crucial aspects that need careful attention to ensure responsible and effective integration into the healthcare ecosystem [7].

I.3 Contributions

This thesis work aims to advance healthcare monitoring systems, integrating the IoT and AI specifically, my focus is enhancing ECG signal processing through advanced denoising techniques. The significance of this contribution lies in addressing the critical challenge of noise within ECG signals, which can significantly impact the accuracy of cardiac anomaly detection and classification. By developing and implementing robust denoising algorithms, the research aims to fortify the reliability of ECG signals, ensuring a more precise and dependable foundation for healthcare monitoring. This endeavour holds the potential to elevate diagnostic accuracy, facilitate early detection of cardiac disorders, and ultimately contribute to the overall improvement of patient care within the evolving landscape of healthcare technologies. The significant contributions are as follows:

- Develop innovative denoising techniques explicitly tailored for ECG signals. Our approach incorporates advanced signal processing and AI algorithms, combining the Particle Swarm Optimisation (PSO) algorithm with the Wavelet Transform (WT). Additionally, we employ the Genetic Algorithm (GA) in conjunction with the WT to extract optimal WT parameters, creating a hybrid system. The primary objective of these techniques is to reduce noise interference proficiently, consequently enhancing the accuracy and reliability of ECG data for subsequent analysis.

- The thesis substantially improves healthcare monitoring systems by focusing on denoising ECG signals. The developed techniques aim to elevate the accuracy of cardiac anomaly detection within these systems, facilitate more reliable diagnoses, and contribute to the overall efficacy of healthcare monitoring.
- Implement an IoT-based ECG monitoring system using ESP32 and deep learning Convolutional Neural Networks (CNN)

I.4 The organisation of the manuscript

This thesis is organised into six chapters. Following this general introduction, Chapter II is dedicated to the fundamentals of biomedical signals. The first part introduces biomedical signal fundamentals, while the second focuses on filtering-based WT.

Chapter III presents a comprehensive overview of IoT and AI in healthcare, highlighting the state-of-the-art developments in this domain.

Chapter IV reviews the project's tools, focusing on their role in enhancing ECG signal analysis and diagnostic precision through advanced denoising and classification techniques.

Chapter VI reveals the implementation of an IoT-based ECG monitoring system, incorporating PSO-WT for signal denoising and DWT-2D for feature extraction via the ESP32 microcontroller. It details how the AD8232 ECG sensor is integrated with the Node-RED platform, showcasing the system configuration and the effective combination of sophisticated algorithms with durable hardware. This method highlights the effectiveness of our 2D-CNN model on the ESP32 in enhancing ECG signal analysis and monitoring.

Finally, we conclude this document with a general conclusion and the perspectives that open up in the field of e-healthcare.

Chapter II

An Introduction to Biomedical Signal Fundamentals and Filtering-Based Wavelet Transforms

II.1 Introduction

Biomedical signals are indispensable in the realm of healthcare, offering profound insights into the physiological functions within the human body. These signals, which are captured using specialised medical equipment, are crucial for diagnosing, monitoring, and understanding a broad spectrum of medical conditions. Highlighting their importance, types, and applications in healthcare and medical research, biomedical signals like the Electrocardiogram (ECG), Electroencephalogram (EEG), and Phonocardiogram (PCG) stand out for their utility in providing essential data for patient care and scientific inquiry [16]. Delving into the fundamentals reveals that understanding these signals encompasses their generation, acquisition, and interpretation processes, emphasising the critical analysis techniques that unravel the physiological insights contained within. Signal characteristics such as amplitude, frequency, and duration are scrutinised for deviations from normal patterns, aiding in the identification of potential health issues [17] [18]. Furthermore, biomedical signals are not just diagnostic tools but also pivotal in medical research, driving the exploration of bodily functions, the innovation of monitoring technologies, and the evaluation of treatment outcomes. In this context, filtering-based Wavelet Transform (WT) emerges as a significant technique in biomedical signal processing, providing a nuanced approach to dissecting complex physiological data through multi-resolution analysis, thus amplifying the diagnostic and research utility of these signals [19].

II.2 Biomedical signal basics

Biomedical signals play a pivotal role in the realms of healthcare and medical research, offering invaluable insights into the intricate physiological workings of the human body. These biomedical signals provide a window into the body's inner workings and are

indispensable for healthcare professionals, researchers, and clinicians in their efforts to understand, diagnose, and treat various medical conditions. Some of the most frequently encountered biomedical signals include PCG, EEG, and ECG [16].

II.2.1 Phonocardiogram (PCG)

The Phonocardiogram, often abbreviated as PCG, is a graphical representation of the sounds produced by the heart, particularly the heart's mechanical activity and the flow of blood within its chambers and vessels. This diagnostic tool is primarily used in cardiology to analyse and interpret heart sounds, enabling healthcare professionals to detect abnormalities or irregularities in the heart's functioning [20].

The PCG is obtained by placing specialised microphones or sensors, known as phonocardiography sensors or stethoscopes, on the chest to capture the acoustic signals generated during the cardiac cycle. These signals consist of a series of heart sounds, including the familiar "lub-dub" of the heartbeat, as well as additional sounds like murmurs and clicks. Each of these sounds corresponds to specific events in the cardiac cycle and can provide critical information about the heart's condition [21].

Interpreting a PCG involves analysing the timing, intensity, and frequency characteristics of the recorded sounds. Healthcare professionals use this information to assess the heart's overall health, identify valve abnormalities, detect murmurs or irregular rhythms, and monitor the effectiveness of treatments or interventions [22].

Overall, the PCG is a valuable tool in cardiology, aiding in the diagnosis and management of various cardiac conditions and contributing to the comprehensive assessment of cardiac health. Researchers and clinicians continue to explore its potential applications in both clinical practice and medical research.

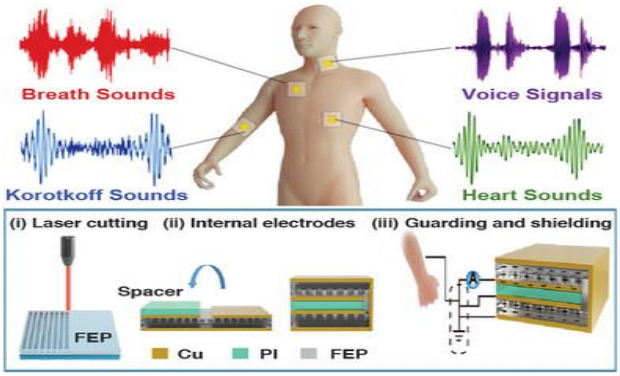


Figure II.1: PCG signal acquisition during the recording process

II.2.2 Electroencephalogram (EEG)

An Electroencephalogram, commonly referred to as EEG, is a non-invasive neurophysiological test used to measure and record the electrical activity of the brain. This diagnostic technique is essential in neurology, neuroscience, and clinical medicine to study brain function, detect abnormalities, and diagnose various neurological conditions [23].

The EEG procedure involves placing a set of electrodes on the scalp, which are connected to an EEG machine. These electrodes capture the electrical signals generated by the brain's neurons. These signals, called brainwaves, represent the synchronised electrical activity of groups of neurons firing together [24].

EEG recordings typically display several types of brainwaves, each associated with different mental states and activities. The main categories of brainwaves include:

1. **Delta (δ) Waves**: These slow, high-amplitude waves are associated with deep sleep and certain brain disorders.
2. **Theta (θ) Waves**: Theta waves are present during light sleep, relaxation, and the early stages of deep sleep.
3. **Alpha (α) Waves**: Alpha waves occur when a person is awake but relaxed and with their eyes closed. They are often observed during meditation and relaxation.
4. **Beta (β) Waves**: Beta waves are associated with alertness, problem-solving, and active mental engagement.
5. **Gamma (γ) Waves**: These high-frequency waves are linked to higher cognitive functions, perception, and conscious awareness.

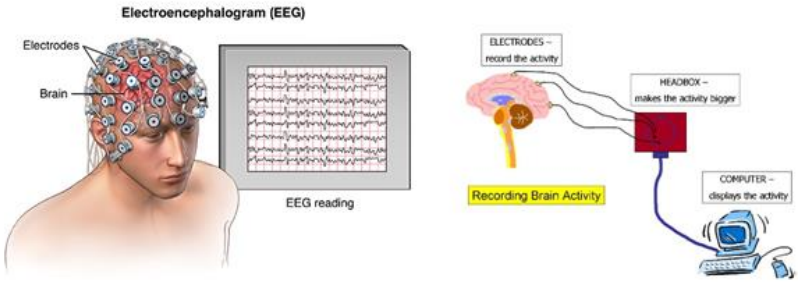


Figure II.2: Acquisition of EEG signals during the recording procedure

Clinicians and neurologists use EEG recordings to diagnose and monitor various neurological conditions, such as epilepsy, sleep disorders, brain tumors, and cognitive impairments. Abnormal patterns or spikes in EEG readings can provide valuable insights into the presence and localisation of brain abnormalities [25].

EEG also plays a crucial role in neuroscientific research, where it helps scientists better understand brain function, cognitive processes, and how the brain responds to stimuli or tasks. Advances in EEG technology, including portable and wearable EEG devices, have expanded its applications beyond clinical settings into fields such as human-computer interaction, brain-computer interfaces, and mental state assessment [26].

In summary, EEG is a powerful tool for studying brain activity, diagnosing neurological disorders, and advancing our understanding of the human brain's complex functions. It continues to be an invaluable asset in both clinical practice and scientific research.

II.2.3 Electrocardiogram (ECG)

Electrocardiogram (ECG) signals, often referred to as ECG tracings or ECG waveforms, are graphical representations of the electrical activity of the heart over time. These signals are recorded using an electrocardiograph, which detects and amplifies the minute electrical changes on the skin's surface generated by the heart's depolarisation and repolarisation during each cardiac cycle [27].



Figure II.3: ECG signal acquisition during the recording process

ECG signals are composed of a sequence of characteristic waves, segments, and intervals, which can be used to identify any anomalies in a subject. A standard ECG signal typically exhibits amplitude and frequency ranges of 10 µV to 5 mV and 0.05 to 100 Hz, respectively [28]. Accurate data capture from each component of an ECG enables assessment of the physical state of the heart. [29–31], with each component corresponding to a specific event in the cardiac cycle. The crucial components of ECG signals include:

- **P-Wave:** Represents atrial depolarisation, signifying the contraction of the atria.
- **QRS Complex:** Indicates ventricular depolarisation, marking the contraction of the ventricles.
- **T-Wave:** Represents ventricular repolarisation, signifying the relaxation of the ventricles.
- **PR Interval:** Measures the time from atrial depolarisation to ventricular depolarisation.
- **QT Interval:** Measures the time it takes for ventricular depolarisation and repolarisation.
- **ST Segment:** A segment between the QRS complex and the T-wave that reflects the period when the ventricles are depolarised but not yet repolarised.

ECG signals are crucial for diagnosing various cardiac conditions, evaluating heart rate and rhythm, and monitoring the effects of medications or interventions. Healthcare professionals, particularly cardiologists and electrocardiography technicians, analyse ECG signals to assess the heart's electrical health and identify any abnormalities or irregularities [32].

The interpretation of ECG signals requires a deep understanding of cardiac physiology and the ability to recognise patterns and deviations from normal. ECGs are

routinely used in clinical settings, including hospitals, clinics, and emergency rooms, to evaluate patients with chest pain, arrhythmias, and other cardiac symptoms [33].

Moreover, advancements in technology have led to the development of portable ECG devices and wearable monitors, allowing for continuous heart monitoring and remote healthcare. This has revolutionised the field by enabling early detection and prompt management of heart-related issues [34]. In brief, ECG signals play a crucial role in cardiology and healthcare by furnishing significant insights into the heart's electrical functions, thus aiding in the identification and management of various cardiac ailments.

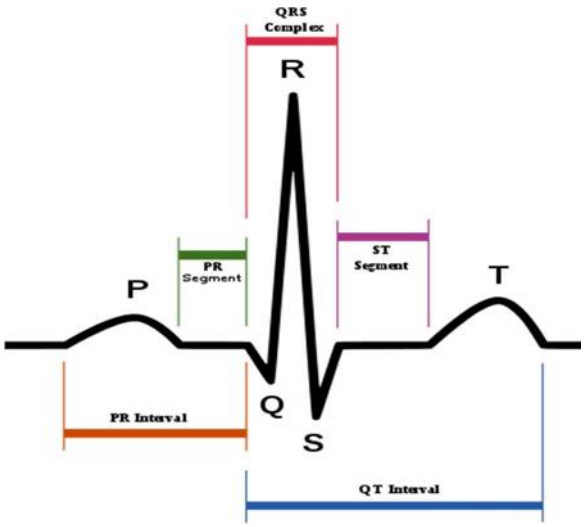


Figure II.4: A one-cycle ECG [35]

II.2.4 ECG with predominant noises

The disturbances and noises occur within the spectral range of interest and primarily exhibit morphological features resembling either the inherent characteristics of the ECG or specific characteristics related to diseases. Here's a brief overview of the main ECG noises [36]:

The introduction of synchronised noise components by Power line interference (PLI), which frequently originates from external sources like electrical devices, has the potential to result in misinterpretation or incorrect diagnosis. Conversely, AWGN, which is Gaussian-distributed random noise, obscures more minute ECG signal details. Baseline Wander (BW), which commonly transpires within the frequency range of 0.15 Hz to 0.3 Hz, confers rhythmic oscillations to the baseline and obstructs critical waveform components, thereby

impeding the precise diagnosis of cardiac conditions. Muscular movement artefacts, which are distinguished by high-frequency noise (usually 25-50 Hz and greater), become apparent in the form of abrupt bursts and interference. These artefacts introduce complexity into the process of interpreting the fundamental cardiac electrical activity.

II.2.4.1 ECG signal with PLI

PLI noises are caused by inductive and capacitive couplings of 50/60 Hz power lines during ECG signal acquisition, as illustrated in Figure II.5. At an input SNR of 10 dB, record number 100 from the MIT-BIH database became contaminated with noise[3].

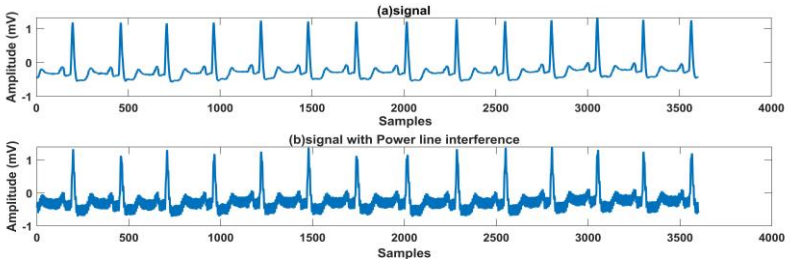


Figure II.5: (a) The clean signal, (b) signal contaminated with PLI [37]

II.2.4.2 ECG signal with AWGN

As illustrated in Figure II.6, channel noise is introduced when ECG signals are transmitted over a channel characterised by feeble channel conditions, such as AWGN [38], At an SNR input of 10 dB, the record number 100 became contaminated with noise.

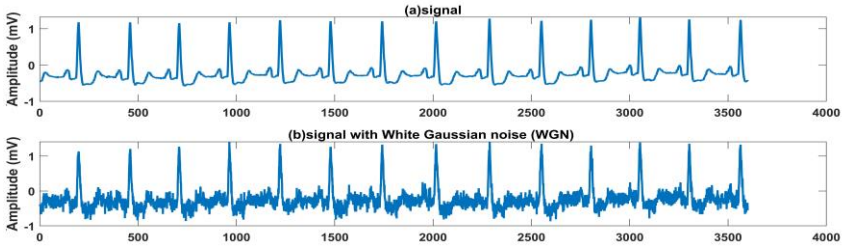


Figure II.6: (a) the original signal, (b) the signal with AWGN [37]

II.2.4.3 ECG signal with BW

To properly analyse an ECG with baseline wander, it is important to first identify the frequency and extent of the baseline drift. This can be done visually by examining the ECG waveform or by using digital signal, processing techniques to filter out the baseline wander [39]. Overall, interpreting an ECG with baseline wander requires careful analysis and consideration of the extent and frequency of the drift, as well as the potential impact on the

clinical interpretation of the ECG. Figure II.7(a) shows a representation of the clean ECG signal from the MIT-BIH database, while Figure (b) shows the corrupted signal with BW.

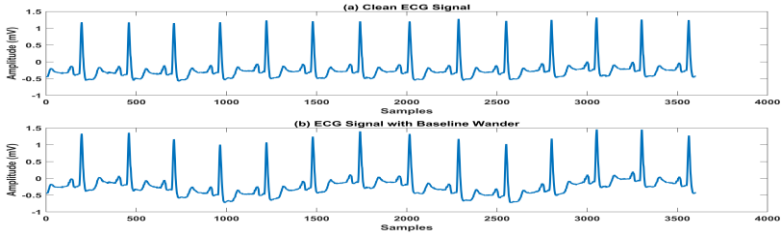


Figure II.7: (a) clean ECG (b) ECG with BW

II.3 Evolution of Wavelet Transform

For a considerable period, traditional signal processing focused on defining signals and creating operators that maintained signal properties consistently over time and space. However, the most significant data often lies within transient signals rather than in stable ones. In the discussion below, we'll explore the development of the WT, starting from the foundation provided by the Transform of Fourier (FT).

II.3.1 The Fourier transform

In 1807, Joseph Fourier, a French mathematician, introduced the Fourier transform (FT), which is perhaps the most commonly employed technique for signal analysis. Fourier's insight was that a periodic function could be expressed as an infinite series of complex exponentials. Over time, this idea was broadened to include functions that are not periodic, and it was further extended to include signals that occur in discrete time.

The FT breaks down the signal into a set of trigonometric orthogonal functions. Equation (1.1) defines the FT for a continuous signal x(t). The resulting transformed signal, denoted as $X_{FT}(f)$, provides a comprehensive representation of the frequency content within the time for signal x(t) [40]. The initial signal will be rebuilt by employing the inverse FT, as indicated in Equation (1.2).

$$X_{FT}(f) = \int_{-\infty}^{\infty} x(t) e^{-j2\pi ft} dt \tag{1.1}$$

$$x(t) = \int_{-\infty}^{\infty} X_{FT}(f) e^{j2\pi ft} df \tag{1.2}$$

Applying these equations makes it feasible to convert a signal x(t) into the frequency domain and then revert it back. The execution of the FT, and subsequent reconstruction becomes achievable when the specified Dirichlet conditions, as indicated in the referenced literature [40,41]:

- The integral $\int_{-\infty}^{\infty} |x(t)|dt$ should exist, meaning that the FT $X_{FT} \rightarrow 0\ as\ |f| \rightarrow \infty$.
- The FT $X_{FT}(f)$ and the time signals x(t) are only one-valued meaning that no two values exist at the same frequency f or time instant t.
- Signal x(t) as well as its corresponding FT $X_{FT}(f)$ demonstrate piece-wise continuity. In simpler terms, this means that the signal has points of discontinuity, but at these points, the value of the signal must be equal to the mean of the surrounding points. It is equally crucial to emphasise that the magnitude of the discontinuity must be limited, and the quantity of discontinuity should not escalate endlessly within a bounded time, as described in the literature [40].
- A sufficient but not necessary condition for x(t) and $X_{FT}(f)$ to have upper and lower bounds is presented. However, this condition is not applicable to certain functions like Dirac's δ-function.

II.3.2 Short Time Fourier Transform (STFT)

To meticulously observe the dynamic evolution of a signal's frequency characteristics, we adopt a method of partitioning the signal into discrete segments and thoroughly examining the spectrum of each constituent. This foundational principle serves as the underpinning for the STFT, initially introduced by Gabor in 1946 [42] and subsequently reinterpreted as a filter bank by J.B. Allen in 1977 [43]. In the calculation of the STFT, a judicious selection of windowing function is applied to the original signal, maintaining a non-zero value for a specifically brief duration. Following this, we meticulously execute the Fourier Transform on the resulting signal. The consequence is a comprehensive two-dimensional representation of the signal's dynamic behaviour, which can be precisely articulated mathematically as:

$$\mathrm{STFT}_x(\tau, f) = \int_{-\infty}^{\infty} x(t)\mathrm{g}^*(t-\tau)e^{-j2\pi ft}dt \qquad (1.3)$$

In this representation, the function g(t) is the chosen windowing function, commonly adopting forms such as the Hann window or a Gaussian function centred at zero. In contrast,

x(t) denotes the signal under scrutiny. This formula can be conceptualised as evaluating the signal by applying either a time-sliding window or a frequency-sliding band-pass filter.

Notably, a unique characteristic of this transformation is the consistent maintenance of the window's length throughout the entire analysis. This steadfastness ensures a reliable resolution in both the time and frequency domains, allowing for a detailed examination of the signal's characteristics and facilitating the identification of nuanced frequency components [44].

II.3.3 Wavelets

Historique

In 1909, wavelets were introduced in an addendum to a Haar's thesis. The Haar wavelet possesses the characteristic of compact support, indicating that it becomes zero beyond a defined interval. However, a drawback of Haar wavelets lies in their lack of continuous differentiability, thereby imposing constraints on their applicability [45].

During the 1930s, various independent research groups investigated the portrayal of functions by utilising basis functions that vary in scale. Understanding the principles behind basis functions and scale-varying basis functions is essential for comprehending wavelets. The accompanying sidebar offers a brief supplementary lesson [46].

By utilising a basis function that varies in scale, precisely the Haar basis function (which will be elaborated upon later), Paul Levy, a physicist from the 1930s, explored Brownian motion, a form of random signal (1.4). Levy determined that the Haar basis function excelled over Fourier basis functions when scrutinising detailed aspects within Brownian motion, particularly those of smaller scale [47].

In the 1930s, Littlewood, Paley, and Stein undertook a research initiative focused on calculating the energy of a function f(x) and its energy:

$$\text{energy} = \frac{1}{2}\int_0^{2\pi} |f(x)|^2 dx \tag{1.4}$$

The calculation yielded varied outcomes based on whether the energy was concentrated at specific points or spread across a broader range. This variation in results raised concerns among scientists, suggesting a potential lack of energy conservation. In

response, researchers identified a function capable of scaling and conserving energy during functional energy computations. This discovery contributed to David Marr obtaining an efficient algorithm for numeric image processing with wavelets in the first years of the 1980s [48].

From 1960 to 1980, Guido Weiss and Ronald R. Coifman delved into analysing fundamental components within a function space called atoms. Their objective was to identify atoms associated with a general function and elucidate the "assembly rules", enabling the reconstruction of all elements within the function space using these atoms. In 1980, physicist Grossman and engineer Morlet extended the concept of wavelets within the realm of quantum physics. These researchers presented a conceptual framework for understanding wavelets rooted in physical intuition [45].

In 1981, Jean Morlet, a petroleum engineer affiliated with Elf-Aquitaine, discovers a technique to break down seismic signals into entities he refers to as "wavelets of consistent form." Seeking validation for this method, he enlists the assistance of quantum physicist Alex Grossmann.

In 1984, Morlet and Grossmann collaborated on pioneering work, introducing the term "wavelet" into the mathematical vocabulary for the first time. This groundbreaking contribution marked a pivotal moment in the field, establishing a foundation for exploring and applying wavelet theory across various mathematical and scientific disciplines.

In 1986, Stéphane Mallat, a doctoral candidate in computer vision under Meyer, connected wavelet theory with subband coding and quadrature mirror filters in image processing. Together with Meyer, Mallat demonstrated that wavelets are inherent in the multiresolution analysis of signals at various scales.

Mallat's contributions simplified wavelet analysis, eliminating the need for knowledge of the mother wavelet formula. The process became a series of straightforward operations involving averaging pixel groups and taking differences. Furthermore, electrical engineers were able to comprehend the concepts of wavelets better through the incorporation of standard terms such as "the filters," "the high frequencies," and "the low frequencies."

In 1987, Ingrid Daubechies introduced a groundbreaking wavelet class during her time at the Courant Institute and AT&T Bell Laboratories. Unlike Meyer's orthogonal

wavelets, Daubechies' discovery could be implemented using straightforward digital filtering, employing short digital filters. In contrast to Haar wavelets, these novel wavelets were introduced to signal processors without requiring abrupt transitions. As a result, they offered an optimal instrument for decomposing digital data into scale contributions by integrating the ideas of Daubechies and Mallat, a straightforward and orthogonal transformation materialised, which could be efficiently computed using contemporary digital computers [45].

Daubechies wavelets exhibit intriguing features, displaying intimate connections alongside fractal theory. When magnified, their graph reveals characteristic jagged wiggles at any level of magnification, showcasing an intricate complexity that lacks a simple formula. Despite their asymmetry and ungainliness, akin to something nineteenth-century mathematicians might have found unsettling, these wavelets are esteemed for their functionality. Like the Model-T Ford, they are appreciated for their effective performance. Daubechies wavelets transform theoretical concepts into practical tools easily programmed and utilised by scientists with minimal mathematical training.

In 1990, at Stanford University, David Donoho and Iain Johnstone applied wavelets to enhance images by reducing noise, resulting in sharper versions than the original images.

In 1993, in collaboration with the National Institute of Standards and Technology, Los Alamos National Laboratory, commercial vendors, and criminal justice communities, the Criminal Justice Information Services Division of the FBI established standards for digitising and compressing fingerprints [48].



Figure II.8: A left thumb fingerprint digitized by the FBI. The original image is on the left [45].

Subdivision surfaces debuted in the cinematic realm through the 1998 film A Bug's Life, supplanting the less sophisticated NURBs (non-uniform rational B splines) technique employed in the original Toy Story film of 1995. In the subsequent 1999 film Toy Story 2, NURBs and subdivision techniques coexisted. The original Toy Story characters retained their NURBs form, while the newly introduced characters embraced the subdivision method. The prospective application of subdivision surfaces holds promise for the video game industry, potentially addressing the prevalent issue of the current blocky appearance in graphics.

Meanwhile, in the realm of theory, mathematicians continue the quest for improved wavelet types suited for two-dimensional and three-dimensional images. While standard wavelet methods excel at capturing edges, their pixel-by-pixel approach could be more efficient for representing potentially simple curves or lines. Stanford University's David Donoho and Emmanuel Candès have introduced a novel wavelet class known as "ridgelets," explicitly designed to identify discontinuities along a line. Concurrently, other researchers explore "multiwavelets," capable of encoding multiple signals traversing the same line, as observed in colour images transmitting three colour values (red, green, and blue) simultaneously. When questioned about the significance of mathematics, mathematicians frequently highlight that concepts devised to address pure mathematical challenges can yield unforeseen applications in the future. However, the narrative of wavelets presents a more intricate and intriguing scenario. In this instance, targeted applied research gave rise to a novel theoretical synthesis, revealing new applications to scientists.

II.4 Comparative Visualisation

In the upcoming discussion, we will visually compare the time-frequency resolution cells of the three previously mentioned transforms. Figure II.9 illustrates the FT, showcasing its excellent frequency localisation and the absence of time localisation in this particular transformation.

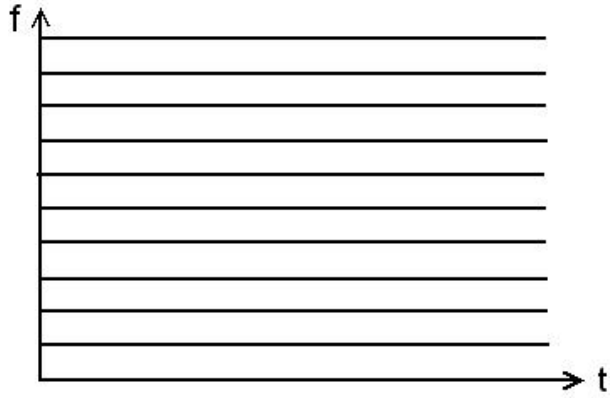
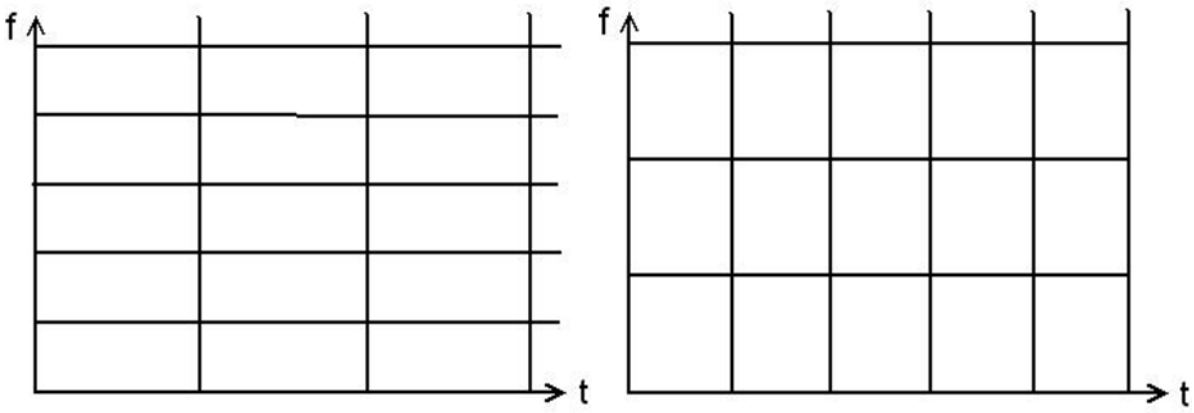


Figure II.9: The time-frequency graph of the Fourier Transform.

Figure II.10 shows the time-frequency localisation characteristics of the STFT. By the Heisenberg principle, there is a fundamental constraint on the extent of time and frequency localisation, resulting in time-frequency atoms represented as rectangles with equal surface areas. Figure II.10(a) showcases a transformation with superior frequency localisation, indicating a more precise identification of frequency components. Figure II.10(b) illustrates a transformation with improved time localisation, emphasising a more accurate representation of signal dynamics over time. This depiction highlights the inherent trade-off between time and frequency localisation in the STFT.



(a) STFT with better localisation of frequencies (b) STFT with better time localisation

Figure II.10: Time-frequency illustration of the STFT.

Two aspects distinguish the WT from the STFT at their core. Firstly, the window width is adaptable in the WT based on the analysing frequency. Secondly, the choice of the analysis function in the WT allows for greater flexibility, as illustrated in Figure II.11.

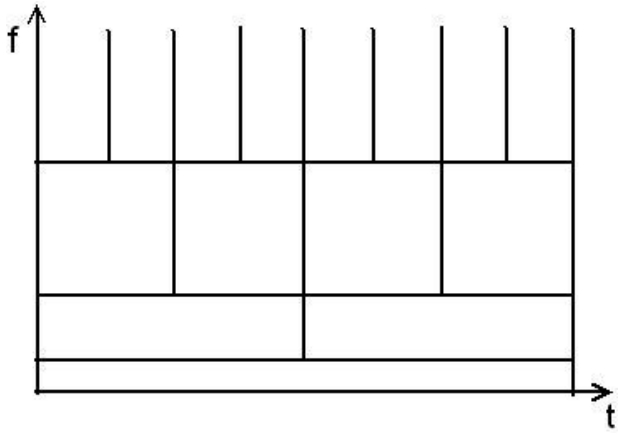


Figure II.11: Time-frequency illustration of the Wavelet Transform.

II.5 Wavelet transforms

II.5.1 Continuous WT (CoWT)

Unlike the FT, the WT allows greater flexibility in selecting the analysing function without using sine forms. A wavelet function, denoted as $\psi(t)$, represents a small oscillatory wave designed to differentiate between various frequencies [49]. A wavelet comprises the window as well as the geometry being analysed. Figure II.12 illustrates a potential wavelet called the Morlet wavelet. Multiple wavelet functions with distinct properties are developed for the Continuous Wavelet Transform (CWT) [49].

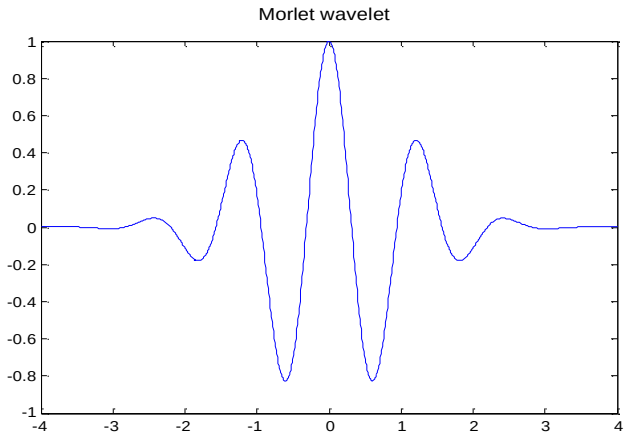


Figure II.12: Morlet wavelet

A mathematical function $\psi(t)$ is categorised as a wavelet if it satisfies the subsequent criteria [50]:

- The energy of a wavelet should be finite.

$$E = \int_{-\infty}^{\infty} |\psi(t)|^2 dt < \infty \quad (1.5)$$

The energy (E) is computed by integrating the squared magnitude analysing function ψ(t), emphasising the requirement for this quantity to remain finite.

- If $\Psi(f)$ represents the Fourier transform of the wavelet $\psi(t)$, it is imperative for the following condition to be satisfied:

$$C_\psi = \int_0^{\infty} \frac{|\psi(t)|^2}{f} df < \infty \quad (1.6)$$

This condition signifies the absence of a zero-frequency element in the wavelet (Ψ (0) = 0), indicating that the average of the WT function (t) must be zero. This criterion is called the constant of admissibility. The precise value of C_ψ is dependent on the specific wavelet chosen.

- In the case of complex wavelets, a crucial requirement is that the Fourier transformation $\Psi(f)$ must both exist and disappear in the case of negative frequencies.

The continuous WT is formulated as follows:

$$X_{WT}(\tau, s) = \frac{1}{\sqrt{|s|}} \int_{-\infty}^{\infty} x(t) \psi^* \left(\frac{t-\tau}{s}\right) dt \quad (1.7)$$

The signal after transformation, denoted as $X_{WT}(\tau, s)$, is dependent on the translation variable τ and the scale variable s. The term $\psi^*(t)$ signifies the use of the complex conjugate in the case of a complex wavelet. Normalisation of signal energy occurs at each scale by dividing the wavelet coefficients by $\frac{1}{\sqrt{|s|}}$ [50]. This normalisation guarantees that the wavelets maintain consistent energy levels across different scales.

When the scale s is modified, both the window length and the wavelet's central frequency f_c are impacted. The results of wavelet analysis are therefore expressed on a scale rather than in terms of frequency. The wavelet's temporal position is determined by the translation parameter τ; modifying τ permits the wavelet to be shifted across the signal. Rows of the time-scale plane are populated when a constant scale s is maintained while the

translation τ is varied. By contrast, the columns of the time-scale plane are filled when the scale s is varied while the translation τ remains constant. Each of the elements in $X_{WT}(\tau, s)$, which are referred to as wavelet coefficients, corresponds to a distinct frequency scale and a specific time domain point.

The inverse transformation of the WT is comparable to that of the FT and STFT. The definition of the inverse continuous wavelet transformation (ICoWT) is as follows:

$$x(t) = \frac{1}{C_\psi^2} \int_{-\infty}^{\infty} \int_{-\infty}^{\infty} X_{WT}(\tau, s) \frac{1}{s^2} \psi\left(\frac{t-\tau}{s}\right) d\tau ds \tag{1.8}$$

It is critical to specify that the admissibility constant C_ψ satisfies the second condition of the WT.

II.5.2 Discrete wavelet transforms (DWT)

Time-frequency analysis is generally feasible, but the reconstruction process poses challenges and imposes significant limitations on the basis function. This section introduces a framework that enables analysis and reconstruction in discrete time without redundancy. It becomes evident that designing and interpreting orthonormal bases in discrete time is considerably more uncomplicated compared to their continuous counterparts. Filter banks are crucial facilitating structures that can be viewed as a discrete and potentially orthonormal version of the extended STFT. We will demonstrate that an extended filter bank exhibits time-frequency precision properties comparable to the wavelet transform. Moreover, we establish a linkage between the DWT, a filter bank structured as a tree, and the CWT discussed in the preceding (section II.5.1).

The filter bank, encompassing the DWT, produces coefficients across multiple hierarchical levels during the analysis and synthesis phases. Distinct treatment methodologies are applied to these coefficients within each application domain, customising the reconstructed signal to exhibit specific desired characteristics. This section furnishes a comprehensive exploration of the broad applications of filter banks and the DWT across diverse contexts.

II.6 DWT implementation

The practical utility of the DWT stems from its capability for Multi-Resolution Analysis (MRA) [51][52], as well as its efficient Perfect Rebuilding (PR) filter bank architectures.

II.6.1 Multiresolution Analysis (MRA)

MRA is a fundamental concept in signal and image processing, particularly associated with techniques like WT. MRA aims to analyse signals or images at multiple resolution levels, capturing both coarse and fine details. In the context of WT, such as the DWT, MRA involves breaking down a signal into approximation and detail coefficients at different scales. Each resolution level corresponds to a distinct frequency band, facilitating a comprehensive understanding of the signal's frequency content across scales. This approach is valuable in applications like image compression, denoising, and feature extraction, where varying levels of detail are crucial. MRA offers a flexible framework for signal representation, enabling a nuanced analysis of complex signals or images.

Multiresolution analysis, also known as multiscale analysis, involves a series of nested subspaces, represented as $V2 \subset V1 \subset V0 \subset V{-}1 \subset V{-}2$ ..., within the space $L2(R)$, as illustrated in Figure II.13.

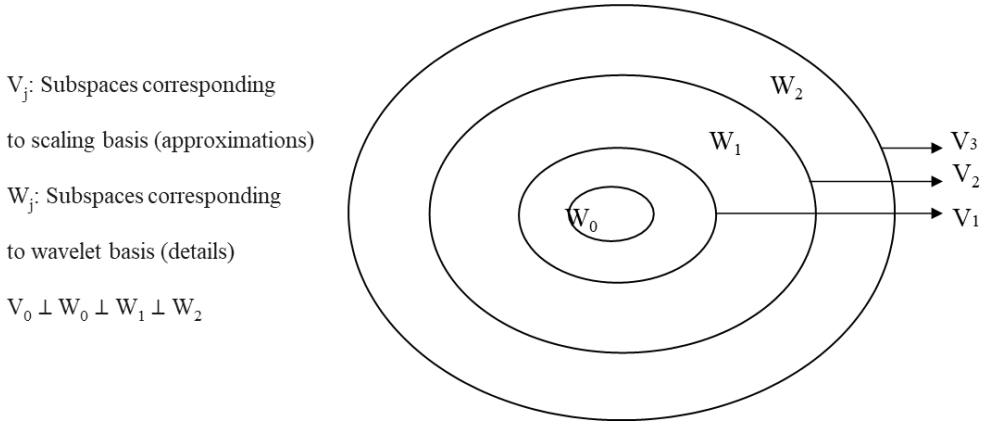


Figure II.13: scaling and wavelet basis-spanned nested vector spaces [53]

The MRA adheres to the conditions as follows:

- $V_j \subset V_{j+1}, j \in \mathbb{Z}$
- $V_{-\infty} = \{0\}\ and\ V_{\infty} = L^2$

- $f(t) \in V_j \Leftrightarrow f(2t) \in V_{j+1}$
- $V_2 = V_0 + W_0 + W_1$
- $L^2 = \cdots + W_{-2} + W_{-1} + W_0 + W_1 + \cdots = V_0 + W_1 + \cdots$
- $W_{-\infty} + \ldots + W_{-2} + W_{-1} = V_0$

By introducing the Father Wavelet scaling function φ(t), we can ensure that for every fixed j, the family. $\begin{cases} \varphi_{j,k} = 2^{-j/2}\varphi\left(2^{-j/2}t - k\right), (j,k \in \mathbb{Z}) \\ \int \varphi(t)dt = 1 \end{cases}$ (1.9)

Creates a set of vectors that are both orthogonal and normalised, serving as the basis of the subspace Vj.

If Wj denotes the mutually perpendicular constituent of Vj (Wj⊥Vj) within the subspace Vj+1, then there exists a function ψ(t) (Mother Wavelet) such that, for each given j, the family

$$\psi_{j,k} = 2^{-\frac{j}{2}}\psi\left(2^{-\frac{j}{2}}t - k\right), (j,k \in \mathbb{Z}) \quad (1.10)$$

Creates a set of vectors that are both orthogonal and normalised, serving as the basis of the subspace Wj. As a result of the nesting subspaces and the MRA requirement (3), the scaling function fulfils the subsequent 2-scale (dilation or refining) equation:

$$\varphi(t) = \sqrt{2}\sum_{n=-\infty}^{\infty} h_0[n]\varphi(2t - n),\ n \in \mathbb{Z} \quad (1.11)$$

This equation fulfils the condition for admissibility $\sum h_0[n] = \sqrt{2}$

A similar equation constrains the wavelet function.

$$\psi(t) = \sqrt{2}\sum_{n=-\infty}^{\infty} h_1[n]\varphi(2t - n),\ n \in \mathbb{Z} \quad (1.12)$$

Under the specified conditions: $\sum h_1[n] = 0$ and $h_1[n] = (-1)^n h_0[-n+1]$

The coefficients of the low-pass or high-pass filters are represented by the values $h_1[n]$ and $h_0[n]$, respectively.

II.6.2 Filter banks

The filter bank comprises filters segregating signals into frequency bands [54]. Figure II.14 illustrates an example of a two-channel filter bank. A discrete-time signal, $x(k)$, enters the analysis bank and undergoes filtering by the $L_0(z)$ and $H_0(z)$ filters, which partition the frequency content of the input signal into bands of equal width. Consequently, $L_0(z)$ and $H_0(z)$ serve as a low-pass and a high-pass filter, respectively. Each filter's output contains half the frequency content but an equal number of samples compared to the input signal. The combined outputs retain the same frequency content as the input signal, but the data volume is doubled. Hence, downsampling by a factor of two (denoted by ↓2) is applied to the outputs of the analysis bank filters. Reconstructing the original signal is achievable through the synthesis filter bank [49][54].

In the synthesis bank, the signals undergo upsampling (↑2) and pass through the filters $L_1(z)$ and $H_1(z)$, which are based on the filters in the analysis bank. The rebuilt signal y(k) is obtained by summing the outputs of the synthetic bank filters. The filter bank technique, referred to as subband coding, generates various output signals referred to as subbands [49].

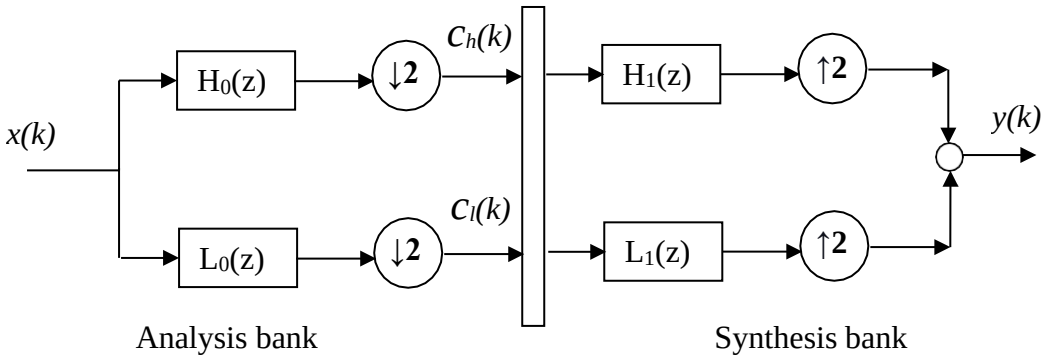


Figure II.14: Filter bank with two channels [53]

II.6.2.1 Down- and upsampling

The low-pass filter, referred to as $L_0(z)$, and the high-pass filter, referred to as $H_0(z)$, split the signal's frequency content into two equal parts. Hence, it is rational to reduce the signal's sampling rate with a factor equal to two to eliminate duplication. It is possible to

recover the signal *x(k)* by decreasing half of each sample from the filtered inputs $c_l(k)$ and $c_h(k)$ [54]. It is essential to acknowledge that the down-sampling operation (↓2) only keeps the even-numbered elements of the filter results, which means it cannot be reversed. Aliasing refers to the act of eliminating information in the frequency domain. When the Shannon sampling theorem criteria are met, there is no loss of information [54] [55]. The Shannon sampling theorem states that when downsampling a sampled signal by a factor M, the resulting spectrum may be obtained by dividing the initial spectrum into M equal bands and adding these bands together [49].

The signals undergo an initial upsampling procedure before filtration in the synthesis bank. Using a factor of two (↑2), the upsampling process is executed by inserting zeros between the initial signal samples. It is imperative to emphasise that the original signal will not be restored by downsampling and then upsampling a signal

$$x(k) = \begin{pmatrix} \vdots \\ x(0) \\ x(1) \\ x(2) \\ x(3) \\ x(4) \\ \vdots \end{pmatrix} \quad (\downarrow 2)x(k) = \begin{pmatrix} \vdots \\ x(0) \\ x(2) \\ x(4) \\ \vdots \end{pmatrix} \quad (\uparrow 2)(\downarrow 2)x(k) = \begin{pmatrix} x(0) \\ 0 \\ x(2) \\ 0 \\ x(4) \\ \vdots \end{pmatrix} \tag{1.13}$$

The transposition of (↓2) is denoted as (↑2). Since transpositions occur in reverse order, synthesis can be accomplished by transposing the analysis. Moreover, (↓2) (↑2) equals I (identity matrix), as (↑2) serves as the correct inverse of (↓2) [54]. This implies the potential to retrieve the original signal through a combination of up- and downsampling. The process involves initially inserting zeros and subsequently eliminating them, restoring the original signal.

II.6.2.2 Perfect reconstruction

For flawless reconstruction to be achieved, the bank of filters must be orthogonal. Furthermore, precise design criteria for the synthesis and analysis filters must be fulfilled.

The purpose of these criteria is to guarantee error-free signal reconstruction by averting interference and distortion [54]. The filter bank, depicted in Figure II.14, consists of two channels. The signal is divided into two frequency ranges by the low-pass and high-pass filters, $L_0(z)$ and $H_0(z)$. Downsampling would not cause information loss if they were

perfect brick-wall filters, but practical constraints prevent the realisation of ideal filters, resulting in a transition band. This transition band causes amplitude and phase distortion in each filter bank channel, in addition to aliasing [49]. To avoid aliasing in the two-channel filter bank shown in Figure II.14, the filters within the synthesis filter bank must be carefully designed [54]. In general, the input X(z) and output Y(z) of the filter banks are related as follows:

$$Y(z) = \frac{1}{2}\{H_0(z)L_0(z) + H_1(z)L_1(z)\}X(z) + \frac{1}{2}\{H_0(-z)L_0(z) + H_1(-z)L_1(z)\}X(-z) \quad (1.14)$$

Therefore, the criterion for achieving perfect rebuilding is

$$\begin{cases} H_0(z)L_0(z) + H_1(z)L_1(z) = 2z^{-N} \\ H_0(-z)L_0(z) + H_1(-z)L_1(z) = 0 \end{cases} \quad (1.15)$$

Here, N represents the total delay within the bank of the filter. An N^{th} filter order typically introduces a delay for N samples [49].

WT methods based on filters are multipurpose instruments for signal processing and data analysis. These tools provide the capability to conduct multiresolution analysis, extract essential features, and uncover latent patterns in intricate datasets [56]. Nevertheless, these benefits are accompanied by obstacles that necessitate meticulous examination. Computational complexity emerges as a notable obstacle, especially with the expansion of datasets in dimensionality or size. This has the potential to result in prolonged processing durations and heightened resource requirements, which may have an effect on applications that rely on real-time or limited resources. In addition, it is critical to select an appropriate wavelet function, as this can have a significant impact on the outcomes, specifically pertaining to the precision and significance of the features that are extracted. It is imperative for both researchers and practitioners to conscientiously assess the wavelet that best aligns with their datasets and analytical goals [57]. In the end, the utilisation of filter-based WT methods should be determined by a thorough comprehension of their benefits and drawbacks; this necessitates a scrupulous evaluation of data properties and application specifications.

II.7 Conclusion

This chapter introduces the basic concepts of biomedical signals, including EEG, PCG, and ECG, and discusses various noise sources in ECG recordings. This sets the stage for the introduction of the WT as an essential tool for improving the accuracy of signal analysis. It delves into the mathematical foundations of WT and its distinctive ability to decompose signals into their frequency components. Through case studies and examples, the practical applications of WT are showcased. Owing to its time-frequency localisation capabilities, wavelet analysis has surpassed the Fourier transform and is thus preferred for a wide array of applications, such as signal and image compression and noise reduction in signals. WT, known for its compactness and filter bank implementation, offers extensive flexibility in its deployment and in the use of various wavelet families.

Chapter III

IoT and AI in Healthcare

III.1 Introduction

IoT has emerged as an important and intrinsic component of current wireless sensor network technology. Consequently, IoT technology applications have permeated various sectors within society, such as education, industry, and healthcare systems. The automation of these applications has been enhanced through IoT, accelerating socially relevant processes globally. Today, we observe that AI is increasingly being applied as a key technology for IoT applications. From another perspective, IoT technology has improved utilities and applications in the digital world, enriching social demands related to knowledge collection and communication through various sensors, including video sensors and communication systems, which are essential elements of the IoT ecosystem. Beyond these physical devices, AI also plays a necessary and vital role in automating the systems required for processing IoT applications.

The integration of AI and IoT in healthcare, enable continuous monitoring and personalised interventions through the collection of real-time patient data by IoT devices. AI algorithms analyse this data, identifying patterns and anomalies to support informed decision-making by healthcare professionals. Optimisation algorithms fine-tune AI models for specific healthcare applications, enhancing diagnostic accuracy and treatment optimisation. Convolutional Neural Networks excel in medical image analysis, enabling early detection of abnormalities. Together, these technologies improve patient outcomes and drive innovation in clinical practices.

III.2 The Internet of Things in Healthcare

"The Internet of Things (IoT)" has gained significant traction within communication technologies. This burgeoning term, depicted as the upcoming frontier [58], has developed extensively, paving the way for transformative changes. Illustratively portrayed in Figure III.1, the IoT is poised to revolutionise numerous facets of our daily lives, heralding a paradigm shift with its potential to instigate widespread impact on a global scale.



Figure III.1: Aspects of the current city related to IoT [59]

In the coming years, there is an expected surge in IoT devices, with over 26 billion currently connecting to the Internet. Forecasts for 2030 predict a sixfold increase, resulting in six times more connected objects than people [60] (Figure III.2). This broad spectrum of interconnected items, from household lamps to automobiles, utilises physical components like sensors and microcontrollers for data exchange [61]. Each device has a unique identifier for real-time data collection, enabling seamless machine-to-machine (M2M) communication. The copious global data generated by these devices is centralised in the cloud, streamlining data management and enhancing system efficiency.

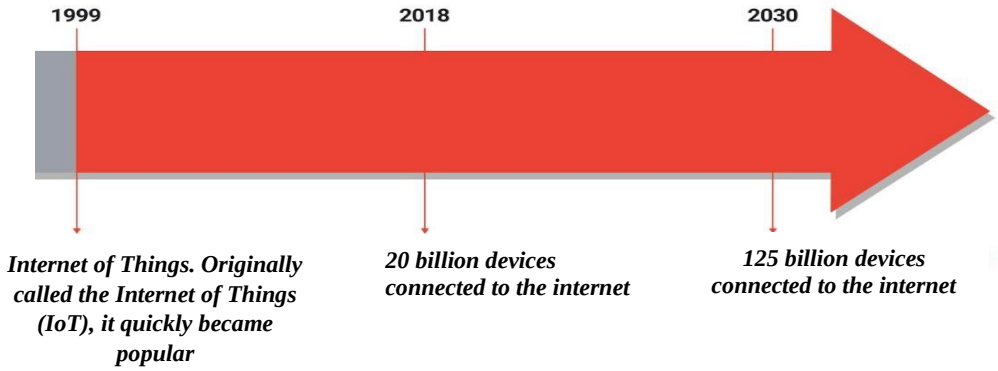


Figure III.2: Chronological history of the emergence of IoT [59]

IoT is the foundation for building Enhanced Cyber-physical Intelligent Universal Frameworks [62]. Designed for billions of physical objects (sensors and actuators), it employs various technologies like RFID, Wi-Fi, NB-IoT, and LoRa for Internet connectivity [63]. It enables seamless interaction with medical sensors, surveillance cameras, and home appliances, facilitating the development of applications and services where each object is Internet-connected [64,65]. Sensors play a crucial role in signal detection, ubiquitously in applications like mobile devices, automotive systems, climate monitoring tools, industrial control mechanisms, and healthcare equipment as shown in Figure III.3. As IoT projects transition from concept to reality, a significant challenge arises:

- Efficient data flow in the system poses questions about device-generated information, the role of devices in data creation, and information return mechanisms. Choosing between real-time transmission and batch processing complicates data management. Recognising the role of analytics in shaping the system's future is crucial. The key focus is on interpreting collected data to positively impact lives, highlighting the critical importance of the data ecosystem.

These technical considerations arise during the design phase to ensure appropriate tool usage from the outset. For smart devices and sensors, each operation generates data, transmitted via the network to the central application. At this stage, decisions on data creation standards and transmission methods are crucial. MQTT, HTTP, and CoAP are the most commonly employed protocols for data transmission, each with distinct advantages. HTTP, initially designed for the client-server model, is suitable for bidirectional data exchange between devices and central systems. However, its extensive data in headers may make it less suitable for low-bandwidth conditions.

In contrast, MQTT, developed specifically for M2M and IoT deployments, utilizes a Publish/Subscribe (Pub/Sub) model, facilitating efficient message transmission from devices to a central broker, which then relays messages to all subscribed systems [66–68]. MQTT's lightweight message size is advantageous in bandwidth-sensitive implementations. Although MQTT (Message Queuing Telemetry Transport) offers several advantages in terms of security, making it a suitable protocol for many IoT applications. It supports Transport Layer Security (TLS) and Secure Sockets Layer (SSL) protocols, ensuring data encryption during transmission to protect against eavesdropping and tampering. MQTT also allows for client authentication using username and password credentials, and supports more advanced authentication mechanisms like client certificates, ensuring that only authorized devices can connect to the broker. TLS/SSL also ensures data integrity during transmission, preventing data alteration or corruption. The lightweight nature of MQTT minimizes the attack surface, reducing potential security vulnerabilities. MQTT's flexibility in implementation over various network protocols, combined with regular updates and strong community support, helps promptly address security vulnerabilities and improve the protocol's resilience. By leveraging these features, MQTT provides a robust and secure communication framework for IoT applications, ensuring data confidentiality, integrity, and availability.

In IoT applications, devices produce data that is sent to the main application for transmission and analysis. Data transfer timing whether real-time or batched depends on device, network, and power considerations. The paramount importance lies in the accurate chronological order of data points for successful IoT applications, and any timing failure compromises the application goals. Precise alignment of data order is crucial; discrepancies may lead to inaccurate results during analysis, especially in detecting component failure conditions [69,70]. Time series data may be created as events unfold, providing a real-time record for each device. Additionally, data can be aggregated in batches, although it is not available in real time. This approach suits devices that prioritise battery life over real-time data provision [71,72].

In traditional relational databases, limitations on write requests can impact gathering all device data accurately, posing a risk of significant data loss. To address this, many IoT projects prefer NoSQL platforms like Cassandra and MongoDB. These platforms, especially Cassandra, can handle numerous write operations even with millions of consistently generating devices, preventing potential data loss [73,74]. Unlike traditional databases with a primary-replica structure, well-configured distributed database systems, like those used in NoSQL platforms, eliminate the concept of a "primary" server. Each node in the cluster can independently process transactions, ensuring consistent maintenance of the complete record over time.

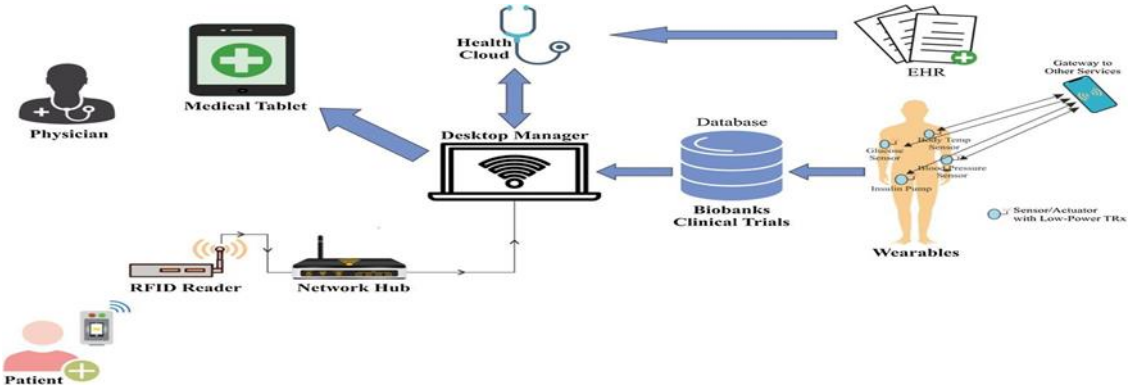


Figure III.3: IoT in healthcare frameworks [75]

In the healthcare application, the IoT devices transform medical data into actionable insights for improved patient care, marking a technological shift in healthcare with a focus on interconnected objects [76]. Connected sensors and wearables store relevant information in the cloud, enabling real-time patient monitoring. IoT has the potential to significantly

impact life-saving applications involving data collection from bedside devices, patient information visualisation, and real-time diagnostics. To address global challenges in healthcare device operations, securely storing data in the cloud allows efficient oversight by carers or doctors, saving valuable time. Remote diagnosis and asset tracking eliminate manual visits, and accurate hospital service localisation is achieved through sensors and wireless technologies, ensuring precise information retrieval [77,78].

III.3 The data in the field of health

Data is integral to patients' diagnosis, treatment, and management, guiding clinicians in assessing health. The digitisation of healthcare has exponentially increased data volume, necessitating compatible equipment for processing. The expanded availability of data enhances medical decision-making across specialties. Figure III.3 visualises evolving healthcare data sources, reflecting their diversity. The dynamic nature of data sources, driven by complex datasets and new capabilities, underscores the evolving landscape of healthcare data.

III.3.1 Clinical data

Technological advancements in healthcare digitisation yield significant clinical data, extending beyond healthcare providers to include exogenous data from sources like home monitoring systems, smartphones, and wearable devices [79]. This accessibility allows a comprehensive understanding of patients' health, emphasising a multifactorial approach rather than symptom-based disease determination [80] . The challenge lies in harnessing the full potential of exogenous data for diagnosis and treatment. Integrating this approach into research using data-driven AI systems is recommended for enhanced predictive and personalised patient care. The intricate and unstructured nature of healthcare data poses a challenge for conventional tools and methodologies [81].

With a shift towards unstructured formats, growing data diversity in healthcare faces challenges like inconsistent formatting and varying data quality [82]. Clinical data primarily resides in Electronic Health Records (EHRs), providing comprehensive patient information [83,84]. EHR data is categorised into structured and unstructured types, each posing challenges. Structured data, adhering to standardised coding, still exhibits format variations, complicating combined analysis. Unstructured data from diverse sources adds complexity to

EHR integration. Navigating through multiple systems for analysis is required, as highlighted in the accompanying table III.1 [85–87] .

Table III.1: Data categories and different data elements [59]

data category	data element	Description
structured	demographic information	Gender, age, height, weight, blood type, etc.
	medications	Ordering medications, prescriptions, allergies, etc.
	life habits	Habits regarding smoking, alcohol, drugs and genetic history.
	Physiological data and results	Blood pressure, ECG, oxygen saturation and other monitoring data.
	History of hospitalisations and diagnoses	Historical data on previous treatments and medical history in health facilities.
unstructured	Medical imaging	Radiography, medical resonance imaging (MRI), computer tomography (CT), etc.
	Clinician Notes	Documentation from dialogues and patient reviews.
	pathology report	Data from tissue and cell examination.

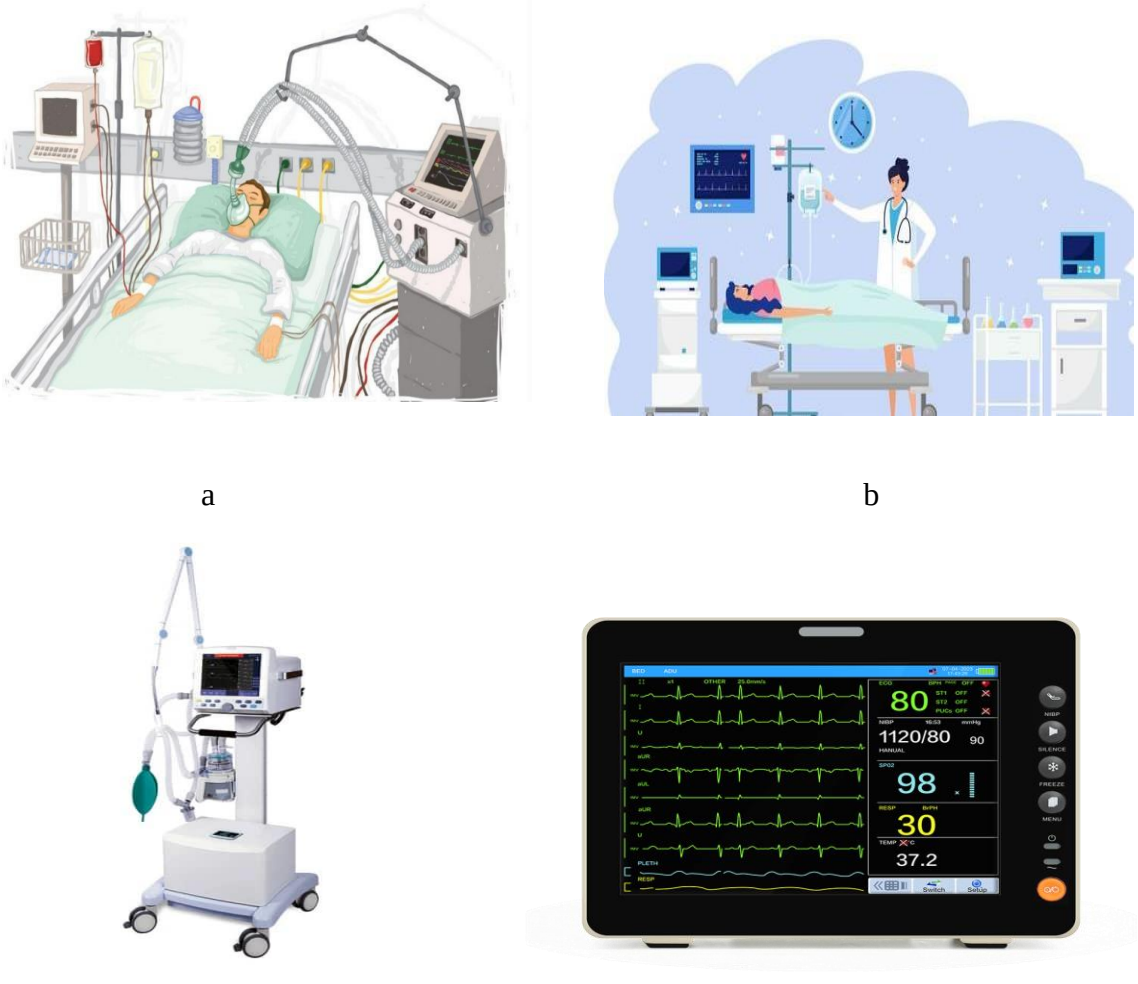
III.3.2 Patient monitoring

Remote Patient Monitoring (RPM), a system for overseeing patients remotely, empowers individuals to manage their health actively. When used by healthcare professionals, RPM offers continuous insights into a patient's health trajectory and enhances understanding of treatment plan compliance, enabling timely interventions [88,89]. It strengthens clinician-patient relationships by leveraging transmitted data to craft personalised care strategies and make informed decisions collaboratively. The American Heart Association supports initiatives improving RPM accessibility, emphasising appropriate design and evidence-based utilisation [90]. Patient monitoring is integral to treating hospitalised patients within the broader healthcare value chain.

Patient monitoring provides continuous physiological data, offering insights into vital signs [91]. Tracking these signs allows clinicians to assess their health status, enabling early detection of potential complications and timely interventions. Monitoring technologies, tailored to specific signals, share consistent components: sensors detecting physiological signals, transduction to electrical counterparts, amplification, filtration, and visual presentation to clinicians. The data undergoes comprehensive analytics before

integration into the EHR [92,93]. Monitoring systems include adjustable thresholds, akin to alarm systems, with accumulated data seamlessly integrated into the EHR.

Monitoring individual patients with diverse health states and treatments often requires additional devices to capture various physiological indicators such as intravascular pressures, cardiac outputs, or specialised neurological monitoring tailored to specific needs or clinical contexts. Monitoring evolves based on factors like surgery, inter-hospital transfer, or anaesthesia recovery. Regardless of the variables, fundamental practices include tracking vital signs like pulse, blood pressure, respiratory rate, oxygen saturation, and capnography. Acknowledging this broader landscape while exploring ECG signals in detail ensures a holistic understanding of patient well-being for delivering targeted and personalised care [94,95].



a b

c d

Figure III.4: Compliance tracking and related equipment. a. Supervision in intensive care units. b. Monitoring of normal patients. c and d: Patient monitoring devices

In line with many procedures in the medical field, as illustrated in Figure III.4, patient monitoring, in general, is accompanied by numerous guidelines and standards to ensure a minimum level of service quality. Focusing on patients with cardiovascular diseases, we will narrow the guidelines to using RPM technologies to enhance cardiovascular disease outcomes. Let us begin with ease of use and accessibility. The effectiveness of RPM heavily relies on its design and user-friendliness. RPM often involves interaction among various user groups through a digital system or with the general practitioner in their office. Communication in these usage scenarios is typically multimodal, making it crucial to understand who, how, and when information transmission and personal communication occur.

Developing a device using a user-centred design involves end-users at all stages, ensuring an understanding of user needs and usage context for system integration into clinical workflows. For RPM, user-centred design is crucial for high adoption rates and minimising user errors [96]. This approach caters to diverse individuals, enhancing patient satisfaction. Ensuring user-friendliness requires a detailed analysis of end-user needs. Interoperability, integration, and data confidentiality are vital concepts. Achieving the highest interoperability level benefits healthcare systems [88,89], while RPM integration into workflows should be manageable for them. Preserving patient data confidentiality and addressing liability and reimbursement issues are challenges, emphasising the importance of trust and confidentiality in healthcare communication. Balancing accessibility and confidentiality impact stakeholders, including patients, trust in healthcare providers, and the healthcare system [97–99].

III.4. AI in Healthcare

III.4.1 The Metaheuristic Optimisation Algorithms

Optimisation seeks the most favourable solution to a given problem from all possibilities [100]. Traditional methods often need revision for today's intricate problems, categorised as difficult optimisation problems. Exact methods may not provide optimal solutions within a reasonable timeframe. These problems involve continuity, discreteness, constraints, objectives, and dynamics. In pursuing optimality, predefined goals and constraints guide the process [101]. The objective function varies across different problem types [102]. Optimisation within a constraint system aims to identify parameter values that

optimise the specified objective. Classical or local heuristic search methods are used for feasible or quasi-optimal solutions. Researchers introduce metaheuristic algorithms as novel techniques, proving valuable for complex optimisation challenges within reasonable timeframes and computational costs. Metaheuristics gain popularity for their advantages over traditional methods: being independent of gradient information, simple implementation across diverse fields, and mitigating the risk of being trapped in local optima through exploration capabilities.

III.4.2 Optimisation Problem

An optimisation problem is exploring a solution space to find an optimal solution quantified by an objective function. This quantification leads to the goal of maximising or minimising the problem. A set of exact methods allows finding a solution in a finite and generally polynomial time. These methods, including the gradient method, the Newton method, etc., are deterministic, meaning they provide the best-expected result in a finite number of steps through derivation or traversing all or part of the solutions. Difficult optimisation represents a class of optimisation problems that cannot be solved in polynomial time or by an exact method, given the constraints of the characteristics of the objective function.

III.4.2.1 Formulation of the optimisation problem

From a mathematical perspective, it is feasible to represent most optimisation problems in a generic form, aiming to minimise the following function:

$$f_i(x), (i = 1,2,3 \dots, M), x \in R^D \tag{3.1}$$

with:

$$h_j(x) = 0, (j = 1,2,3 \dots, J) \tag{3.2}$$

$$g_k(x) \leq 0, (k = 1,2,3 \dots, K) \tag{3.3}$$

Where $f_i(x)$, $h_j(x)$, and $g_k(x)$ are functions of the design vector. They represent the components of the D-dimensional vector, where x is the real, continuous, or discrete design or decision variable. The function $f_i(x)$, where (i = 1,2, 3..., M), is referred to as the objective function or simply the cost function. In the case of M = 1, there is only one objective. The space covered by the decision variables is termed the design space or search space R^D, while

the space formed by the values of the objective function is known as the solution space or response space. Equalities for $h_j(x)$ and inequalities for $g_k(x)$ are referred to as constraint functions. We can also express the inequalities in the other direction (≥ 0), and objectives can be formulated as a maximisation problem. In a rare but extreme case where there are no objectives at all, only constraints exist. Such a problem is called a feasibility problem, as any feasible solution is optimal.

III.4.2.2 Classification of optimisation problems

The classification of optimisation problems can also be carried out by examining the nature of the objective landscape, which can be divided into multi-modal and uni-modal problems (including convex optimisation). Additionally, the classification may pertain to the determinism of the problem. If the formulation has no randomness, the problem is deemed deterministic, and all the problems mentioned earlier are essentially deterministic. However, if there is uncertainty in variables or function forms, such optimisation involves probability distributions and expectations. In such cases, they are often called stochastic optimisation or robust optimisation. The classification of optimisation problems and the terminologies used in optimisation literature can be diverse and potentially confusing. Whether an optimisation problem is considered easy or difficult can depend on various factors and the actual mathematical formulation or functions of the problem. Three factors that make a problem more challenging are the objective function's non-linearity, the problem's high dimensionality, and the search domain's complex shape.

Non-linearity and multi-modality:

The high non-linearity of a function to be optimised generally implies multi-modality with multiple local modes featuring multiple (possibly infinite) optima. In most cases, algorithms designed to solve such problems are more likely to get trapped in local modes.

High dimensionality:

High dimensionality is associated with the curse of dimensionality, where distances become large. In contrast, the volume that any searching algorithm can effectively explore becomes insignificant compared to the vast feasible space.

Constraints:

The presence of multiple constraints can introduce complexity to the feasible region, characterised by irregular geometries or shapes. In certain scenarios, the feasible region may be fragmented into disconnected portions with isolated islands, posing a challenge for algorithms to explore all feasible areas and potentially overlooking true optimality thoroughly. Additional considerations, such as the time required to evaluate an objective, play a crucial role. In various fields like bioinformatics, aerospace engineering, and deep learning, assessing a single objective can be time-intensive (ranging from hours to days or weeks), resulting in high computational costs. Hence, the selection of efficient algorithms becomes of utmost importance.

III.4.2.3 Inspiration of Metaheuristics

The fundamental concept behind most metaheuristic algorithms draws inspiration from nature, animal behaviour, or physical phenomena [100]. Metaheuristic algorithms are generally classified into three main categories: evolution-based techniques, physics-based techniques, and swarm-based techniques. Evolutionary methods mimic the process of evolution in nature to perform optimisation [103]. On the other hand, physics-based algorithms optimise using the principles of physics in the universe. The third class of metaheuristic algorithms consists of swarm-based techniques, which emulate the behaviour of animals in a group.

Metaheuristic optimisation methods inspired by nature have led to the discovery of numerous optimisation algorithms in various categories, these include:

Genetic Algorithm (GA): This algorithm is inspired by the processes of natural selection and evolution. It involves the evolution of a population of potential solutions to find the optimal solution.

Harmony Search Algorithm (HSA): Modelled after the improvisation process of musicians searching for the best harmony, this algorithm seeks optimal solutions by adjusting variables in a harmonious manner.

Particle Swarm Optimisation (PSO): Inspired by the collective behaviour of birds or particles in a swarm, PSO involves particles moving through the search space to find the optimal solution.

Flower Pollination Algorithm (FPA): This algorithm simulates the pollination process of flowers and the interaction between flowers to optimise a given objective function.

Each of these algorithms leverages principles from nature to address optimisation problems in distinct ways, offering a diverse set of tools for solving complex problems in various domains.

III.4.3 Optimisation algorithms for WT in biomedical signals

III.4.3.1 ECG noise elimination using WT

WT is an effective and widely employed method for signal representation in both the time and frequency domains. The method has been successfully implemented in a multitude of contexts, such as signal compression and function selection [104–106]. In general, WT can be classified as either continuous WT (CWT) or discrete WT (DWT) [107]. In recent times, WT has been extensively utilised in the processing of non-stationary signals, including EEG and ECG, due to the demonstrated detrimental impacts of numerous ECG artefact effects on the actual ECG signal. Muscular action and PLI [108]. are the origins of these artefacts. This research establishes a wavelet denoising method based on the elimination of WGN and PLI. Figure III.5 illustrates the wavelet denoising process with three decomposition levels ($\boldsymbol{L = 3}$).

The approach developed by Donoho is one of the methods for DWT described in [109] As depicted in Figure III.6, multiple coefficients are utilised to modify the input signal's high and low frequencies in order to degrade an input signal that is already noisy is also defined as follows [110]:

$$C(a,b) = \sum_{n\in Z} x(n)\, g_{j,k}(n) \tag{3.4}$$

In Equation (3.4), $\boldsymbol{C(a,b)}$ represents the dynamic wavelet coefficients, $\boldsymbol{a = 2^{-j}}$, $\boldsymbol{b = k2^{-j}}$, $\boldsymbol{j \in Z}$, $\boldsymbol{k \in Z}$, $\boldsymbol{Z}$ stands for set of integers, $\boldsymbol{a}$ represents the size of the time scale, $\boldsymbol{b}$ represents the translation, $\boldsymbol{x(n)}$ denotes the input ECG signal, and $\boldsymbol{g_{j,k}(n)} = \boldsymbol{2^{j/2} g(2^j n - k)}$ is the DWT .

Generally, the wavelet denoising process involves three steps, as outlined below:

• **ECG signal decomposition:** This step entails dividing the original ECG signal into three

levels and breaking down each level into two components – the approximation coefficients (cA) and the detail coefficients (cD), as described by Equations (3.5) and (3.6) respectively. The detail coefficients (cD) undergo processing with a high-pass filter, while the approximation coefficients (cA) are further decomposed for the subsequent level according to the following procedure:

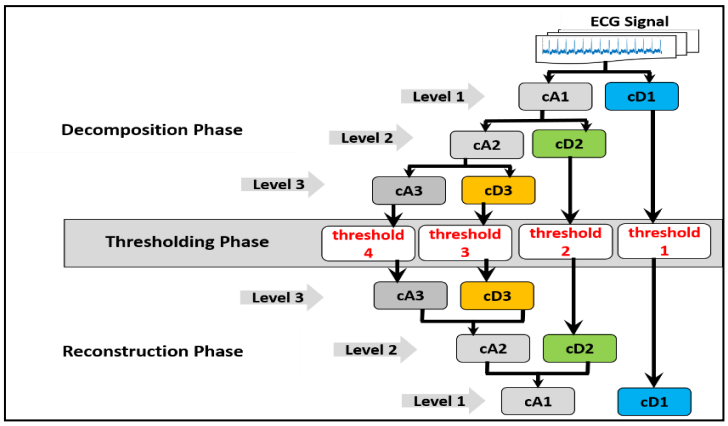


Figure III.5: ECG denoising process [111].

$$cA_i(t) = \sum_{k=-\infty}^{\infty} cA_{i-1}(K)\phi_i(t-K) \tag{3.5}$$

$$cD_i(t) = \sum_{k=-\infty}^{\infty} cD_{i-1}(K)\Psi_i(t-K) \tag{3.6}$$

Where $cA_i(t)$, $cD_i(t)$: the approximation coefficients and the detail coefficients for level i, respectively. Ψ denotes scaling, and ϕ signifies shifting.

• **Thresholding:** DWT employs the Minimax thresholding technique to determine the threshold values at which the maximal mean square error (MSE) between the original and denoised signal is minimised. The calculation of these threshold values aims to reduce the worst-case error encompassing all wavelet coefficients. DWT thresholds are computed as follows using the Minimax criterion:

Noise Level Estimation: It is necessary to calculate the noise level that is present in the signal. Utilising statistical estimators, such as the median absolute deviation (MAD) of the coefficients, or calculating the standard deviation of the wavelet coefficients in the noisy signal, are two approaches to obtaining this estimate. For Minimax thresholding to be effective, noise estimation precision is critical.

Determine the threshold values: Determine the threshold value for each wavelet coefficient at a particular scale and level by applying the Minimax criterion, as illustrated in Equation (3.7). The determination of the threshold (δ) for each coefficient is as follows [109]:

$$\delta = \begin{cases} \sigma(0.3936 + 0.1829log_2(N)), & N > 32 \\ 0, & N \leq 32 \end{cases} \quad (3.7)$$

Where $\sigma = \frac{median(|D_{ij}|)}{0.6745}$, D_{ij} are unit-scale detail coefficients, and N is the length of the signal vector.

• **Reconstruction:** involves the utilisation of the (inverse DWT) iDWT, as described in [112], to reconstruct the ECG denoised signal (Equation 3.8).

$$\boldsymbol{ECG_{denoised}} = \sum_{k=-\infty}^{\infty} \boldsymbol{cA_L(K)}\ \phi'_i(\boldsymbol{t-k}) + \sum_{i=1}^{L}\sum_{k=-\infty}^{\infty} \boldsymbol{cD_{i+1}(K)}\Psi'_i(\boldsymbol{t-k}) \quad (3.8)$$

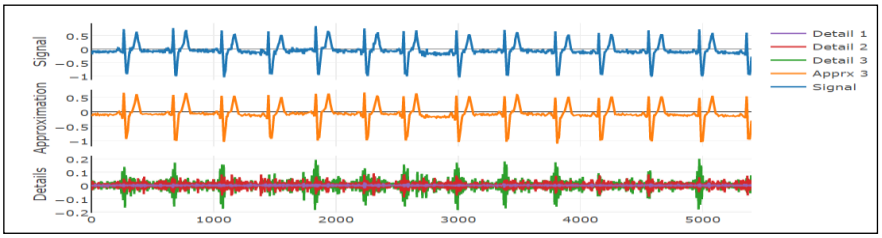


Figure III.6: Details and approximations coefficients [111].

Where 'ECG denoised' represents the reconstructed ECG signal and ***i*** denotes the decomposition level. Wavelet denoising involves five parameters with discrete ranges (refer to Table III.2). The efficacy of noise reduction depends on the chosen wavelet parameters.

The three phases of the wavelet denoising procedure are depicted in Figure III.5. In the initial stage, DWT is utilised to decompose the ECG signal.

Table III.2: Wavelet denoising parameter ranges [57]

Wavelet denoising parameters	Range
Type of wavelet basis function ***Φ***	Coiflet (coif1-coif5), Symlet (sym1-sym45), Daubechies (db1-db45), Fejer-Korovkin (fk4- fk8- fk14- fk18&fk22), and Biorthogonal (bior1.1-bior1.5 & bior2.2-bior2.8 & bior3.1-bior3.9),
Threshold function ***β***	Soft (s), Hard (h)
Level of decomposition ***L***	1–10
Threshold selection of a rule ***λ***	Sqtwolog, Minimax, Heursure, and Rigsure
Rescaling approach ***ρ***	No scaling (one), one level (sln), Several levels (mln).

In this phase, the optimal mother wavelet function (Φ) is chosen to be utilised in the decomposition procedure of the ECG signal. In most cases, the decomposition level (L) is established using combined ECG and prior experience data. The objective of this thesis is to optimise WT parameters. As a second step, thresholding is implemented. The wavelet is characterised by two common thresholds, which are hard (h) and soft (s) thresholds [107,113,114]. The contrast between hard and soft thresholding is depicted in Figure III.7.

For each type of threshold – soft (s) and hard (h) – selection rules (λ), and rescaling methods (ρ), specific choices must be made. The selection of these thresholding methods is crucial as it impacts the overall efficacy of noise removal. Generally, the threshold value is determined based on the intensity of the noise (δ). Tables III.3 and Table III.4 present the different thresholding selection rules and rescaling parameter values.

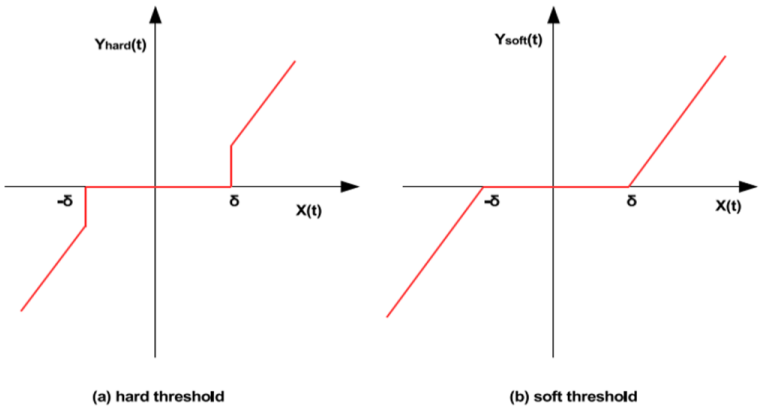


Figure III.7: Hard and soft thresholding techniques [111].

Lastly, Equation (3.9) is applied to the threshold rules.

$$ECG_{noisy}(n) = s(n) + \delta e(n) \quad (3.9)$$

Here, $s(n)$ denotes the original ECG signal,$e(n)$ stands for the noise, δ represents the noise amplitude, and n signifies the sample number. Each wavelet coefficient level *(cA and cD)*, requires independent utilisation of parameters (β, λ, ρ) to apply the wavelet. Finally, the iDWT is utilised as the concluding step to reconstruct the ECG signal.

Table III.3: Threshold selection rules [111]

Threshold selection rule	Description
Rule 1: Rigrsure	The selection of the threshold is based on Stein's Unbiased Risk Estimate (SURE).
Rule 2: Sqtwolog	The threshold is chosen equal to $\sqrt{(2logM}$ where M is number of coefficients in series
Rule 3: Heursure	The threshold is chosen using a combination of the first two rules
Rule 4: Minimaxi	The threshold is chosen to be equal to the Max (MSE)

Table III.4: Rescaling methods for wavelet thresholding [112]

Wavelet thresholding rescaling methods $\boldsymbol{\rho}$	rescaling
sln	Single level
mln	Multiple levels
one	No scaling

III.4.3.2 Genetic Algorithm (GA)

The challenge of global optimisation was tackled using the Genetic Algorithm (GA) technique, which integrates principles of natural selection and genetics. Initially, a random set of potential solutions is generated, and their effectiveness is assessed using a fitness function [112]. This function evaluates the performance of the GA within a specific context and gauges the quality of each solution. The objective of denoising is to effectively remove interference and restore the original ECG signal. A common optimisation goal in ECG noise reduction is to maximise the signal-to-noise ratio (SNR) between the original ECG signal and the denoised ECG signal. Consequently, the SNR is chosen as the fitness function. To compute the SNR, consider an original signal $x(n)$ with N samples and a reconstructed approximation of this signal denoted as $\hat{x}(n)$

$$SNR = 10log_{10}\frac{\sum_{n=1}^{N}[x(n)]^2}{\sum_{n=1}^{N}[x(n) - \hat{x}(n))]^2} \tag{3.10}$$

We chose the SNR as the fitness function for the GA to enhance the optimisation process. SNR provides a quantitative measure of ECG signal quality relative to noise, offering a straightforward metric for evaluating signal quality. By maximising SNR, the GA aims to identify an optimal combination of parameters and filters to reduce noise from Baseline Wander, Muscular Movement Artifacts, PLI, and AWGN. This aligns with our objective of improving the accuracy and reliability of ECG signal interpretation for precise diagnosis of cardiac conditions. This approach emphasises maximising signal quality while minimising the impact of noise, including PLI and AWGN, to enhance the usefulness of ECG data in clinical settings.

Globally optimised network parameters are generated by GAs through the utilisation of three fundamental operators: mutation, selection, and crossover. GA makes use of the population of prospective solutions. By repeatedly performing computations on the operators (selection, crossover, mutation), the GA ascertains the optimal solution in accordance with the principles of natural selection and survival of the fittest. The control

variables for the GA consist of population size, the likelihood of crossover, and the probability of mutation. GA successively generates chromosomes that represent alternative solutions to the problem or a solution that yields positive results as determined by the fitness function. A thorough examination of the fundamentals of conventional GAs is provided. The subsequent section will provide a description of the stages comprising the executed GA. [115,116]:

The generation of new populations involves three discrete procedures. An initial pair of novice players engage in the use of the roulette wheel. Subsequently, crossover operations are executed on the newly generated individuals (Figure III.8). In the third phase, mutation processes are implemented by multiplying each coefficient by a random number ranging from [0.8 to 1.2].

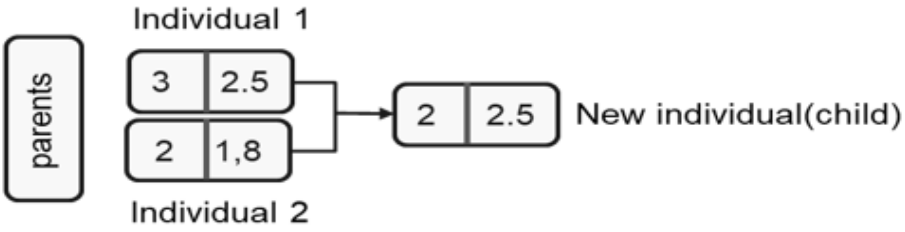


Figure III.8: Operation crossover [37]

The GA employs a population size of 50 individuals and runs for a maximum of 100 iterations. A mutation rate of 0.02 and a crossover rate of 1 are specified.

Algorithm 1 Genetic Algorithm Code

```
1: Xchrom← Generate_Initital_Population
2: Evaluate (Xchrom)
3: while (Stopping criterion is not met) do
4: Xchrom'← Selection (Xchrom)
5: Xchrom''← Crossover (Xchrom')
6: Xchrom'''← Mutation (Xchrom'')
7: Evaluate (Xchrom''')
8: Xchrom← Replacement (Xchrom''' ∪ Xchrom)
9: end while
```

III.4.3.3 Particle Swarm Optimisation (PSO)

The use of PSO in optimisation was extensively discussed in [117]. PSO begins with multiple potential solutions, collectively known as a swarm. Each solution is

represented as a particle, and each particle iteratively explores the search space. In each iteration, a particle evaluates both its locally optimal solution based on the fitness function (local best) and the globally optimal solution among its neighbours (global best). By considering these factors, particles adjust their positions to converge towards optimal solutions, akin to the social behaviour of birds in flocks [118]. Algorithm 2 presents the PSO code. According to this theory, each particle is characterised by its current location: (a) $\boldsymbol{x_i}$ is the current location of particle $\boldsymbol{i}$, (b) $\boldsymbol{v_i}$ current velocity, (c) $\boldsymbol{y_i}$ best local value, and (d) $\hat{\boldsymbol{y}}_{\boldsymbol{i}}$ best global value. Throughout the optimisation loop (see Algorithm 2, lines 6-16), these attributes of each particle are continuously updated at each time step (t).

$$\boldsymbol{y_i(t+1)} = \begin{cases} \boldsymbol{y_i(t)} & \boldsymbol{if\ f\big(x_i(t+1)\big) \geq f\big(y_i(t)\big)} \\ \boldsymbol{x_i(t+1)} & \boldsymbol{if\ f\big(x_i(t+1)\big) < f\big(y_i(t)\big)} \end{cases} \tag{3.11}$$

$$\hat{\boldsymbol{y}} = \{\boldsymbol{y_i(t)} | \boldsymbol{i = arg_{i=1\ldots,N}\ min\ f\big(y_i(t)\big)}\} \tag{3.12}$$

Consider N to be the number of elements comprising the swarm. In Equation (3.13), the velocity vector from particle i to dimension $j \in [1, Nd]$, is associated with the updated dimension velocity in $v_{i,j}$ .Furthermore, the subsequent components are integrated:$\omega v_{i,j}(t)$ In this context, ω denotes the impact of the antecedent velocity, while $v_{i,j}$ represents the earlier velocity. Anxiety associated with exploration increases as the value of ω rises. On the other hand, as ω decreases, the emphasis transitions to exploitation.

$\boldsymbol{y_{i,j}(t) - x_{i,j}(t)}$: signifies that particle $\boldsymbol{i}$ is moving in the direction of the local best.

$\hat{\boldsymbol{y}}_{\boldsymbol{j}}\boldsymbol{(t) - x_{i,j}(t)}$: signifies that particle $\boldsymbol{i}$ moving in the direction of the global best.

$$\boldsymbol{v_i(t+1) = \omega v_{i,j}(t) + c_1 r_{1,j}(t)\left(y_{i,j}(t) - x_{i,j}(t)\right) + c_2 r_{2,j}(t)\ (\hat{y}_j(t) - x_{i,j}(t))} \tag{3.13}$$

An acceleration constant denoted as c_1 and c_2, while r_1 and r_2 produce a uniformly distributed random number between 0 and 1. The term "intra-weight," denoted as " ω " governs the historical velocity. The position of particle i is updated by Equation (3.12).

$$x_i(t+1) = x_i\ (t) + v_i(t\ +\ 1) \tag{3.14}$$

Algorithm 2. Particle Swarm Optimisation code

1: for i = 1, …, N do
2: x_i = Generate_Initital Position for Particle (i)
3: v_i = 0
4: v_i = x_i
5: end for
6: repeat
7: for i = 1, …, N do
8: f (i) = Evaluate Particle (i)
9: y_i = Update Using Equation (3.11)
10: $\hat{y}$i = Update Using Equation (3.12)
11: for j = 1, …, Nd do
12: v_i = Update Velocity Using Equation (3.13)
13: end for
14: x_i = Update Using Equation (3.14)
15: end for
16: until (Stopping Criteria is met)

III.4.4 Disciplines and components of AI

The healthcare sector is experiencing a substantial data surge, with health data growing from 153 exabytes in 2013 to 2314 exabytes in 2020 [119]. Effectively managing and processing this vast amount of data is challenging. The continuous expansion of healthcare data from diverse sources and technologies [120] exceeds the capacity for analysis and utilisation. Leveraging AI is a solution to address this. AI enables machines to replicate human intelligence, accurately interpret external data, learn from it, and apply those learnings to achieve specific goals [121]. Figure III.9 concisely overviews AI subsets, highlighting the primary categories machine learning and deep learning and their relationships.

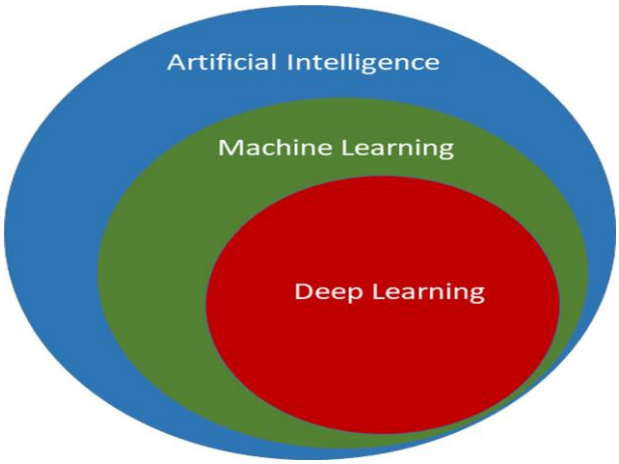


Figure III.9: Full representation of AI subsets [59]

Machine learning (ML) involves algorithms connecting input and output data to implement statistical models. These algorithms process numerous variables to forecast

results, enabling the analysis of previously challenging data volumes. ML is categorised into five segments: supervised learning, unsupervised learning, reinforcement learning, and, to a lesser extent, self-supervised learning and semi-supervised learning [122,123].

Deep learning (DL), a subset of machine learning (ML), operates with fewer assumptions about the underlying data. This flexibility enables effective handling of intricate datasets and performing complex tasks like speech recognition, image interpretation, and natural language understanding. Deep learning employs multiple neural networks with numerous layers, extracting hierarchical features for intricate representations and pattern learning [123,124]. Figure III.10 visually represents various ML subsets, including supervised, unsupervised, reinforcement, self-supervised, and semi-supervised learning, providing a comprehensive overview of the machine learning landscape.

Neural networks process raw data, focusing on clustering and identifying patterns. Unlike traditional algorithms, deep learning continuously improves by learning optimised feature detectors for pattern detection and classification, excelling in analysing intricate datasets [124]. Feature layers are crafted through data-driven training. Practical application requires substantial, high-quality data for fully operational multilayer networks. Deep learning models demand non-temporal data and relatively low complexity in the application domain [125,126]. Both machine learning and deep learning algorithms start with data processing, feature extraction, and addressing the specific task.

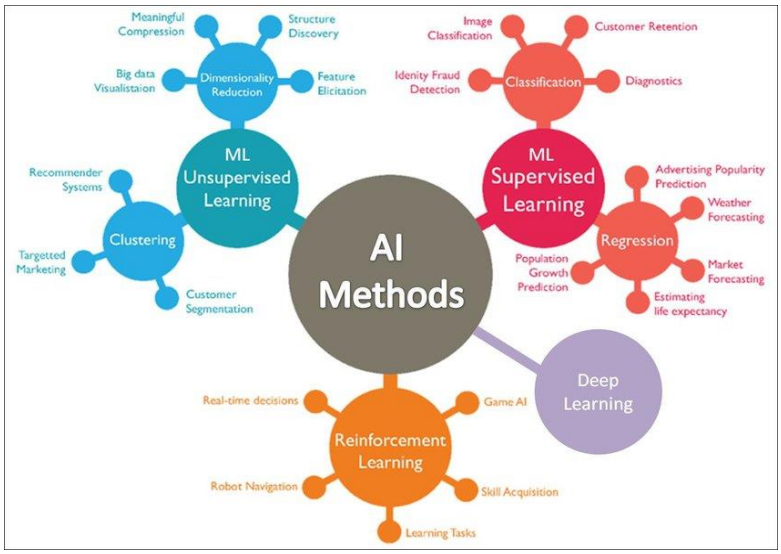


Figure III.10: Types of machine learning algorithms [127]

AI exploration involves delving into neural networks, specifically Artificial Neural Networks (ANNs), inspired by the human brain. ANNs focus on neurons, where the

fundamental principle involves weighting input (x) with a parameter (w) and a bias (b). The cumulative sum of these elements, expressed as z = $w_i * x$ + b, serves as input for an activation function (ϕ), producing the neural model and, ultimately, yielding the output of the neural model, as depicted in equation (3.15):

$$y = \phi(z) = \phi(w_i * x + b) \tag{3.15}$$

Considering only the argument of ϕ, we obtain a linear discriminant function [128,129].

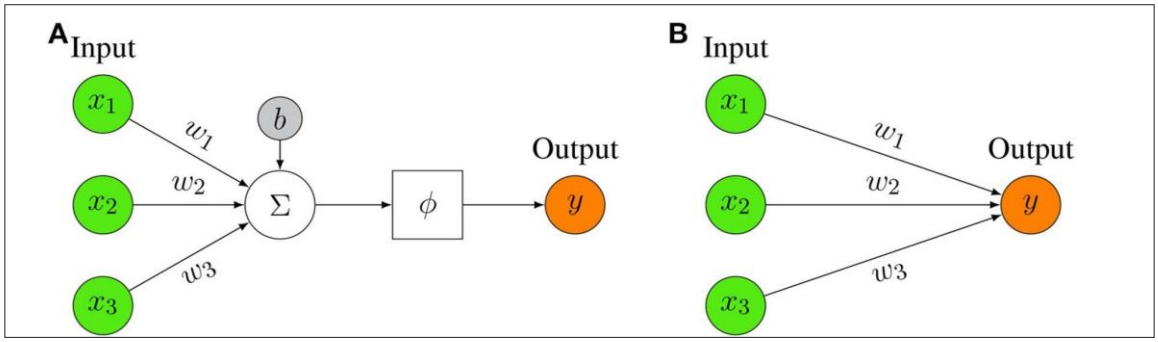


Figure III.11: Representation of a mathematical model of artificial neurons.
(A) The neuron's input is summed up and filtered through the activation function ϕ (for example, refer to Table III.5).
(B) Simplified depiction of an artificial neuron model. Only the essential elements are illustrated [130].

Table III.5: Summary of commonly employed activation functions in neuron models [131]

Activation function	φ(x)	φ′(x)	Values
Hyperbolic tangent	$\tanh(x) = \frac{e^x - e^{-x}}{e^x + e^{-x}}$	$1 - \phi(x)^2$	$(-1,1)$
Sigmoid	$S(x) = \frac{1}{1 + e^{-x}}$	$\phi(x)(1 - \phi(x))$	$(0,1)$
Rectified linear unit (ReLu)	$R(x) = \begin{cases} 0 & \text{for } x < 0 \\ x & \text{for } x \geq 0 \end{cases}$	$\begin{cases} 0 & \text{for } x < 0 \\ 1 & \text{for } x \geq 0 \end{cases}$	$[0, \infty)$
Heaviside function	$H(x) = \begin{cases} 0 & \text{for } x < 0 \\ 1 & \text{for } x \geq 0 \end{cases}$	$\delta(x)$	$[0,1]$
Signum function	$\text{sgn}(x) = \begin{cases} -1 & \text{for } x < 0 \\ 0 & \text{for } x = 0 \\ 1 & \text{for } x > 0 \end{cases}$	$2\delta(x)$	$[-1,1]$
Softmax function	$y_i = \frac{e^{x_j}}{\sum_j^n e^{x_j}}$	$\frac{\partial y_i}{\partial j} = y_i(\delta_j - y_j)$	$(0,1)$

As mentioned earlier, activation functions are a fundamental and crucial concept in machine learning. Before delving into the significant mathematical context of the tasks that we will use in our contributions, it is essential to highlight some important characteristics of these functions, namely [122]:

a. The challenge of vanishing gradients: During gradient descent, adjustments aim to minimise loss, posing a challenge.

b. Zero-centred: The activation function's output must exhibit symmetry around zero, ensuring that gradients do not favour any direction.

c. Computational expenses: Activation functions are employed after every layer and must be computed numerous times within deep networks. Consequently, they need to be computationally economical.

III.4.4.1 Convolutional Neural Networks

Convolutional neural networks (CNNs) are a specialised subset of deep neural networks that utilise the convolution operation for processing input data. Rooted in neuroscientific principles and influenced by the visual cortex's structural organisation [132], CNNs gained widespread popularity after their success in the 2012 ImageNet Challenge [133]. Unlike fully connected networks, CNNs excel at handling spatial or grid-like data structures, such as time series, images, and videos, reducing trainable parameters due to their inherent weight-sharing properties. The subsequent section explores the convolution operation and its motivations and introduces various CNN iterations with illustrative examples.

III.4.4.2 The Convolution Operation

The convolution operation is formally defined as the integral of the product of two functions (f, g) after one function is reversed and shifted over the other. In mathematical terms, this can be expressed as:

$$h(t) = \int_{-\infty}^{\infty} f(t-\tau)g(\tau)d\tau \tag{3.16}$$

This operation can also be represented using an asterisk (*), denoting it as:

$$h(t) = (f * g)(t) \tag{3.17}$$

The convolution operation reveals the mutual influence between two functions rooted in signal processing concepts. Its operation originates from the need to understand how a filter affects a signal. It is exemplified with a one-dimensional continuous signal and a Gaussian filter, resulting in a smoothed version of the original input. Another perspective views convolution as illustrating the relationship between two functions, measuring similarity or dissimilarity at various relative positions. In deep learning, distinctions between convolution and cross-correlation may be secondary, but convolution possesses additional properties, including commutativity. When signals exhibit symmetry, both operations yield identical results. The convolution operation's definition extends to discrete and finite signals, formally defined for two signals, f [k] and g [k], where k is an integer. The convolution operation is formally defined as:

For discrete signals f[k] and g[k], where k belongs to the set of integers, the convolution operation is defined by:

$$h[k] = \sum_n f[k-n]g[n] \tag{3.18}$$

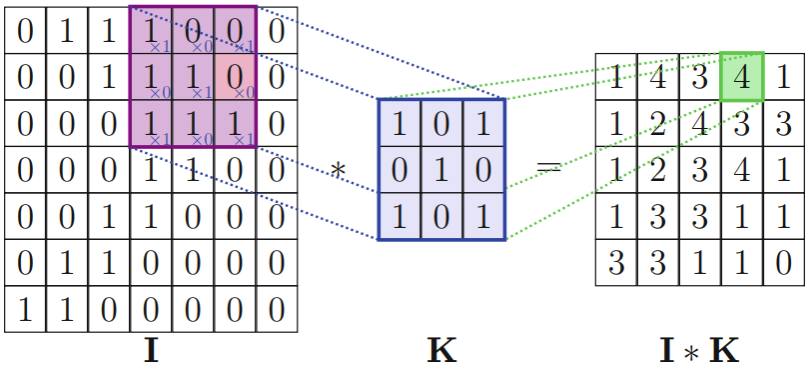


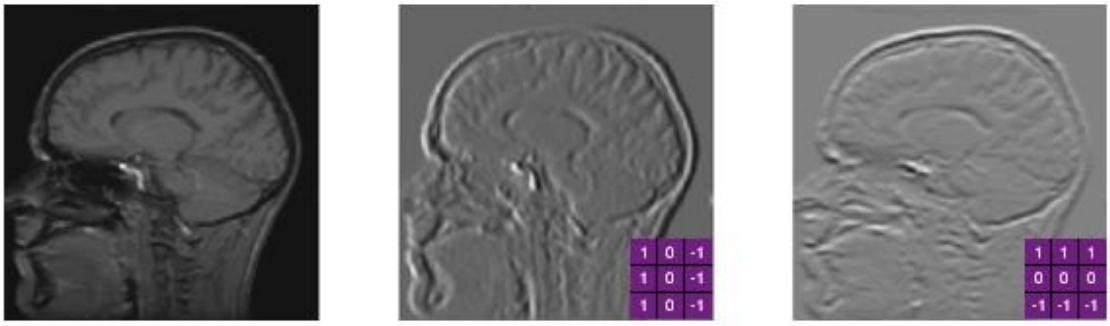
Figure III.12: 2D discrete convolution visualisation operation [134]

Finally, the convolution operation can be similarly extended to multidimensional signals. For instance, the convolution operation between two discrete and finite two-dimensional signals (e.g., I [i, j], K [i, j]) can be expressed as:

$$H[i,j] = \sum_m \sum_n I[i-m, j-n]K[m,n] \tag{3.19}$$

In many cases, a large-sized image is accompanied by a smaller-sized matrix called a kernel, which performs a specific operation. This kernel is typically 3 x 3 or 4 x 4 in size. Figure III.12 shows the convolution operation for a 2D discrete signal (such as an image) and a 3 x 3 kernel. The kernel moves across all input positions, performing element-wise

multiplication and summation to determine the convolution output at the corresponding location. Figure III.13 provides examples of how convolutions can be applied to an image. It is important to note that, similar to multilayer perceptrons, a convolution is usually followed by a non-linear activation function such as ReLu. (Figure III.14 shows an example of activation applied to a feature map.)



Original image Vertical edge detection Horizontal edge detection

Figure III.13: Original image with vertical and horizontal edge detection [134]

Figure III.13 illustrates two instances of convolutions applied to an image. One filter serves as a vertical edge detector, while the other functions as a horizontal edge detector. It is important to note that in Convolutional Neural Networks (CNNs), filters are learned rather than predefined. Therefore, there is no assurance that there will be a detector specifically for vertical or horizontal edges among the learned filters. However, in practice, this often occurs, particularly in the initial layers of the architecture.

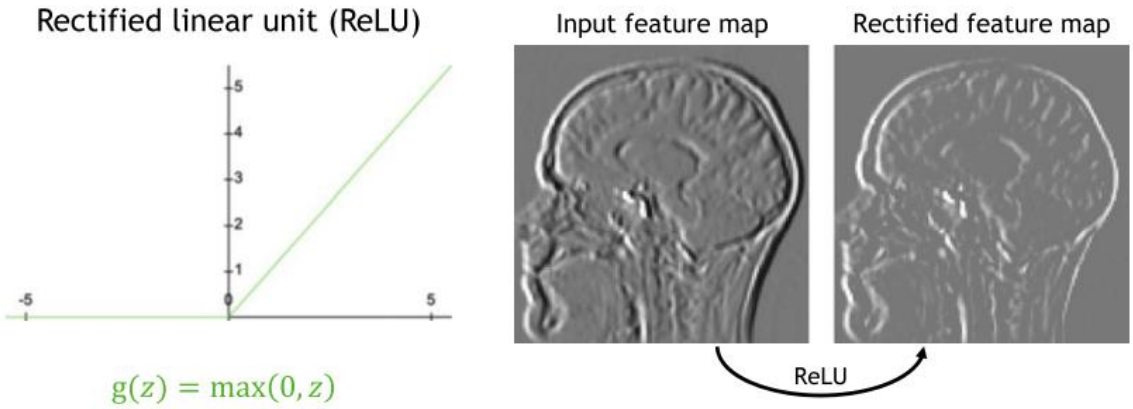


Figure III.14: Exploring Non-linear Activation: Applying ReLu to Image Transformation [134]

Figure III.14 demonstrates an instance of applying a non-linear activation function, specifically a Rectified Linear Unit (ReLu), to an image.

III.4.4.3 Characteristics of the Convolution Operation

In situations involving a discrete domain, the convolution operation can be efficiently performed using straightforward matrix multiplication, thereby eliminating the need to shift one signal over the other manually. This efficiency is achieved by employing a Toeplitz matrix transformation, which converts the convolution kernel into a sparse matrix. This matrix, characterised by its repetitive elements, allows for direct multiplication with the input signal to produce the convolutional output. To demonstrate how the convolution operation translates into matrix multiplication, consider the example of a 3 × 3 kernel (K) and a 4 × 4 input (I):

$$K = \begin{bmatrix} k_{00} & k_{01} & k_{02} \\ k_{10} & k_{11} & k_{12} \\ k_{20} & k_{21} & k_{22} \end{bmatrix} \text{ and } I = \begin{bmatrix} i_{00} & i_{01} & i_{02} & i_{03} \\ i_{10} & i_{11} & i_{12} & i_{13} \\ i_{20} & i_{21} & i_{22} & i_{23} \\ i_{30} & i_{31} & i_{32} & i_{33} \end{bmatrix}$$

Subsequently, the convolution operation can be computed by performing matrix multiplication involving the Toeplitz-transformed kernel:

$$K = \begin{bmatrix} k_{00} & k_{01} & k_{02} & 0 & k_{10} & k_{11} & k_{12} & 0 & k_{20} & k_{21} & k_{22} & 0 & 0 & 0 & 0 & 0 \\ 0 & k_{00} & k_{01} & k_{02} & 0 & k_{10} & k_{11} & k_{12} & 0 & k_{20} & k_{21} & k_{22} & 0 & 0 & 0 & 0 \\ 0 & 0 & 0 & 0 & k_{00} & k_{01} & k_{02} & 0 & k_{10} & k_{11} & k_{12} & 0 & k_{20} & k_{21} & k_{22} & 0 \\ 0 & 0 & 0 & 0 & 0 & k_{00} & k_{01} & k_{02} & 0 & k_{10} & k_{11} & k_{12} & 0 & k_{20} & k_{21} & k_{22} \end{bmatrix}$$

and a reshaped input:

$$I = [i_{00} \quad i_{01} \quad i_{02} \quad i_{03} \quad i_{10} \quad i_{11} \quad i_{12} \quad i_{13} \quad i_{20} \quad i_{21} \quad i_{22} \quad i_{23} \quad i_{30} \quad i_{31} \quad i_{32} \quad i_{33}]^{\mathsf{T}}$$

The resulting output is reshaped into a 2 × 2 matrix to obtain the convolution output. This approach of implementing matrix multiplication sheds light on fundamental properties of the convolution process, which are key reasons for its use in deep neural networks.

Transforming the convolution operation into matrix multiplication clearly demonstrates its alignment with the formalisation of linear functions. This alignment allows for the design of deep neural networks that utilise trainable convolution kernels. Typically, multiple convolution kernels are learned within each convolutional block, and stacking several such blocks builds deep Convolutional Neural Networks (CNNs). The outputs, commonly known as feature maps, are crucial for subsequent layers.

A significant advantage of the convolution operation is its parameter efficiency compared to networks with fully connected layers. The convolution matrix (K) illustrates that the same parameters are reused at every position, unlike in fully connected layers where unique parameters are needed for each input location. This parameter sharing, or weight sharing, drastically cuts down the memory needed to store network parameters. Figure III.15 illustrates how weight sharing operates across different spatial locations and how multiple filters within a single layer can produce a variety of feature maps.

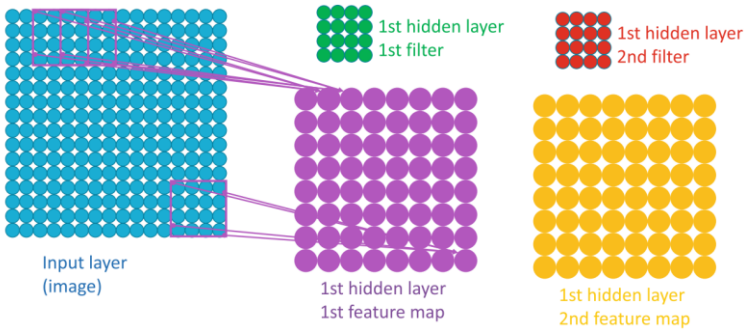


Figure III.15: Multi-Filter Learning in Convolutional Neural Networks

Figure III.15 shows a number of (typically many) filters are learned for a given layer, each of which can identify a distinct aspect of the image, producing a number of feature and filter maps. However, for a particular filter, the weights are shared by all of the image's places.

These feature maps for a specific layer are organised along an additional dimension, as shown in Figure III.16, leading to the formation of a 3D array when starting with a 2D input image (and a 4D array when the input is a 3D image).

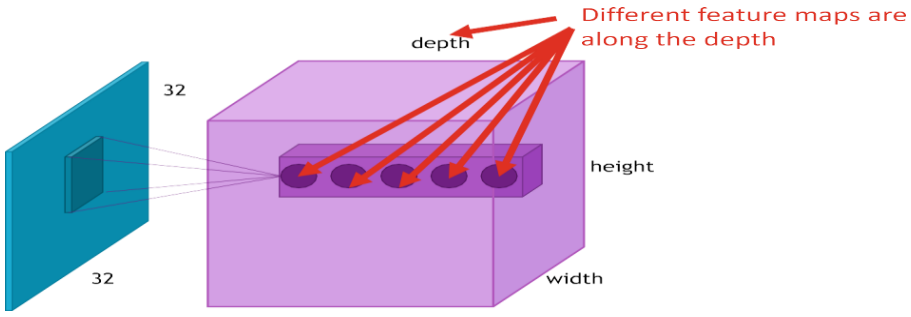


Figure III.16: Organised Feature Maps in Convolutional Neural Networks

Figure III.16 shows the various feature maps for a specific layer organised along an additional dimension. Consequently, the feature maps constitute a 3D array when the input

is a 2D image (and a 4D array when the input is a 3D image). This arrangement allows for effectively representing and handling the output generated by the convolutional layer in convolutional neural networks (CNNs).

Convolutional neural networks have proven to be powerful in processing data with spatial structure, such as images and videos. This effectiveness is based on the local connectivity of kernel elements, with the same kernel applied at different input locations. This processing grants a useful property called translation equivariance. Translation equivariance means that shifting the input of the network results in an equivalent shift in the output, a fundamental property for tasks involving spatial data, enabling the network to produce similar responses at different input locations. An example of the usefulness of this property is evident in an image detection task where the model should respond similarly to anomalies regardless of their location, such as detecting tumours in a Magnetic Resonance Image (MRI) of the brain. Finally, a crucial characteristic of the convolution process is its ability to separate the size of the input from the parameters that can be trained. Unlike in Multilayer Perceptrons (MLPs), where the dimensions of the weight matrix are tied to the size of the input, the parameters that can be trained in convolutional layers are solely determined by the size of the kernel and the number of kernels per layer. This distinction permits the handling of inputs of any size, as demonstrated by fully convolutional networks.

III.4.4.4 Functions and Variants

It has been observed that the convolution operation can alter the dimensionality of the resulting output. For example, in Figure III.17, convolving a 7×7 image with a 3×3 kernel produces a feature map of size 5×5. Although changes in dimension can be avoided by applying suitable padding before the convolution operation—as illustrated in Figure III.17—there are instances where intentionally reducing the input dimensions is beneficial. This reduction is typically employed to decrease computational complexity and progressively enlarge the receptive field of the convolutional layers.

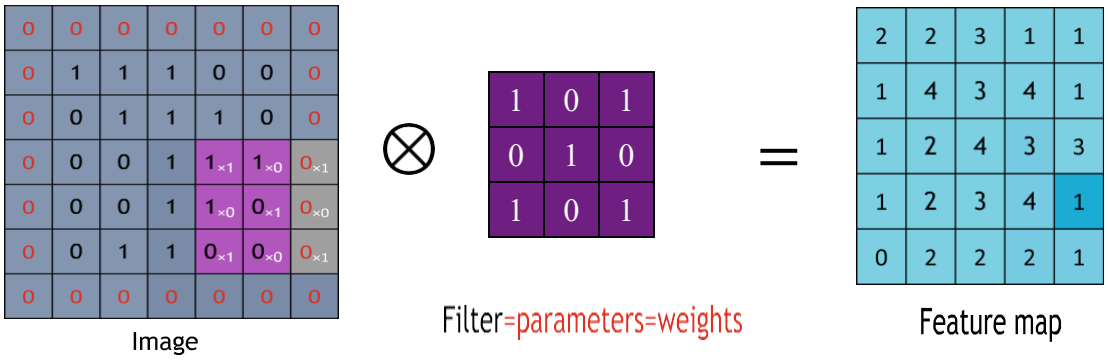


Figure III.17: Exploring Padding Operations in Convolutional Neural Networks

Figure III.17 illustrates the padding operation, which involves adding zeros around the perimeter of an image. This technique, known as zero-padding, allows the generation of feature maps that retain the same spatial dimensions as the original image. Padding is a crucial strategy in Convolutional Neural Networks (CNNs) to manage the output dimensions and to avoid unwanted reductions in size during the convolution process. The choice of padding type can vary depending on the specific requirements of the task at hand. This subsection will explore some of the most prevalent padding strategies employed in CNNs to achieve this objective.

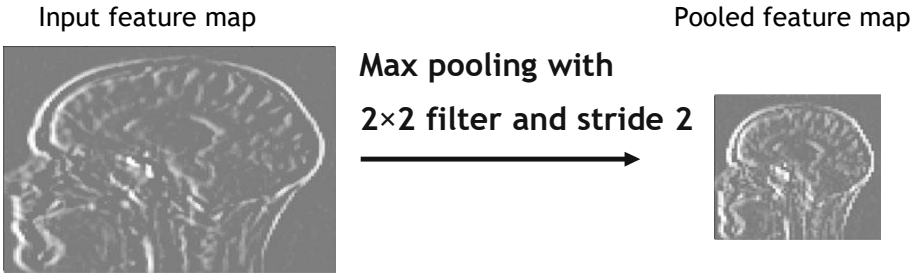


Figure III.18: Visualising Pooling Effects: Maximum Pooling with 2x2 Dimensions and Stride 2 [134]

Figure III.18 illustrates the impact of a pooling process. In this instance, maximum pooling with dimensions 2 × 2 and a stride of 2 is applied.

Downsampling Operations (i.e., Pooling Layers): In many CNN designs, down-sampling methods are heavily utilised to reduce the size of feature maps and decrease computational demands. These methods, known as pooling layers, compress the input values based on the type of pooling applied, effectively summarising the features present in various regions. Common types of down-sampling include maximum pooling, average pooling, and global average pooling. Maximum and average pooling extract the highest or average values

from predefined, non-overlapping regions within the feature map, respectively. Global average pooling, on the other hand, calculates the average value across all spatial dimensions of the feature map, providing a single output per feature map which significantly reduces the data volume. An illustration of these pooling processes can be seen in Fig. III.18.

Stride Convolution refers to a specific approach in convolution operations where, instead of conducting the convolution at every single pixel location (stride of 1), larger step sizes or strides are utilised (refer to Figure III.19). Employing a stride greater than 1 result in a convolution output that contains significantly fewer elements, effectively reducing the spatial dimensions of the feature maps. This technique is particularly useful in deep learning architectures; convolutional blocks with strides greater than 1 are frequently incorporated into CNNs to compress feature maps in intermediate layers, thereby streamlining the network by reducing computational load and memory usage.

Dilated Convolution (Atrous) involves using kernels that have been expanded by inserting zero-spaced holes between the non-zero elements. This technique introduces an additional parameter, the dilation rate (d), which dictates the spacing between the kernel elements. By doing so, it allows the kernel to encompass a broader area of the input, thereby extending its reach without increasing the number of trainable parameters. For example, applying a dilation rate of d =2 to a 3 × 3 kernel expands it such that it covers a 5 × 5 area of the input, though the kernel itself remains sparse.

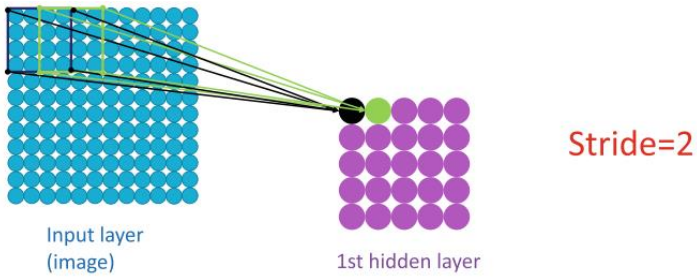


Figure III.19: Stride Operation (Stride of 2)

Transposed Convolution is essential in scenarios where network architectures require not only down-sampling but also up-sampling of spatial dimensions, particularly in later stages. A common application is image segmentation, where the goal is pixel-level classification, necessitating that the network's output spatial dimensions match those of the input. Transposed convolution is one such up-sampling technique used to increase the size of the output feature maps.

In this process, transposed convolution involves interspersing zeros among the input feature map elements—a technique often termed 'fractionally strided convolution.' For example, applying transposed convolution to a 5 × 5 input using a stride of 2 and a 3 × 3 kernel can expand the feature map to 10 × 10. This size increase is adjusted by the stride and the kernel size, ensuring that the output precisely aligns with the required up-sampling factor.

III.4.4.5 Receptive Field Calculation

In deep neural networks, particularly Convolutional Neural Networks (CNNs), the 'receptive field' refers to the portion of the input that contributes to creating a specific output feature. For instance, if a CNN processes an image using a single convolution layer with a 3 × 3 kernel, the receptive field for each element of the resulting feature map is also 3 × 3. This means a 3 × 3 region of the input is used to compute each pixel in the first feature map. Adding another convolution layer with a 3 × 3 kernel increases the receptive field to 5 × 5 for the second layer's output. This expansion occurs because each new layer compounds the area of input influencing its calculations, encompassing the adjacent elements around the original receptive field.

Understanding the receptive field's size at various points within a CNN is crucial for analysing the network’s ability to integrate information across the input image. For a CNN tasked with processing a 256 × 256 image, where comprehensive input integration is necessary, the receptive field should ideally encompass nearly the entire input dimensions by the final layers. The receptive field's dynamics are shaped by the convolution parameters as well as any employed down/up-sampling operations, as discussed earlier. For detailed mathematical formulas and further discussion on receptive field calculations in CNNs, refer to the comprehensive resource in [135].

III.4.4.6 Convolutional Neural Network Architectures

Over the past few decades, numerous convolutional neural network (CNN) architectures have been developed, each suited to a variety of tasks. This chapter will focus on a selection of classical architectures that are primarily designed for classification tasks. Notably, while these architectures are versatile enough to be adapted for different objectives, the primary distinction in their application for classification lies in the choice of the loss

function, such as cross-entropy. Architectures that are specifically tailored for other tasks, such as object detection or segmentation, are discussed in separate chapters.

III.4.4.7 A Basic CNN Architecture

The initial architecture we consider is the simplest form of a CNN, closely resembling the 'LeNet' originally proposed by LeCun et al. [136]. This architecture consists of two main components: the first uses convolution operations to extract features from the image, which are then flattened; the second channels these flattened features into a series of fully connected layers, forming a multilayer perceptron for classification or regression tasks (see Figure III.20). The entire network undergoes end-to-end training without independent training of its two sections. The convolutional segment integrates blocks that include convolution operations—possibly with striding or dilation—alongside a non-linear activation function, such as ReLU, and a pooling operation.

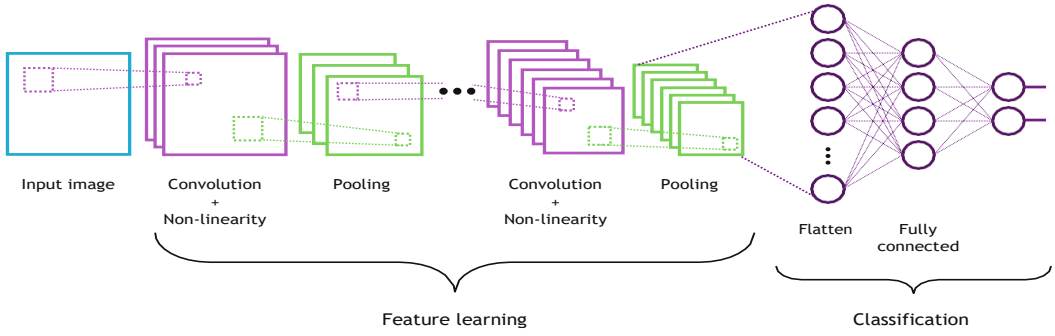


Figure III.20: Unveiling CNN Architecture - From Convolutional Feature Extraction to Multilayer Perceptron Classification [134]

Figure III.20 illustrates a fundamental CNN architecture, traditionally consisting of two primary components. The first part employs convolution operations to conduct feature learning, and the extracted features are subsequently flattened. These flattened features are input into a series of fully connected layers, forming a multilayer perceptron. This final stage is responsible for executing the classification or regression task.

III.4.4.8 Classification of images using deep learning

Except for methods using machine learning, deep learning approaches offer surprisingly better accuracy in computer vision. Classification systems based on machine learning enable the extraction of features from images using specific algorithms, such as Scale-Invariant Feature Transform (SIFT). Therefore, a crucial aspect of machine learning

involves leveraging extracted features for system learning. In contrast, deep learning addresses this issue using a CNN that automatically extracts and classifies features (Figure III.21).

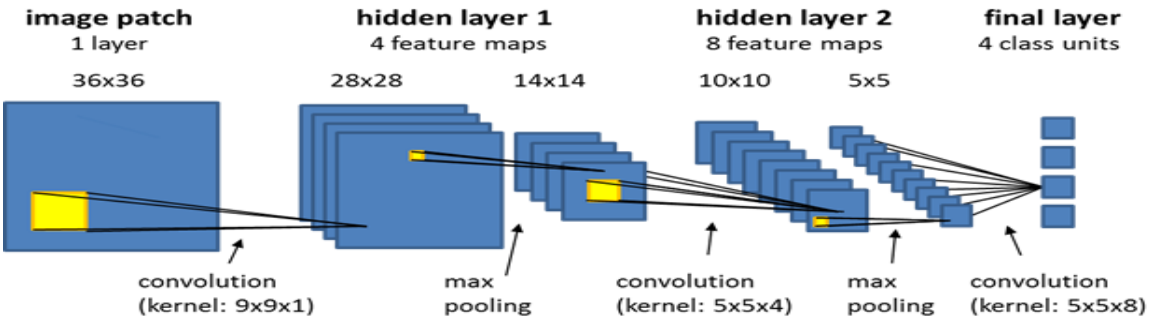


Figure III.21: Deep Learning (CNN) [137]

The first layer of the CNN learns small details of the image; the subsequent layers combine the previous features to create more complex information. In the convolutional neural network, feature extraction is done using filters. The network applies filters to the image to see if there is a match, meaning that the element's shape is identical to a part of the image. Indeed, the process of feature extraction is thus done automatically.

III.4.4.9 Measures to assess the performance of the classification system

This section presents metrics designed to evaluate how well the classifier performs in accurately predicting the class labels of images. The classifier metrics include recognition rate (overall accuracy), recall (or sensitivity), specificity, precision, and the F-measure.

Table III.6 offers more comprehensive information on the formulas for computing these metrics. Furthermore, let us consider the application of our classifier to a labelled test set of images, where P denotes the count of positive images and N represents the count of negative images.

Precision is a distinct metric, given that this term is also employed more broadly to characterise a classifier's predictive capabilities.

- True Positives, or abbreviated as TP, refer to the number of correctly predicted positive values. This indicates instances where the actual class value is 'yes,' and the predicted class value is also 'yes.'

Measure	Formula
recognition rate	$\frac{TP + TN}{P + N}$
Error rate	$\frac{TP + FN}{P + N}$
Recall	$\frac{TP}{P}$
Specificity	$\frac{TN}{N}$
Precision	$\frac{TP}{TP + FP}$
F, F-measure, harmonic mean of precision and recall	$\frac{2 * \text{précision} * \text{recall}}{\text{précision} + \text{recall}}$

Table III.6: Evaluation measures [137]

- False Positives (FP): Let FP be the number of false positives where the actual class is negative and the predicted class is positive, i.e., these are the negative values incorrectly labelled as positive.
- False Negatives (FN): Consider FN as the count of instances where the true class is positive but the predicted class is negative. In other words, these positive values have been inaccurately classified as negative.
- True Negatives (TN): Let TN represent the count of true negatives. These are the correctly predicted negative values, meaning that the actual class value is negative, and the predicted class value is also negative.
- TP (True Positives) and TN (True Negatives) are indicative of correct classifier predictions, whereas FP (False Positives) and FN (False Negatives) highlight situations where the classifier makes mistakes, meaning incorrect classifications.

The confusion matrix, also known as the contingency table, according to Fawcett [138], is a valuable instrument for assessing a classifier's effectiveness in recognising and predicting images belonging to various classes. This matrix is useful for assessing the classifier's ability to identify images from different classes. It is structured as a table with dimensions (n x n), where n represents the number of classes. In this matrix, each column corresponds to the predicted classifications, while each row represents the actual defined classifications.

Table III.7: Confusion Matrix [137]

Real class	**Predicted class**	
	True Positive	False Negative
	False Positive	True Negative

The entries along the diagonal of the confusion matrix indicate accurate classification with the highest precision, while entries off the diagonal indicate classification errors. Table III.7 shows the confusion matrix for two classes with four entries.

III.5 Conclusion

In this chapter, we explored the seamless integration of IoT and AI, emphasising their rapid convergence. We introduced powerful optimisation algorithms, specifically GA and PSO, which are precisely utilised to optimise the WT and identify optimal parameters for reducing noise interference in ECG signal recordings. This advancement fosters a hybrid methodology that leverages the synergistic effects of these algorithms with WT, further detailed in the following section. This approach streamlines the preprocessing of ECG data, thereby enhancing efficiency. Additionally, we delve deeper into the integration of CNN into healthcare applications, highlighting essential functions such as remote patient monitoring and smart diagnosis. Despite global challenges like the digital divide and unequal access to digital healthcare technologies, the transformative potential of AI and IoT in healthcare is undeniably evident. The subsequent sections will provide a comprehensive analysis, meticulously detailing the step-by-step processes employed in our research endeavours.

Chapter IV

Experimental Results and Performance Evaluation

IV.1 Introduction

This chapter thoroughly examines the effectiveness of PSO-WT and GA-WT techniques in reducing noise from ECG signals, specifically targeting prevalent noise types such as PLI and AWGN. As critical pre-processing steps, these methods significantly improve signal quality, which is essential for accurate classification. By transforming ECG signals into a 2D matrix and extracting features using 2D-DWT, both PSO and GA iteratively fine-tune the WT parameters. The resultant denoised signals are then efficiently incorporated into a CNN for classification.

IV.2 PSO and WT for noise reduction in ECG signals

This section provides a detailed examination of the proposed PSO-WT method, which utilises PSO combined with WT to denoise ECG signals. ECG signals are frequently corrupted by various types of noise, presenting a substantial challenge. The PSO-WT approach addresses this by optimising wavelet parameters specifically for the denoising of ECG signals. The steps of the PSO-WT denoising method, as illustrated in Figure IV.1, are summarised as follows:

Input: An ECG signal corrupted by noise, alongside initial wavelet denoising parameters: (Φ, L, β, λ, ρ).

Processing Steps:

a. Parameter Initialisation: Establish appropriate ranges for the wavelet denoising parameters and develop objective functions that incorporate the Signal-to-Noise Ratio (SNR) to evaluate denoising performance.
b. Parameter Optimisation: Utilise PSO to fine-tune the wavelet denoising parameters, selecting the set that maximises noise reduction efficacy.
c. Wavelet Transform: Apply the WT to the noisy ECG data to extract all wavelet coefficients.

d. Threshold Application: Implement the optimised thresholds to purify the noisy wavelet coefficients of the ECG signal, effectively modifying and enhancing the signal components.

Output: A reconstructed ECG signal is denoised using the optimised wavelet parameters.

The summary of the proposed method is provided in Algorithm 3.

Algorithm 3. Applying PSO Algorithms to Tune WT Parameters for ECG Signal Denoising

1: Initialise noisy ECG signal (nECG), and calculate the SNR, MSE, RMSE, and PRD for input ECG signal.
2: Initialise PSO operators, initialise solution(s)
X_i (i = 1, 2, … Np) Np = 5 wavelet parameters,
The initial solution X_i (Φ, L, β, λ, ρ)
3: $X'opt$ = PSO (X, X_i)
4: ECG Denoised = WT ($X'opt$, nECG)
5: ECG Out Signals = Evaluate (ECG Denoised, SNRout, SNRimp, MSE, RMSE, PRD).

Detailed explanations of the proposed technique are outlined in the subsequent phases:

Phase I: Initialisation. Encompasses three critical stages. The process starts with signal acquisition, where the input ECG signal, S(n), is obtained from the source. Following this, the Noise Identification stage employs the WT denoising method to specifically address the degradation of the ECG signal by White Gaussian Noise (WGN, refer to Equation 4.1) and Power Line Interference (PLI, refer to Equation 4.2). The final stage, Dataset Preparation, involves using these types of noise to mimic real-world disturbances that might taint the ECG signal during its recording. This artificially corrupted signal creates a varied dataset that is instrumental in assessing the efficacy of the proposed denoising method.

$$N(t) = s(t) + \sigma \tag{4.1}$$

$$N(t) = A\,sin\,(2\pi ft) \tag{4.2}$$

The second step of this phase involves initialising the WT denoising parameters (Φ, L, β, λ, ρ) from the ranges provided in Table III.2. The PSO parameters are configured as follows: $C_1 = 2$, $C_2 = 2$, $N_P = 5$, $itermax = 50$, $pop_size = 100$. C_1 and C_2 represent the acceleration constants, N_p is the number of WT parameters, $itermax$ is the maximum number of iterations, and pop_size is the population size. Finally, compute the SNR using equations (4.3), (4.4), and (4.5), PRD using equation (4.15), MSE by equation (4.13), and

root MSE (RMSE) according to equation (4.14). ECG signal data will be recorded both before and after the denoising operation.

Phase II: PSO-based parameter tuning of WT.

PSO is utilised by the proposed method to determine the optimal WT parameters for ECG signal denoising. At the outset, the arrangement of the WT parameters is denoted by the vector $x = (x_1, x_2, \dots, x_n)$, where n denote the number of WT parameters equal to 5. Where, x_1 denotes the value of the mother WT function's parameter Φ; x_2 represents the value of the level of decomposition parameter L; x_3 describes the approach taken to establish a threshold β; x_4 specifies the thresholding selection rule for the parameter value λ; and x_5 operates the rescaling method ρ, the range of these parameter values is determined from Table III.2. An illustration of a WT parameter solution for ECG signal denoising is presented in Figure IV.3. The PSO algorithm utilises the objective function SNR to assess the outcome, which is specified as follows:

$$SNR_{imp} = SNR_{output} - SNR_{input} \tag{4.3}$$

Where SNR_{input} and SNR_{output} are as follows:

$$SNR_{input} = 10log_{10} \frac{\sum_{n=1}^{N}[S(n)]^2}{\sum_{n=1}^{N}[S(n) - \tilde{S}(n))]^2} \tag{4.4}$$

$$SNR_{output} = 10log_{10} \frac{\sum_{n=1}^{N}[S(n)]^2}{\sum_{n=1}^{N}[S\left(n) - \hat{S}(n)\right)]^2} \tag{4.5}$$

The $S(n)$ denotes the initial ECG signal; $\tilde{S}(n)$ represents the ECG signal with noise; and $\hat{S}(n)$ signifies the denoised ECG signal obtained by adjusting wavelet parameters via the PSO algorithm. This process iteratively improves the randomly generated solution. The result of this phase is an optimised solution $x'_{opt} = (x'_1, x'_2, .., x'_n)$ that will proceed to the next phase.

Phase III: Noise Removal Using Wavelet Transform (WT). This process relies on the optimised solution x'_{opt} and comprises three main stages, illustrated in Figure III.5 and elaborated upon below:

- **Decomposition of ECG signals using DWT:** The DWT eliminates the disturbance in the input ECG signal $S(n)$ during this phase. In the decomposition procedure, it is

necessary to utilise the initial and subsequent x'_{opt} parameters, which are the mother wavelet Φ and the level of decomposition L. Each of the three levels of the DWT technique depicted in Figure IV.2 separates the noisy ECG data into cA and cD. Following this, the former is decomposed and passed through a low-pass filter, while the latter is subjected to a high-pass filter. The ECG signal is convolved with the assistance of low-pass and high-pass filters. Block (↓2) represents the downsampling operator, which is employed to preserve the even indicator components of the ECG signal in accordance with their frequency and frequency intensity. From the ECG signal, cA and cD are extracted.

- **Thresholding:** The second stage in the ECG denoising process involves applying a thresholding technique to the wavelet coefficients derived from the DWT. This step is critical and is directly contingent upon the estimated noise level in the coefficients. During this stage, it is necessary to select thresholding techniques (ρ), thresholding selection criteria (λ), and thresholding type (β) from the x'_{opt}. The assessment of the ECG signal's denoising can be achieved by subjecting the noisy and non-stationary signal $\hat{X}$ to a thresholding technique (Equation (4.6)), as described in reference[139]:

$$Z = THR(\hat{X}, \delta) \tag{4.6}$$

In this context, THR denotes the thresholding function, and δ signifies the threshold value. The estimation of δ is critical to the efficacy of ECG noise removal in the wavelet domain. Consequently, numerous estimation methodologies have been proposed. Donoho and Johnstone [109] established the following threshold in Equation (4.7):

$$\delta = \sigma\sqrt{2logM} \tag{4.7}$$

M denotes the length vector of the DWT coefficients, while σ represents their standard deviation.

Assuming it is solely dependent on cD and cA has the highest energy and lowest frequency among all ECG signals, we approximate the threshold value as follows using the coefficient levels specified in Equation (4.8):

$$\hat{x}_d(l) = THR(\hat{x}_d(l), \delta_l), l = 1,2, \ldots \tag{4.8}$$

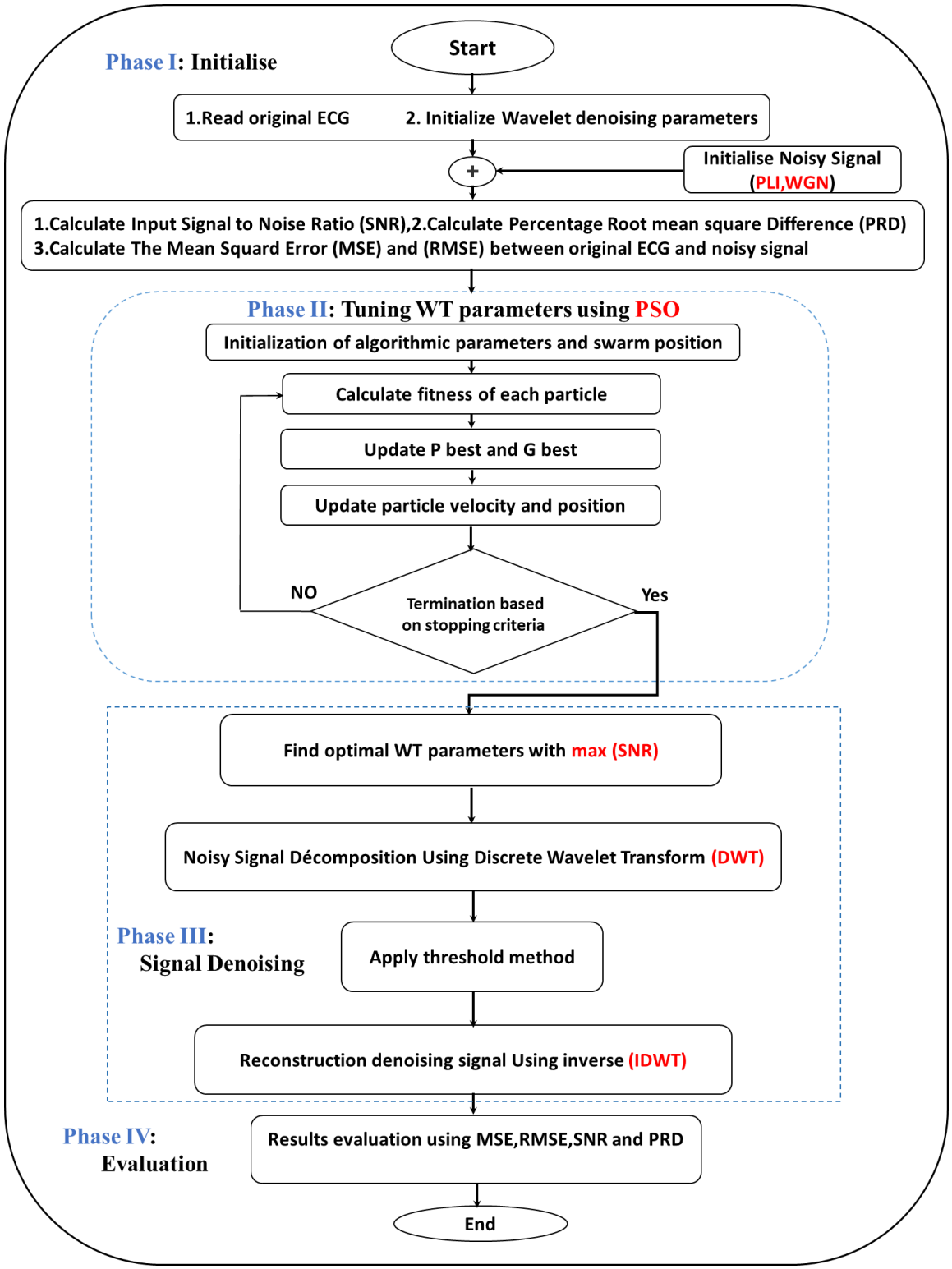


Figure IV.1: The proposed PSO-WT method [111]

In this context, l represents the WT decomposition level, $\hat{x}_d$ signifies the vector of DWT threshold detailed coefficients, and δ_l is a threshold value assigned to said level. As

previously observed, Figure III.7 illustrates that the wavelet generally offers two distinct varieties of thresholding-specific functions (β): hard thresholding and soft thresholding.

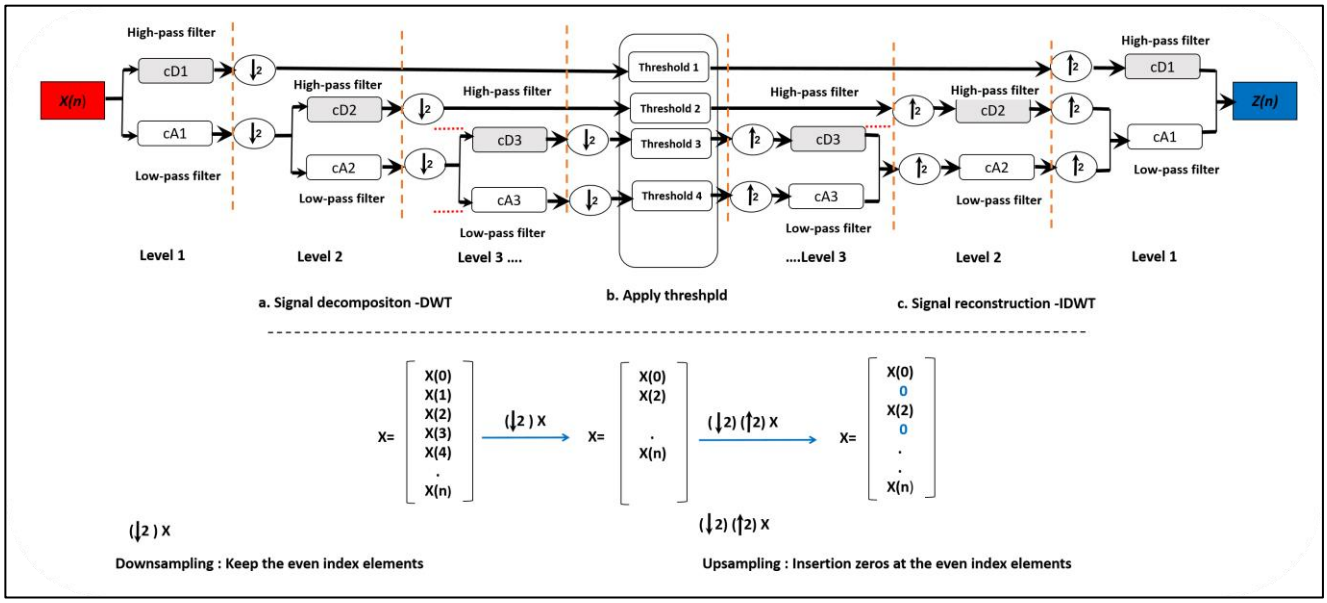


Figure IV.2: ECG denoising procedure [111]

In accordance with Equations (4.9) and (4.10), respectively, the following are explanations of the differences between hard and soft thresholding methods:

$$\hat{x}_{di}(l) = \begin{cases} \hat{x}_{di}(l) - |\delta_l| & |\hat{x}_{di}(l)| \geq \delta_l \\ 0 & |\hat{x}_{di}(l)| < \delta_l \end{cases} \tag{4.9}$$

$$\hat{x}_{di}(l) = \begin{cases} \hat{x}_{di}(l) & |\hat{x}_{di}(l)| \geq \delta_l \\ 0 & |\hat{x}_{di}(l)| < \delta_l \end{cases} \tag{4.10}$$

At level l, i denotes the detailed coefficient index at DWT. The DWT thresholding coefficients are summarised in Equation (4.11).

$$\hat{X} = [\hat{x}_d(1)\ \hat{x}_d(2)\ \hat{x}_a(2)] \tag{4.11}$$

- **Denoised ECG signal reconstruction using iDWT:** Equation (4.12), when applied to $\hat{X}$ in conjunction with iDWT, is utilised to compute the initial ECG signal:

$$z[n] = \sum_{k=-\infty}^{\infty} cA_L(K)\ \Phi'_i(n-k) + \sum_{i=1}^{L} \sum_{k=-\infty}^{\infty} cD_{i+1}(K)\Psi'_i(n-k) \tag{4.12}$$

Upsampling (↑2)) is employed to convolve the ECG signals, a process that involves appending zeros to the even index components. Illustratively, the iDWT technique for three levels is illustrated in Figure IV.2.

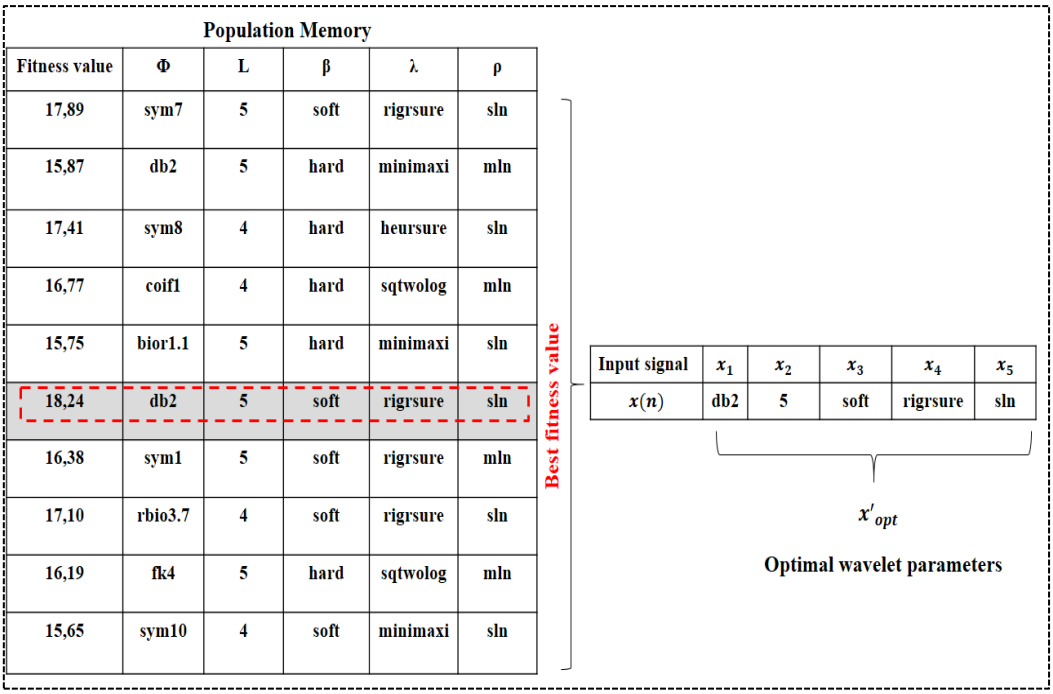


Figure IV.3. PSO-optimal WT configuration for removing noise from ECG signals [111]

Phase IV: Assessment of ECG Outcomes:

After processing by WT, the denoised ECG signals are rigorously evaluated. This assessment utilises the following key metrics:

Signal-to-Noise Ratio (SNR): Measures the quality of the ECG signal relative to the background noise.

SNR Enhancement: Quantifies the improvement in SNR as a result of the denoising process.

Mean Squared Error (MSE): Assesses the average squared difference between the original and denoised signals, as defined in Equation (4.13).

Root Mean Squared Error (RMSE): Provides the square root of MSE, offering a more interpretable measure of error magnitude, detailed in Equation (4.14).

Percentage Root Mean Square Difference (PRD): Evaluates the error relative to the signal's original amplitude, specified in Equation (4.15).

These metrics collectively offer a comprehensive view of the denoising efficacy and signal fidelity post-WT treatment.

$$MSE = \frac{1}{N}\sum_{n=1}^{N}(S(n) - \hat{S}(n))^2 \quad (4.13)$$

$$RMSE = \sqrt{\sum_{n=1}^{N}\frac{1}{N}[S\left(n\right) - \hat{S}(n)\Big)]^2} \quad (4.14)$$

$$PRD = 100 * \sqrt{\frac{\sum_{n=1}^{N}[S(n) - \hat{S}(n)]^2}{\sum_{n=1}^{N}[S(n)]^2}} \quad (4.15)$$

In this context, $S(n)$ denotes the clean ECG signal, $\tilde{S}(n)$ signifies the noisy ECG signal, and $\hat{S}(n)$ signifies the denoised ECG signal produced by adjusting the WT parameters using the designated PSO method. N signifies the number of samples.

IV.2.1 Results and Discussions

To assess the effectiveness of filtration in the proposed method, we downloaded a number of records from the MIT-BIH database [140] ,which is widely recognised and accessible to the public. An ECG record possesses the subsequent attributes: a sample length of 650,000, a sampling rate of 360 Hz, an 11-bit resolution spanning a 10-mV range, and a bit rate of 3960 bps. In the literature, this database is frequently used as a standard against which to compare various noise-removal techniques.

In this study, we presented two kinds of noise for refining ECG signals: WGN and PLI. Through experimental selection, we fine-tuned these parameters to enhance their effectiveness. We introduced PSO as a method to derive an optimal configuration of parameters for noise reduction. The parameters earmarked for optimisation are detailed in Table III.2.

In this study, the parameters for wavelet noise removal were fine-tuned using MATLAB 2018b software. The specific parameters employed for PSO analysis were as follows: $C_1 = 2, C_2 = 2, N_P = 5, itermax = 50$, and $pop_size = 100$. The convergence criterion for fitness determined the stopping point.

IV.2.1.1 AWGN Removal

The optimised parameters for wavelet denoising, achieved through PSO, are outlined in Table VI.1. It is often unclear whether a single wavelet can effectively remove noise. Our investigation revealed varying degrees of success among different wavelets in noise reduction. Orthogonal WTs like Coiflets and Symlets offer distinct advantages, being compact and allowing for accurate reproduction of the original signal without distortion [141]. Based on the results obtained, the Coiflets wavelet family is more effective for ECGs heavily contaminated by noise, whereas the Symlets family is better suited for ECGs with

lower noise levels. The optimal decomposition level directly corresponds to the noise level, with levels 7–8 recommended for high noise and levels 3–4 for low noise. Despite its simplicity, the soft thresholding method frequently outperforms the hard thresholding approach. Among the three thresholding rescaling techniques, the 'sln' (single-level noise) method demonstrated the highest efficacy, followed by the 'rigrsure' technique, which also showed notable efficiency. In our experimentation, conducted with 16 ECG records from the MIT-BIH database, we utilised PSO to determine the optimal wavelet denoising parameters, using SNR improvement as the fitness function.

Following the filtration process, average values for SNR, PRD, MSE, and RMSE are computed for the signal. Table VI.2 showcases the outcomes of the ECG signal after denoising using the PSO-WT denoising technique. SNRinput values ranged from -5 dB to 30 dB with a step size of 5 dB. An illustration of the obtained result is presented in Figure IV.4, featuring record number 100 from the MIT-BIH database. The figure comprises the original signal (Figure IV.4-a), the noisy signal (Figure IV.4-b), and the denoised signal (Figure IV.4-c) generated through the proposed method. It's evident that the denoised signal closely resembles the original ECG, affirming the efficacy of the proposed approach.

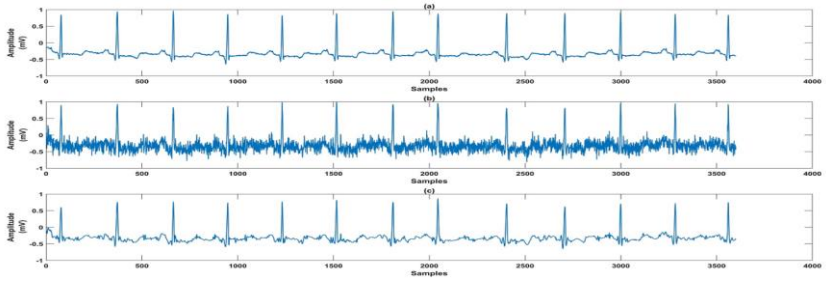


Figure IV.4: (a) Illustration of the clean ECG signal (one sample), (b) ECG signal corrupted with noise at SNRinput = 10 dB, (c) Denoised ECG signal obtained using the proposed technique (φ = sym3, β = soft, λ = rigsure, L = 5, and ρ = sln) yielding SNRoutput = 18.24 dB.

Additionally, the proposed method demonstrates notable results for a noisy signal with SNR input of 10 dB, yielding a PRD of 13.47 and an output SNR of 18.24, marking a significant improvement of 8.24 in SNR. Figure IV.5(a) illustrates the relationship between input and output SNR, showcasing an almost linear correlation, indicating their direct proportionality. As SNR input increases, SNR output also rises. Figure IV.5(b) presents a graphical representation of the PRD between the original and denoised ECG signals, with

detailed values available in Table VI.2. It's observed that the proposed method performs smoother with lower noise levels, as evidenced by lower PRD values, denoting efficient signal denoising. Figures IV.5(c) and IV.5(e) depict the MSE and RMSE between the original and denoised ECG signals. It's noteworthy that MSE and RMSE values exhibit an inverse relationship with SNRinput values.

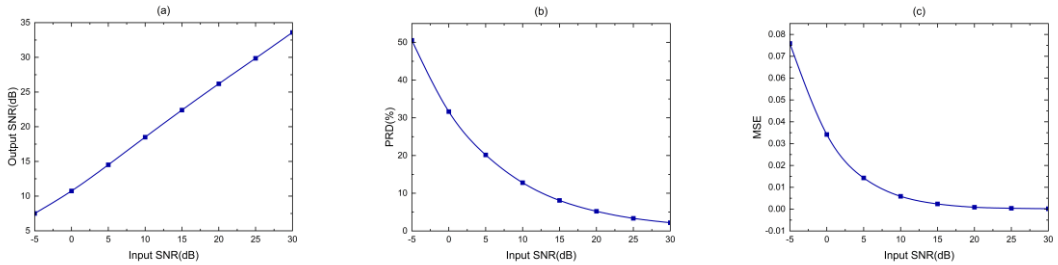
Table VI.1: The PSO-derived optimal parameters for wavelet denoising of the tested signal.

WT denoising parameters	SNR input values		
	SNR in < 10 dB	10 dB < SNR in < 25 dB	SNR in > 25 dB
The type of wavelet basis function φ	Coif 3	Sym 3	Sym 18
Thresholding function β	soft	soft	soft
Decomposition level L	8,7	6,5	4,3
Thresholding selection rule λ	rigsure	rigsure	rigsure
Rescaling approach ρ	sln	sln	sln

Table VI.2: Evaluation of ECG signal denoising efficacy across varying input SNR levels

Input SNR (dB)	Output SNR (dB)	Improvement SNR (dB)	MSE	RMSE	PRD %
-5	7.5034	12.5740	0.0759	0.2550	50.5431
0	10.7463	10.8169	0.0342	0.1701	31.6505
5	14.5189	9.5895	0.0143	0.1103	20.1725
10	18.4955	8.5661	0.0059	0.0708	12.8114
15	22.3989	7 .4695	0.0024	0.0448	8.1116
20	26.1904	6 .2610	0.0009	0.0287	5.2273
25	29.8667	4.9373	0.0004	0.0184	3.3552
30	33.5884	3.5416	0.0002	0.0121	2.2019

The enhancement in SNR achieved by the proposed method is determined by the disparity between SNR output (dB) and SNR input (dB), offering insight into the noise elimination performance.



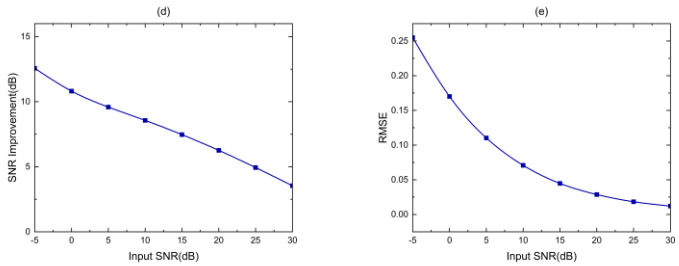


Figure IV.5: illustrates: (a) The relation between SNRoutput and SNRinput, (b) PRD with SNRinput, (c) MSE varying with SNRinput, (d) SNR Improvement with SNRinput, and (e) RMSE with SNRinput.

Figure IV.5(d) illustrates the correlation between SNR improvement and SNRinput. Notably, greater SNR enhancements occur at lower SNRinput levels, indicating that our method excels particularly in scenarios with substantial noise levels.

A comprehensive comparison is conducted to evaluate the enhancements in SNR and PRD achieved by the proposed denoising method against more than 10 other state-of-the-art noise removal techniques [36] all utilising the same database. These comparisons are detailed in Figure IV.6. Given that the reported outcomes in literature originate from various SNRinput values applied to different records sourced from the MIT-BIH database, we categorise our comparisons based on SNRinput values and the ECG records utilised by the corresponding techniques. Consequently, we compare our results against EMD with an NLM (EMD-NLM)[142], conventional filtering (CF) [143], and NLM denoising of ECG signals (NLM) [144]. using four SNRinput values (-5, 0, 5, and 10) with record 100, as illustrated in Figures IV.6 (a) and IV.6 (b). Furthermore, a comparison involving three SNRinput values (-5, 0, and 5) with record 103 is made against the IHP-ST EMD [145] and SF methods [146], depicted in Figure IV.6(c) and Figure IV.6(d).Another comparison based on two values of SNR_{input} (5 and 10) using records 100 and 103 is made against the following techniques: EMD-ASMF [147], SDCST [148], NIWT [149], 1DTVD [150], and GAMNVE [151], as depicted in Figures IV.6(e), IV.6(f), IV.6(g), and IV.6(h). It is evident from Figure IV.6 that the proposed method surpasses all other contemporary techniques across all SNRinput levels in terms of SNR enhancements and achieves the lowest PRD values. Hence, the PSO-based approach has effectively optimised the parameters for wavelet denoising of ECG signals, resulting in superior performance compared to existing techniques. Moreover, it is noticeable that the obtained SNR improvements for the ECG signal are vulnerable to high levels of noise.

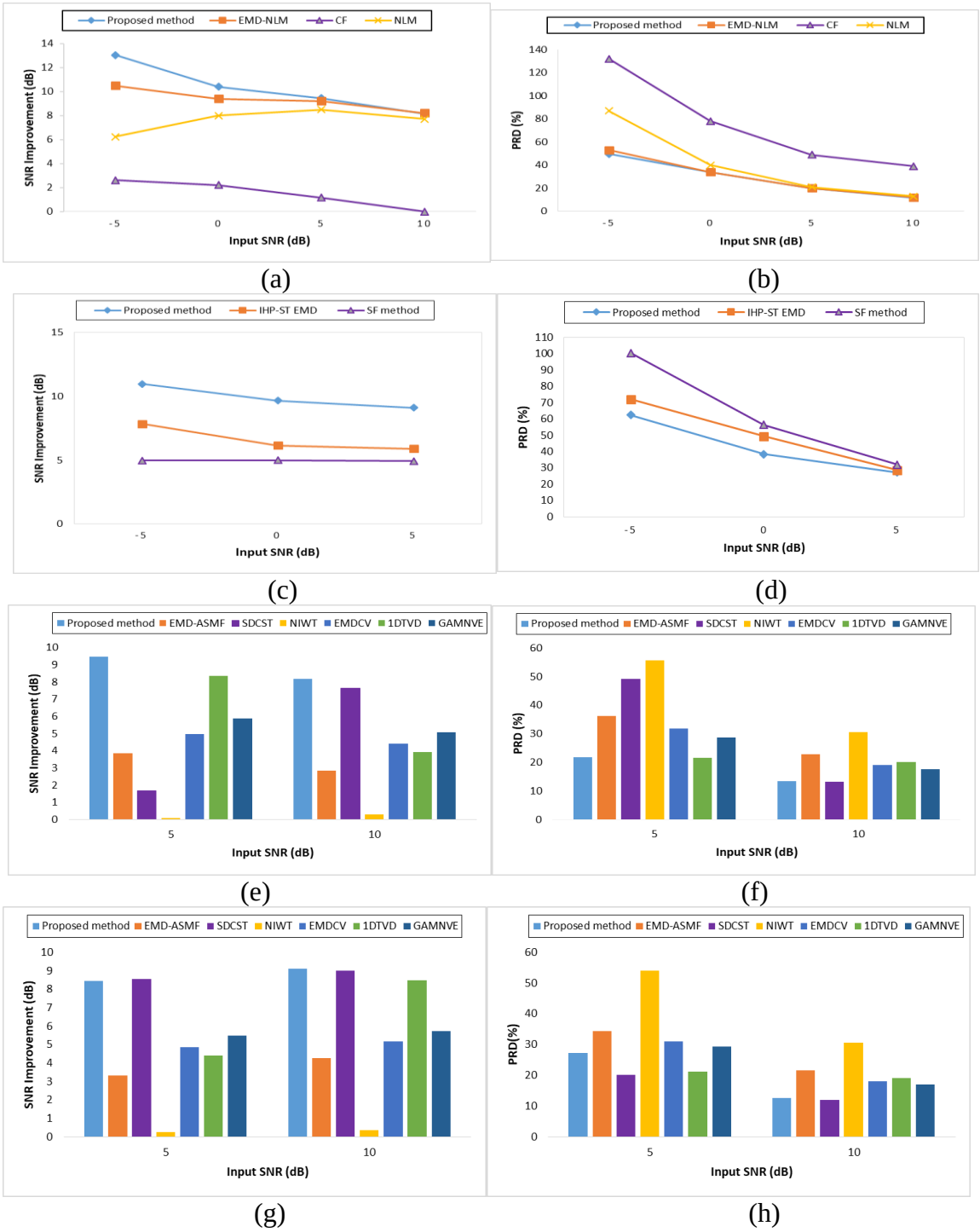


Figure IV.6: The improved performance of SNR and PRD for various denoising methods

IV.2.1.2 PLI removal

Additionally, PLI, the second kind of additive noise, was used to test the suggested method. Two fundamental frequencies—50 Hz and 60 Hz—of the produced ECG signal from the MIT-BIH database were supplemented with this noise. The average SNRoutput was determined by running the experiment on 16 distinct samples taken from this database.

An example of the proposed method's application is illustrated with record number 100 from the MIT-BIH database, as shown in Figure IV.7. This figure is segmented into three parts: IV.7(a) shows the original ECG signal, IV.7(b) displays the same signal with added noise, and IV.7(c) presents the signal after denoising. The visual comparison between the original and the denoised ECG signals highlights their strong similarity, underscoring the effectiveness of the denoising process.

Furthermore, with an initial SNR input of 10 dB at a noise frequency of 50 Hz, the denoising method achieved an output SNR of 22.69 dB. This corresponds to an SNR improvement of 12.69 dB, significantly enhancing the signal clarity and demonstrating the substantial efficacy of the proposed wavelet denoising technique.

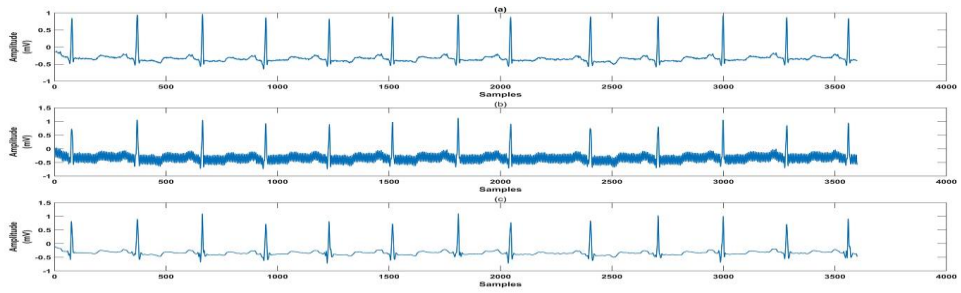


Figure IV.7: (a) Original ECG signal, (b) ECG signal corrupted with noise at SNRinput = 10 dB, (c) Denoised ECG signal obtained using the proposed technique (φ = db2, β = hard, λ = rigsure, L = 3, and ρ = mln)

In Table VI.3 and VI.4, we compare the SNRoutput achieved by the denoising method (PSO-WT) with other published noise removal techniques, namely EVD-based technique [152], MRLS-based technique [153], and EMD-WT-based technique [154] specifically for eliminating PLI noise. It is evident from the tables that the proposed method consistently outperforms the other techniques mentioned. Values highlighted in bold represent the optimal values for each SNR level and each ECG record. However, as indicated in Table 6, the MRLS approach exhibits superior performance at low noise levels for the 50 Hz frequency, yet the proposed method surpasses it at higher noise levels. Additionally, it is worth noting that the EMD-EWT-based technique [6] outperforms the proposed method in most cases at this frequency. Another noteworthy observation is that the proposed approach demonstrates outstanding results, outperforming all other state-of-the-art techniques for noise elimination at a frequency of 60 Hz, as demonstrated in Table

VI.4. Overall, these findings underscore the effectiveness of the proposed method compared to other contemporary methods for removing this type of noise.

Table VI.3: Comparative analysis of PLI removal (**f = 50Hz**) from different ECG signals at different SNRinput levels, evaluated based on SNRoutput as averaged values over 20 segments.

ECG Record	SNR_{inp} = -10dB					SNR_{inp} = -5dB					SNR_{inp} = 0dB				
	SNR_{out}(dB)														
	Proposed	EVD [152]	MRLS [153]	EMD-WT [154]	EMD-EWT [6]	**Proposed**	EVD [152]	MRLS [153]	EMD-WT [154]	EMD-EWT [6]	**Proposed**	EVD [152]	MRLS [153]	EMD-WT [154]	EMD-EWT [6]
100 m	14.065	3.758	13.666	11.366	**18.985**	16.322	7.284	17.899	11.869	**21.809**	16.198	11.683	21.583	11.547	**23.057**
102 m	13.626	3.770	13.560	13.958	**18.934**	14.913	7.462	17.651	14.926	**21.858**	15.582	10.526	21.161	15.716	**23.561**
103 m	13.455	3.770	13.984	13.804	**20.272**	14.580	7.300	18.472	15.313	**24.602**	17.055	11.707	22.815	16.294	**27.885**
105 m	**21.418**	3.772	14.054	19.238	20.378	22.887	7.302	18.625	21.846	**25.038**	23.586	11.711	23.116	24.422	**29.222**
109 m	**23.054**	3.773	14.095	20.012	20.424	24.889	7.305	18.590	23.420	**25.198**	25.771	7.420	23.023	25.503	**29.605**
116 m	17.638	3.775	14.122	15.267	**20.202**	18.221	7.307	18.547	17.759	**24.655**	18.450	11.718	22.719	18.515	**28.222**
119 m	**20.436**	3.774	14.071	17.066	20.362	21.718	7.305	18.481	19.252	**25.029**	22.530	11.716	22.797	21.013	**29.128**
123 m	**20.827**	3.769	14.056	13.270	20.249	21.884	7.114	18.635	15.344	**24.737**	22.279	10.867	23.092	16.156	**27.963**
201 m	18.289	3.770	13.789	16.956	**20.276**	19.046	7.299	18.268	19.434	**24.864**	19.314	11.706	22.497	20.428	**28.793**
205 m	16.033	3.779	13.691	12.754	**20.074**	16.246	7.312	18.068	13.260	**24.210**	17.255	11.723	22.117	14.811	**26.787**
213 m	16.597	3.772	14.146	18.008	**20.431**	17.135	7.303	18.601	21.485	**25.092**	17.372	4.681	22.911	23.389	**29.352**
219 m	19.923	3.768	14.069	17.622	**20.298**	20.754	7.626	18.500	19.643	**24.910**	21.165	11.885	22.800	21.540	**28.939**
220 m	14.574	3.775	13.955	11.075	**19.623**	15.419	7.308	18.357	11.919	**23.006**	17.281	11.721	22.396	11.216	**24.495**
221 m	16.244	3.770	13.971	16.442	**20.280**	16.634	7.301	18.463	18.355	**24.863**	16.779	11.711	22.798	19.619	**28.827**
223 m	**20.933**	3.767	14.048	18.023	20.383	22.002	7.296	18.513	19.867	**25.076**	22.278	11.702	22.862	21.894	**29.335**
231 m	10.470	3.767	13.946	11.604	**20.134**	12.986	7.295	18.409	13.221	**24.162**	16.542	11.405	22.619	13.154	**26.302**
AVG	17.349	3.770	13.951	15.404	**20.082**	18.477	7.320	18.380	17.307	**24.319**	19.340	10.868	22.582	18.451	**27.592**

Table VI.3: Comparative analysis of PLI removal (**f = 50Hz**) from different ECG signals at different SNRinput levels, evaluated based on SNRoutput as averaged values over 20 segments (Continue).

ECG Record	SNR_{inp} = 5dB					SNR_{inp} = 10dB				
	SNR_{out}(dB)									
	Proposed	EVD [152]	MRLS [153]	EMD-WT [154]	EMD-EWT [6]	**Proposed**	EVD [152]	MRLS [153]	EMD-WT [154]	EMD-EWT [6]
100 m	19.740	16.045	23.931	11.458	**23.700**	22.487	18.872	**25.648**	14.349	24.944
102 m	18.113	5.480	23.714	16.125	**25.164**	20.691	2.371	25.756	17.313	**27.353**
103 m	20.933	15.314	26.680	14.873	**29.042**	23.953	9.675	29.781	15.335	**30.179**
105 m	24.134	13.795	27.219	24.887	**32.356**	25.109	5.800	30.749	25.856	**34.112**
109 m	26.062	5.251	27.205	26.972	**33.232**	26.143	4.407	30.962	27.390	**35.536**
116 m	20.297	11.099	26.458	19.558	**30.065**	24.551	6.060	29.476	18.903	**30.385**
119 m	23.513	15.167	26.891	21.544	**31.859**	26.509	9.161	30.242	20.212	**32.610**
123 m	23.027	15.131	27.054	13.747	**28.451**	27.023	15.784	**29.406**	17.211	28.360
201 m	21.023	16.200	26.299	21.258	**31.390**	23.727	15.491	29.620	20.444	**32.479**
205 m	20.134	16.524	25.706	12.038	**26.655**	23.898	13.542	**28.065**	14.717	26.835
213 m	19.503	4.390	26.962	24.891	**32.706**	22.875	3.860	30.679	25.093	**34.745**
219 m	21.496	11.099	26.812	22.216	**31.759**	23.855	8.261	30.433	21.338	**32.787**
220 m	20.914	15.813	24.963	11.081	**23.440**	24.245	10.436	**25.868**	15.084	25.222
221 m	20.863	15.311	26.670	20.072	**31.415**	23.452	12.536	29.911	18.821	**32.473**
223 m	22.552	11.401	26.839	22.453	**32.448**	26.206	3.946	30.370	22.054	**33.760**
231 m	20.044	11.336	26.044	12.883	**25.333**	23.128	6.254	**27.780**	16.877	26.780
AVG	21.397	12.460	26.215	18.503	**29.314**	24.245	9.153	29.047	19.437	**30.535**

Table VI.4: Comparative analysis of PLI removal (**f = 60Hz**) from different ECG signals at different SNRinput levels, evaluated based on SNRoutput as averaged values over 20 segments.

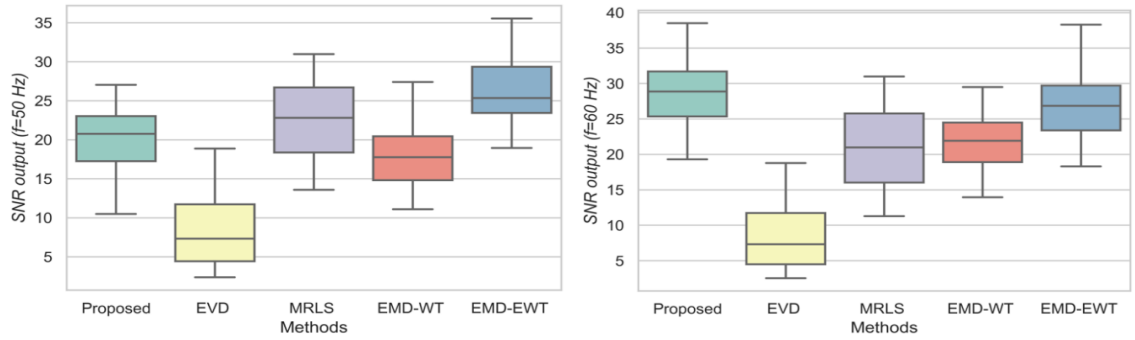
ECG Record	SNR_{inp} = -10dB					SNR_{inp} = -5dB					SNR_{inp} = 0dB				
	SNR_{out}(dB)														
	Proposed	EVD [152]	MRLS [153]	EMD-WT [154]	EMD-EWT [6]	**Proposed**	EVD [152]	MRLS [153]	EMD-WT [154]	EMD-EWT [6]	**Proposed**	EVD [152]	MRLS [153]	EMD-WT [154]	EMD-EWT [6]
100 m	**23.057**	3.754	11.310	13.932	18.682	**25.353**	7.251	15.866	14.924	22.260	**26.566**	11.582	20.184	16.220	24.476
102 m	**19.281**	3.750	11.269	15.456	18.283	20.313	7.420	15.752	16.373	**21.535**	20.750	10.436	19.892	17.553	**23.381**
103 m	**24.567**	3.761	11.321	16.383	19.097	**27.494**	7.304	15.992	19.819	23.426	**29.036**	11.727	20.633	20.540	26.839
105 m	**21.863**	3.761	11.432	21.702	19.310	**25.831**	7.276	16.179	24.234	23.860	**28.623**	11.650	20.962	25.481	27.729
109 m	**24.414**	3.766	11.429	22.358	19.424	**27.965**	7.292	16.209	25.485	24.141	**30.488**	8.450	21.043	27.256	28.446
116 m	**24.364**	3.766	11.482	18.295	19.411	**28.157**	7.294	16.302	20.732	24.161	**30.665**	11.697	21.234	21.918	28.522
119 m	**24.708**	3.771	11.467	20.128	19.487	**29.180**	7.302	16.296	22.138	24.349	**32.837**	11.712	21.235	24.462	28.995
123 m	**24.862**	3.771	11.372	16.818	19.444	**29.597**	7.117	16.110	18.570	24.208	**33.769**	10.870	20.961	20.582	28.583
201 m	**24.212**	3.764	11.369	19.663	19.126	**27.181**	7.285	16.012	21.069	23.329	**28.858**	11.663	20.607	23.495	26.555
205 m	**24.227**	3.771	11.399	16.870	19.402	**28.279**	7.301	16.112	18.047	24.128	**31.128**	11.710	20.928	19.106	28.246
213 m	**24.828**	3.770	11.445	21.348	19.520	**29.043**	7.300	16.264	23.809	24.467	**32.183**	4.678	21.226	27.507	29.369
219 m	**24.686**	3.770	11.436	20.393	19.486	**28.879**	7.632	16.254	22.095	24.320	**31.967**	11.891	21.193	24.485	28.915
220 m	**24.010**	3.768	11.373	14.297	19.180	**27.494**	7.298	16.058	15.656	23.584	**29.578**	11.705	20.703	17.526	27.225
221 m	**23.760**	3.765	11.347	19.177	19.087	**26.387**	7.280	15.991	20.644	23.200	**27.675**	11.644	20.518	22.693	26.279
223 m	**25.127**	3.769	11.444	20.709	19.498	**29.575**	7.299	16.251	22.598	24.387	**33.072**	11.706	21.164	24.998	29.166
231 m	**23.815**	3.772	11.419	14.741	19.286	**26.223**	7.304	16.174	17.290	23.920	27.414	11.421	21.023	19.209	**27.880**
AVG	**23.861**	3.765	11.395	18.267	19.233	**27.309**	7.310	16.114	20.218	23.705	**29.663**	10.909	20.844	22.064	27.538

Table VI.4: Comparative analysis of PLI removal (**f = 60Hz**) from different ECG signals at different SNRinput levels, evaluated based on SNRoutput as averaged values over 20 segments (Continue).

ECG Record	SNR_{inp} = 5dB					SNR_{inp} = 10dB				
	SNR_{out}(dB)									
	Proposed	EVD [152]	MRLS [153]	EMD-WT [154]	EMD-EWT [6]	**Proposed**	EVD [152]	MRLS [153]	EMD-WT [154]	EMD-EWT [6]
100 m	**27.113**	15.785	23.297	17.781	**25.407**	**27.477**	18.767	24.895	18.549	26.002
102 m	21.015	4.960	22.824	18.438	**24.788**	22.218	2.528	24.680	18.908	**26.245**
103 m	**29.689**	14.968	24.965	22.316	29.046	29.849	9.452	28.401	23.339	**29.703**
105 m	30.180	13.664	25.516	27.017	**30.379**	30.725	5.899	29.272	27.346	**31.730**
109 m	**31.761**	5.243	25.719	29.033	31.809	32.257	4.475	29.803	29.251	**33.823**
116 m	31.898	10.628	26.047	22.841	**31.996**	32.367	5.557	30.299	24.636	**34.193**
119 m	**35.157**	15.162	26.125	25.838	33.074	**36.255**	9.129	30.713	27.729	35.835
123 m	**36.793**	15.137	25.793	23.208	31.980	**38.502**	15.787	30.071	24.822	33.399
201 m	**29.574**	15.777	24.683	23.735	28.416	**29.807**	14.927	27.598	24.651	29.222
205 m	**32.686**	16.504	25.545	21.191	31.241	**33.818**	12.673	28.644	22.152	31.522
213 m	33.980	4.389	26.164	28.346	**34.088**	35.291	3.866	30.976	29.473	**38.299**
219 m	**33.658**	11.107	26.164	24.846	33.025	34.738	8.263	30.863	26.377	**35.884**
220 m	**30.517**	15.790	24.619	19.065	28.221	**31.084**	10.433	26.333	20.435	28.445
221 m	**28.205**	15.661	24.464	23.168	27.997	28.494	13.373	27.183	24.479	**28.715**
223 m	**35.146**	11.410	26.106	25.471	33.622	36.068	4.071	30.863	27.058	**37.238**
231 m	27.866	11.733	25.770	21.382	**29.300**	28.072	6.256	29.180	22.867	**30.194**
AVG	**30.952**	12.370	25.238	23.355	30.274	31.689	9.091	28.736	24.505	**31.903**

The comparative performance of denoising methods, as detailed in Tables VI.3 and VI.4, is visually represented in Figure IV.8 through box-plot diagrams. For a noise frequency of 50 Hz, shown in Figure IV.8(a), the Empirical Mode Decomposition-Extended Wavelet Transform (EMD-EWT) method outperforms others, achieving a maximum Signal-to-Noise Ratio (SNR_output) of 35 dB and an average of 26 dB. In contrast, the proposed method attains a satisfactory average SNR_output of 21 dB under the same conditions.

However, at a higher frequency of 60 Hz, as illustrated in Figure IV.8(b), the proposed method exhibits superior performance, achieving an average SNR_output of 28 dB, slightly higher than the 27 dB average for the EMD-EWT method. Notably, in this scenario, the majority of the results obtained with the proposed method exceed an SNR_output of 25 dB, demonstrating its robustness in higher frequency noise environments.



(a) (b)

Figure IV.8: PLI reduction comparison, (a) SNR_{output} (f = 50 Hz), (b) SNR_{output} (f = 60 Hz)

IV.3 ECG signal denoising using the proposed GA-WT

Given that the ECG signal has been contaminated by both PLI and WGN using equations (4.1) and (4.2) respectively, we utilised the GA technique to determine the optimal parameters (decomposition levels L and threshold value ϭ) for WT denoising to effectively eliminate the noise from the ECG signals. The resultant GA-WT noise reduction technique is depicted in Figure IV.9, demonstrating its application in enhancing the quality of ECG signals.

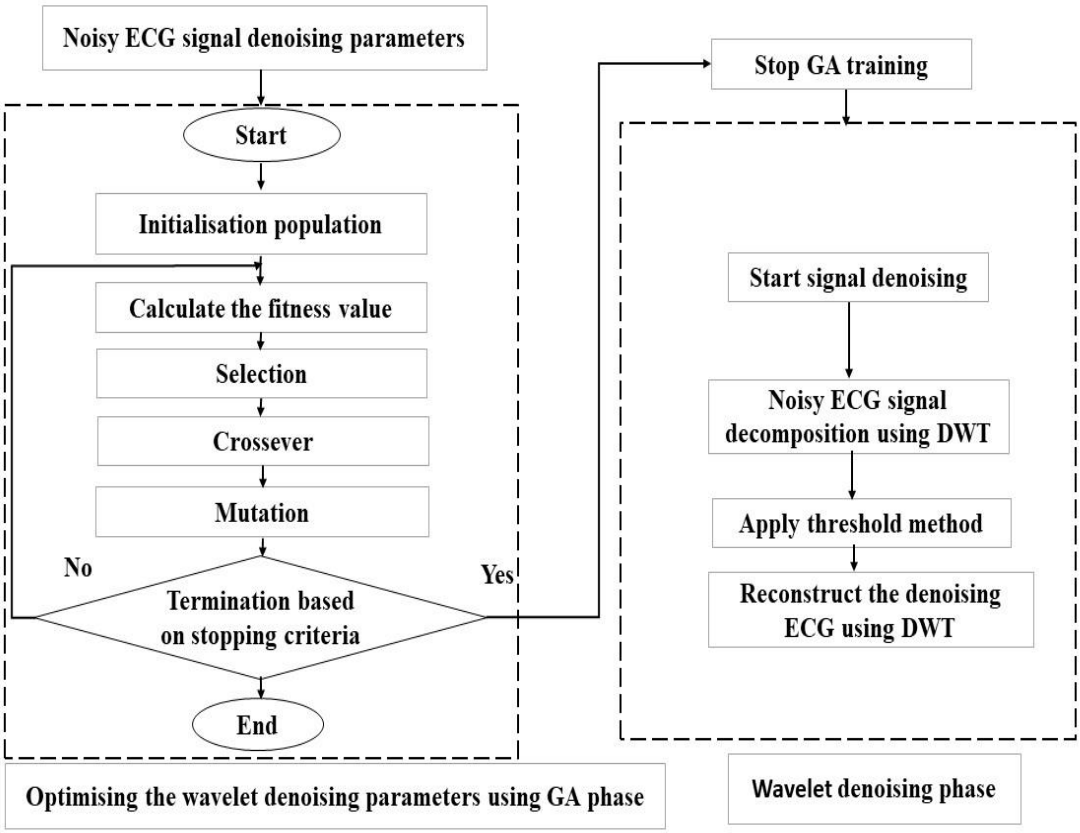


Figure IV.9: The proposed GA-WT method

The formulated GA-WT method for noise reduction can be characterised as follows:

Algorithm 4 Tuning WT Parameters Using GA Algorithms to obtain ECG Signal Noise-reduction

1: Initialise the noisy ECG signals (nECG) and estimate the SNR for the ECG signal input.

2: Initialise GA operators, initialise solution(s)

Xi (i = 1, 2) Xi (L, ϭ) represents the initial solution (where L and ϭ are the level of decomposition and threshold value, respectively).

3: X'opt = GA (X, Xi), X'opt (Lopt, ϭopt)

4: ECG Denoised = DWT (X'opt, nECG)

5: ECG Out Signals = Evaluation (ECG Denoised, SNRout, PRD)

The objective assessment of the proposed method is detailed in Table VI.5, which evaluates performance using two key metrics: SNR and PRD. This table presents a comparative analysis between the proposed approach, which integrates GA -enhanced DWT, and a standard ECG denoising technique that utilises the basic DWT alone. The comparison is conducted across a range of initial SNR levels to assess efficacy under varying noise conditions.

Table VI.5: The efficacy of the basic and optimised DWT in terms of SNRout and PRD

SNRinput (dB)	L -dwt	L-opt	Ɓ -dwt	Ɓ -opt	SNRout-dwt	SNRout-opt	PRD-dwt (%)	PRD-opt (%)
10	3	3	2.55	0.19	20.94	21.04	9	8.9
15		3		0.08	20.98	22.32	8.96	7.67
20		2		0.04	20.99	25.99	8.95	5.01
25		2		0.02	21	29.33	8.94	3.41

Both methods utilise the 'db13' mother wavelet function. The initial input SNR values, reflecting the introduced noise level in the clean ECG signal, are listed in the first column of Table VI.5. In each table, the second and third columns represent the initial and optimised values of the WT's decomposition level parameter, respectively. The fourth and fifth columns indicate the basic and optimised threshold values of the WT parameter. The remaining columns in each table present the SNR and PRD outputs for both the standard and improved GA-DWT methods.

The findings clearly indicate that the proposed GA-WT enhancement outperforms the basic DWT, as evidenced by higher SNR outputs and lower PRD ratios. Additionally, the table demonstrates that the output SNR and PRD ratios for the basic DWT remain relatively consistent regardless of the input SNR value. However, for the enhanced DWT, as the input SNR increases, the output SNR also increases while the PRD decreases. According to Table VI.5, which utilises the "db13" wavelet function, the output SNR value for the basic DWT ranges between 20.94 and 21 when the input SNR varied between 10 and 25 dB. Consequently, the SNR output remains consistently low, irrespective of the input SNR. Conversely, the optimised DWT method exhibits an increasing output SNR as the input SNR increases. For example, a 25 dB input SNR results in an output SNR of 29.33 dB. Therefore, the proposed method generates a higher SNR output compared to the basic DWT, especially for noisier ECG signals. The best input SNR value of 25 dB corresponds to a clearer ECG signal. In conclusion, the superiority of the proposed enhanced DWT method using GA over the basic WT for noise reduction from ECG signals is evident through the higher SNR output achieved.

Figure IV.10 presents the outcomes of an initial subjective assessment conducted at a frequency of 50 Hz. It exhibits the pristine original ECG signal (IV.10 (a)) alongside the ECG signal corrupted by additional noise (IV.10 (b)). Furthermore, it showcases the purified ECG signal (IV.10 (c)) generated through the recommended approach. This visual representation clearly indicates a high degree of resemblance between the original and

denoised ECG signals. This similarity underscores the effectiveness of the proposed technique for ECG noise elimination, which integrates DWT optimisation with GA.

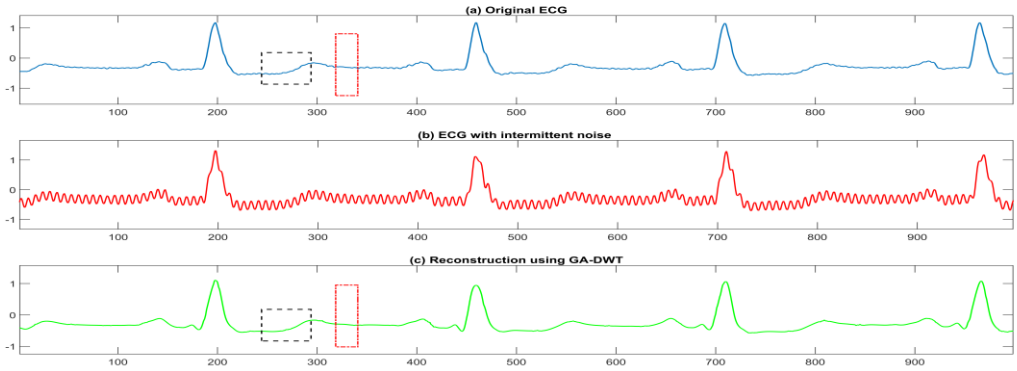


Figure IV.10: (a) Clean, (b) noisy and (c) denoised ECG signal using GA-WT at SNRinput=10dB

Table VI.6: Assessing SNR improvements and PRD across varied input SNR values for each ECG record with 50 Hz PLI.

ECG	SNR_{imp}					PRD				
Record	-10	-5	0	5	10	-10	-5	0	5	10
100	23.76	19.05	14.22	10.37	7.90	20.99	20.30	19.89	17.34	12.87
103	22.31	17.54	12.89	9.39	6.96	24.91	24.25	23.25	19.41	14.18
105	27.95	24.77	20.55	15.84	11.00	12.70	10.30	09.41	09.10	08.94
109	31.76	29.01	25.05	20.44	15.68	8.17	6.30	5.59	5.34	5.20
116	26.86	22.46	17.66	12.89	9.29	14.45	13.49	13.18	12.85	10.90
123	28.04	23.85	19.14	14.34	10.68	12.61	11.47	11.09	10.84	9.29
201	27.20	22.85	18.08	13.23	8.93	13.90	12.89	12.55	12.34	11.34
221	22.59	21.05	16.19	11.64	6.87	16.79	15.94	15.68	14.86	14.01
231	20.22	15.36	11.14	7.70	6.90	32.32	31.82	28.81	23.88	14.30

The enhanced SNR of the denoised PLI signal, as well as values for multiple ECG recordings with varying input SNR levels, are presented in Table VI.6. SNRimp values remain around 25 dB when the input SNR is minimal and decrease as SNR increases.

Table VI.7: Performance parameters for arrhythmia ECG records tainted by AWGN.

ECG	SNR_{imp}					PRD				
Record	-10	-5	0	5	10	-10	-5	0	5	10
100	16.22	11.59	7.78	6.58	5.58	52.57	54.47	42.08	26.62	16.73
103	12.28	8.53	7.48	5.83	5.86	115.41	78.02	44.10	28.61	16.31
105	12.12	10.35	9.19	7.96	6.99	95.64	55.22	34.88	22.69	14.40
109	14.52	12.22	10.94	9.06	8.31	71.15	43.16	28.66	19.93	12.16
116	15.29	10.41	8.52	7.49	6.07	64.24	63.19	37.37	23.88	15.79
123	18.96	14.44	9.63	7.80	6.73	36.37	35.85	34.13	22.96	14.65
201	12.92	9.98	8.42	7.61	5.95	103.78	60.10	38.35	23.68	15.80
221	12.23	10.01	8.13	7.12	5.69	92.70	60.13	39.75	25.05	16.56
231	11.38	8.13	6.73	5.98	5.67	133.63	83.02	48.76	28.46	16.74

The estimated PRD values for record 105 are 12.70, 10.30, 9.41, 9.10, and 8.94 at the specified levels of noise. Upon employing the proposed method for AWGN noise elimination, the corresponding improvement values are documented in Table VI.7. The

output signal and outcomes exhibit exceptional quality, irrespective of the magnitude of input noise.

In this section, we present the results obtained from applying the proposed approach for ECG signal noise removal. This method revolves around optimising the two primary parameters of the Discrete Wavelet Transform (DWT), namely the decomposition level (L) and the threshold value (σ), using Genetic Algorithms (GA). It's worth mentioning that this study was conducted using MATLAB 2018-B edition with the Wavelet Toolbox. Additionally, we conducted comparative analysis on filtering two different types of noise: Power Line Interference and additive Gaussian noise. Multiple records from the MIT-BIH database was utilised for the experiments outlined in this thesis.

IV.3.1 AWGN noise removal

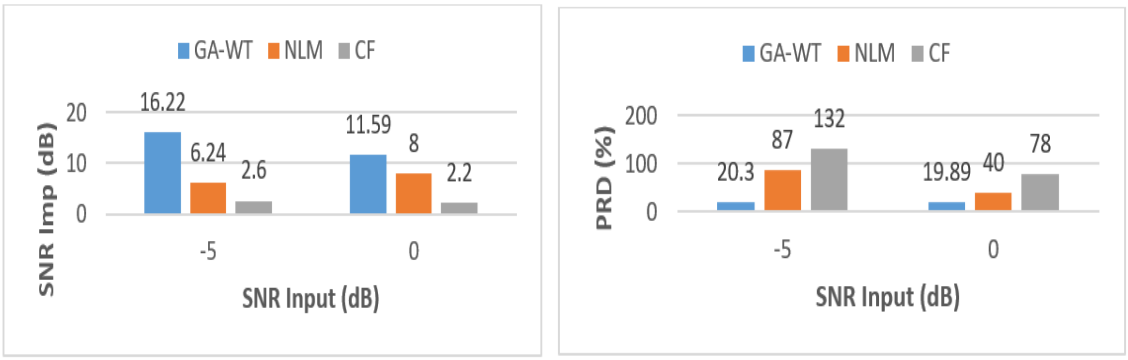
Table VI.8 showcases the effectiveness of the proposed approach in eliminating noise from ECG signals corrupted by AWGN. Utilising records 100, 101, 102, and 103 sourced from the MIT-BIH database, the table presents SNRout and PRD values at input noise levels of 5 dB and 10 dB. These values are compared with the outcomes of other methods including EMD-ASMF [147], GAMNVE[155] , PLI-SWT [156], and 1DTV [157].

The bolded values in the table denote the maximum values for each SNR record along with their corresponding PRD for individual ECG records. These findings underscore the effectiveness of the proposed method in eliminating such noise.

A further comparison was undertaken using records number 100 under high-noise SNR conditions of -5 and 0, as depicted in Figure IV.11. This comparison highlights the superiority of the proposed method over both NLM [144] and CF [143] methods, as indicated by achieving the highest SNR improvement and lowest PRD. This outcome serves to illustrate the effectiveness of the proposed approach.

Table VI.8: Performance metrics for arrhythmia ECG records corrupted by AWGN

Signal	SNR	Input SNR	Output						PRD					
			GA-WT	EMD- ASMF	GAMNVE	NIWT	PLI- SWT	1DTVD	**GA-WT**	EMD-ASMF	GAMNVE	NIWT	PLI- SWT	1DTVD
100	5		11.58	8.87	10.88	5.11	4.99	**13.34**	26.62	36.05	28.65	55.54	56.30	**21.59**
	10		**15.58**	12.78	15.09	10.13	9.99	13.93	**16.73**	22.98	17.65	31.18	31.67	20.11
101	5		**14.14**	9.66	10.94	5.15	4.99	13.25	**19.91**	32.92	28.47	55.32	56.31	21.78
	10		**16.48**	13.52	15.31	10.15	9.99	13.62	**15.00**	21.09	17.22	31.09	31.67	20.86
102	5		**11.38**	8.70	10.16	5.13	4.99	10.97	**27.00**	36.77	31.10	55.44	56.32	28.29
	10		**14.69**	12.50	14.40	10.14	9.99	11.15	**18.00**	23.72	19.08	31.14	31.68	27.71
103	5		10.83	9.24	10.71	5.10	4.99	**13.48**	28.61	34.55	29.24	55.59	56.30	**21.21**
	10		**15.86**	13.32	15.47	10.11	9.99	14.41	**16.31**	21.59	16.94	31.24	31.66	19.05



(a) (b)

Figure IV.11: The enhancement in SNR and PRD across different denoising methods.

IV.3.2 PLI noise removal

Tables VI.9 and VI.10 present the outcomes achieved by applying the proposed method to various records of the ECG signal from the aforementioned database. The first column enumerates the record numbers (100, 103, 105, 109, 116, 123, 201, 221, 231), while the subsequent columns display different methods used in previous studies for comparison with the proposed method at different SNR input values. The resulting SNR output of our denoising method (GA-WT) is juxtaposed with other state-of-the-art denoising methods in these tables, namely: the EVD-based technique [152], the MRLS-based technique [153], and the EMD-WT technique [158], all utilised for mitigating PLI noise. Table VI.8 showcases the superior performance of the proposed methodology when subjected to heightened noise levels, particularly with an SNR input of -10 dB at a frequency of 50 Hz. Notably, a significant enhancement in average SNR compared to the other techniques considered is observed in this scenario. Furthermore, it's important to note that the advantages of the proposed approach extend beyond these elevated noise levels, as it also demonstrates superior performance in certain recordings when noise levels are relatively lower.

Additionally, the suggested method outperformed earlier techniques when employed to reduce noise at a frequency of 60 Hz with input SNR values of 0 and 5, as demonstrated in Table VI.10. Overall, these results underscore the efficacy of the proposed noise reduction technique.

The comprehensive analysis presented in Tables VI.9 and VI.10 unequivocally demonstrates the highly effective noise reduction capabilities of the proposed approach in this context. These results emphasise its superiority over existing methods in certain records

and highlight its practical potential in real-world scenarios where noise reduction is paramount.

The dependable and consistent results across different noise levels and frequencies validate the reliability and credibility of the proposed technique, making it a promising path for continued research and practical application in relevant domains.

Table VI.9: The efficacy of removing PLI (at f = 50Hz) from different ECG signals with varied input SNR levels was assessed using averaged values over 20 segments.

ECG Record	SNR_{inp} = -10 dB				SNR_{inp} = -5 dB				SNR_{inp} = 0 dB				SNR_{inp} = 5 dB			
	SNR_{out}(dB)															
	GA-WT	EVD [152]	MRLS [153]	EMD-WT [154]	GA-WT	EVD [152]	MRLS [153]	EMD-WT [154]	GA-WT	EVD [152]	MRLS [153]	EMD-WT [154]	GA-WT	EVD [152]	MRLS [153]	EMD-WT [154]
100 m	**13,762**	3,758	13,666	11,366	14,051	7,284	**17,899**	11,869	14,227	11,683	**21,583**	11,547	15,371	16,045	**23,931**	11,458
103 m	12,312	3,770	**13,984**	13,804	12,542	7,300	**18,472**	15,313	12,892	11,707	**22,815**	16,294	14,392	15,314	**26,680**	14,873
105 m	17,954	3,772	14,054	**19,238**	19,777	7,302	18,625	**21,846**	20,558	11,711	23,116	**24,422**	20,848	13,795	**27,219**	24,887
109 m	**21,767**	3,773	14,095	20,012	**24,012**	7,305	18,590	23,420	25,059	7,420	23,023	**25,503**	25,447	5,251	**27,205**	26,972
116 m	**16,868**	3,775	14,122	15,267	17,468	7,307	**18,547**	17,759	17,669	11,718	**22,719**	18,515	17,893	11,099	**26,458**	19,558
123 m	**18,042**	3,769	14,056	13,270	**18,859**	7,114	18,635	15,344	19,147	10,867	**23,092**	16,156	19,349	15,131	**27,054**	13,747
201 m	**17,201**	3,770	13,789	16,956	17,856	7,299	18,268	**19,434**	18,086	11,706	**22,497**	20,428	18,238	16,200	**26,299**	21,258
221 m	12,597	3,770	13,971	**16,442**	16,052	7,301	**18,463**	18,355	16,193	11,711	**22,798**	19,619	16,647	15,311	**26,670**	20,072
231 m	10,221	3,767	**13,946**	11,604	10,364	7,295	**18,409**	13,221	11,142	11,405	**22,619**	13,154	12,705	11,336	**26,044**	12,883
AVG	**15,636**	3,769	13,965	15,329	16,776	7,279	**18,434**	17,396	17,219	11,103	**22,696**	18,404	17,877	13,276	**26,396**	18,412

Table VI.10: The efficacy of removing PLI (at f = 60Hz) from different ECG signals with varied input SNR levels was assessed using averaged values over 20 segments.

ECG Record	SNRinp = -10 dB				SNRinp = -5 dB				SNRinp = 0 dB				SNRinp = 5 dB			
	SNR_{out}(dB)															
	GA-WT	EVD [152]	MRLS [153]	EMD-WT [154]	GA-WT	EVD [152]	MRLS [153]	EMD-WT [154]	GA-WT	EVD [152]	MRLS [153]	EMD-WT [154]	GA-WT	EVD [152]	MRLS [153]	EMD-WT [154]
100 m	**14,714**	3,754	11,310	13,932	**18,761**	7,251	15,866	14,924	**22,628**	11,582	20,184	16,220	**25,295**	15,785	23,297	17,781
103 m	14,215	3,761	11,321	**16,383**	19,359	7,304	15,992	**19,819**	**22,987**	11,727	20,633	20,540	**26,657**	14,968	24,965	22,316
105 m	18,542	3,761	11,432	**21,702**	20,058	7,276	16,179	**24,234**	23,227	11,650	20,962	**25,481**	26,979	13,664	25,516	**27,017**
109 m	**22,413**	3,766	11,429	22,358	24,337	7,292	16,209	**25,485**	25,183	8,450	21,043	**27,256**	27,462	5,243	25,719	**29,033**
116 m	17,067	3,766	11,482	**18,295**	19,629	7,294	16,302	**20,732**	**24,258**	11,697	21,234	21,918	**27,971**	10,628	26,047	22,841
123 m	**18,308**	3,771	11,372	16,818	**19,54**	7,117	16,110	18,570	**24,629**	10,870	20,961	20,582	**28,647**	15,137	25,793	23,208
201 m	17,419	3,764	11,369	**19,663**	18,978	7,285	16,012	**21,069**	23,196	11,663	20,607	**23,495**	**26,359**	15,777	24,683	23,735
221 m	15,751	3,765	11,347	**19,177**	18,837	7,280	15,991	**20,644**	**22,827**	11,644	20,518	22,693	**25,643**	11,733	25,77	21,382
231 m	14,578	3,772	11,419	**14,741**	**18,449**	7,304	16,174	17,290	**21,925**	11,421	21,023	19,209	**23,397**	15,785	23,297	17,781
AVG	17,001	3,764	11,387	**18,119**	19,772	7,267	16,093	**20,307**	**23,429**	11,189	20,796	21,933	**26,490**	13,191	25,010	22,788

The findings presented in Table VI.10 clearly establish the superiority of the PSO-WT method over the GA-WT method in removing PLI at a frequency of 50Hz from diverse ECG signals across different input SNR values. Specifically, the PSO-WT method consistently produces higher SNR values and lower MSE, RMSE, and PRD values, indicating its capability to maintain the quality and authenticity of the original ECG signals while efficiently mitigating interference.

Table VI.11: Comparison of PSO-WT and GA-WT Methods for PLI removal in ECG signals across different metrics

ECG record	SNR Input	SNR Output		MSE		RMSE		PRD (%)	
		PSO-WT	GA-WT	PSO-WT	GA-WT	PSO-WT	GA-WT	PSO-WT	GA-WT
100 m	5	**19.74**	15.78	**0.0014**	0.0035	**0.0373**	0.0589	**10.33**	16.46
	10	**22.48**	18.32	**0.0009**	0.0019	**0.0292**	0.0439	**8.08**	12.20
102 m	5	**18.11**	15.06	**0.0018**	0.0023	**0.0428**	0.0487	**15.89**	17.91
	10	**20.69**	17.52	**0.0015**	0.0017	**0.0382**	0.0395	**14.17**	14.89
103 m	5	**20.93**	14.39	**0.0017**	0.0045	**0.0412**	0.0673	**10.58**	19.41
	10	**23.95**	16.96	**0.0007**	0.0024	**0.0259**	0.0495	**6.65**	14.18
105 m	5	**24.13**	20.84	**0.0009**	0.0014	**0.0308**	0.0377	**8.04**	14.18
	10	**25.11**	21.00	**0.0011**	0.0012	**0.0328**	0.0348	**8.58**	8.94
109 m	5	**31.76**	24.7	**0.0008**	0.0010	**0.0287**	0.0348	**5.18**	5.82
	10	**32.25**	25.3	**0.0006**	0.0009	**0.0254**	0.0300	**4.59**	5.43

IV.4 CNN-based ECG Signal Classification

This section provides a comprehensive explanation of the proposed methodology, including its foundational assumptions and detailed procedural steps. It specifically addresses the classification of ECG signals into three categories: Cardiac Arrhythmia (ARR), Congestive Heart Failure (CHF), and Normal Sinus Rhythm (NSR). This classification utilises a well-curated database, which will be described in detail, including the sources and features of the data. Furthermore, this section elucidates the techniques and analytical methods employed in conducting the experimental tests. The following outlines the deep learning-based methodology designed to achieve precise ECG signal classification

IV.4.1 Data Collection:

In this research we used data from three types of ECG signals to develop a robust deep Convolutional Neural Network (CNN). These types include ARR, CHF, NSR covering a range of heart conditions. Figure IV.12 shows these categories helping to emphasise the variety within the dataset.

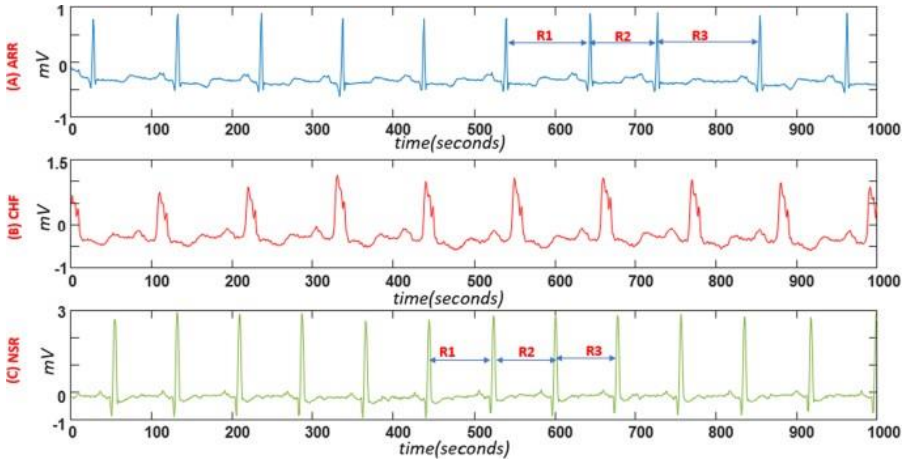


Figure IV.12: The three types of ECG signals: a) ARR, b) CHF, and c) NSR.

These signals were obtained from 162 ECG recordings sourced from three Physionet databases. These databases include the following:

- The MIT-BIH arrhythmia database comprises 96 recordings of ARR signals.
- The MIT-BIH normal sinus rhythm database consists of 30 records of NSR signals.
- The BIDMC congestive heart failure database encompasses 36 records of CHF signals.

IV.4.2 Data pre-processing

The dataset under consideration comprises a data matrix with dimensions 162 x 65536, representing 162 distinct ECG signals. Each signal is comprised of 65536 samples and comes with accurately assigned labels denoting their respective types. Specifically, the first 96 recordings correspond to ARR signals, recordings 97 to 126 represent CHF signals, and recordings 127 to 162 denote NSR signals. As shown in Table VI.12

Table VI.12: description of the collected data

No	Class	Signals
1	Cardiac Arrhythmia (ARR)	96
2	Congestive Heart Failure (CHF)	30
3	Normal Sinus Rhythm (NSR).	36
Total		162

Signal selection from the dataset

Analysing a dataset comprising signals with dimensions (162, 65536) initiates the selection of one segment consisting of 3136 samples, chosen for detailed scrutiny. This selected signal undergoes normalisation, ensuring uniformity across signals by scaling its values between -1 and 1 as shown in Figure IV.13

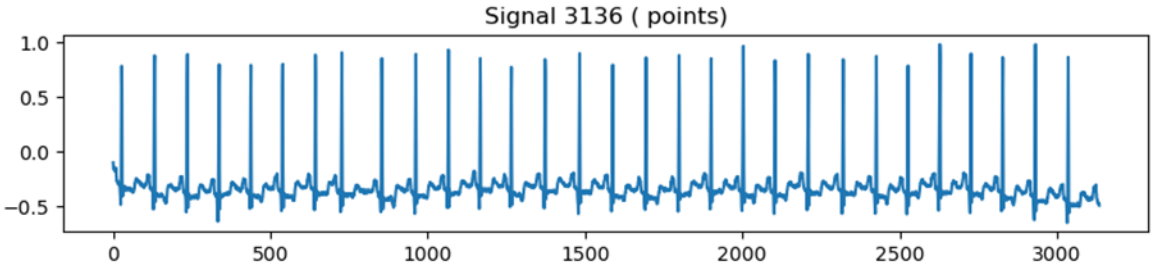


Figure IV.13: Signal segmentation.

Subsequently, the 1D signal undergoes transformation into a 2D matrix with dimensions of 56 × 56, as shown in Figure IV.14, which facilitates a systematic analysis.

This pivotal shift leverages the CNN's exceptional ability to recognise spatial patterns, significantly enhancing its capability to identify complex features within signals. The inherent proficiency of CNNs in handling spatial complexities is fundamental to the success of this approach. By converting 1D ECG signals into 2D spectral-temporal arrays, we align perfectly with CNNs' core strengths—this maintains the accuracy of temporal sequences while efficiently addressing the challenges presented by evolving signal analysis requirements. Furthermore, this transformation simplifies the feature extraction process and facilitates the use of advanced data augmentation techniques, which are crucial for improving the robustness of the model against variations in signal data. Consequently, this methodology not only boosts model flexibility and streamlines the training workflow but also significantly improves performance across complex analytical tasks. These enhancements are particularly valuable in high-stakes environments such as medical diagnostics, where precise and reliable signal interpretation is critical.

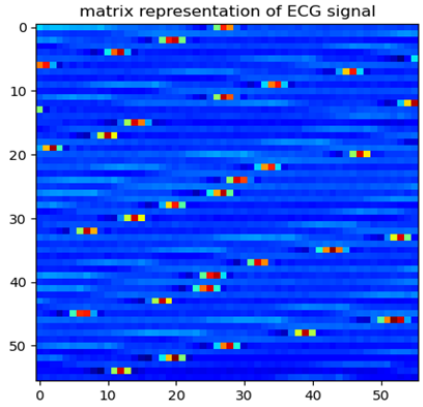


Figure IV.14: Signal Reshaping into 2D Matrix.

IV.4.3 The Two Dimensions Discrete Wavelet Transform (2D DWT)

The one-dimensional Discrete Wavelet Transform (1D DWT) can be implemented using the filter bank architecture, explained in section (II.6.2). However, for applications in image processing, a two-dimensional implementation of the wavelet transform is necessary. This two-dimensional version is often called the 'multidimensional WT in the literature [47,159,160]. Contemporary image code algorithms employ the separable dyadic 2D DWT, as exemplified by the JPEG2000 format [160]. By employing this method, the 1D DWT is expanded to encompass the columns and rows of an image individually.

A representation of an evaluation filter bank is illustrated in Figure IV.15, which illustrates a single-level Two-Dimensional Discrete Wavelet Transform (2D DWT). This configuration produces three sub-images (HL, LH, and HH). representing distinct directional orientations (Horizontal, Vertical, and Diagonal), along with a lower-resolution sub-image LL. The same filter bank structure can be applied iteratively to the LL channel to achieve a multilevel decomposition. The hierarchical representation of multilevel decomposition for an image is visualised in Figure IV.16.

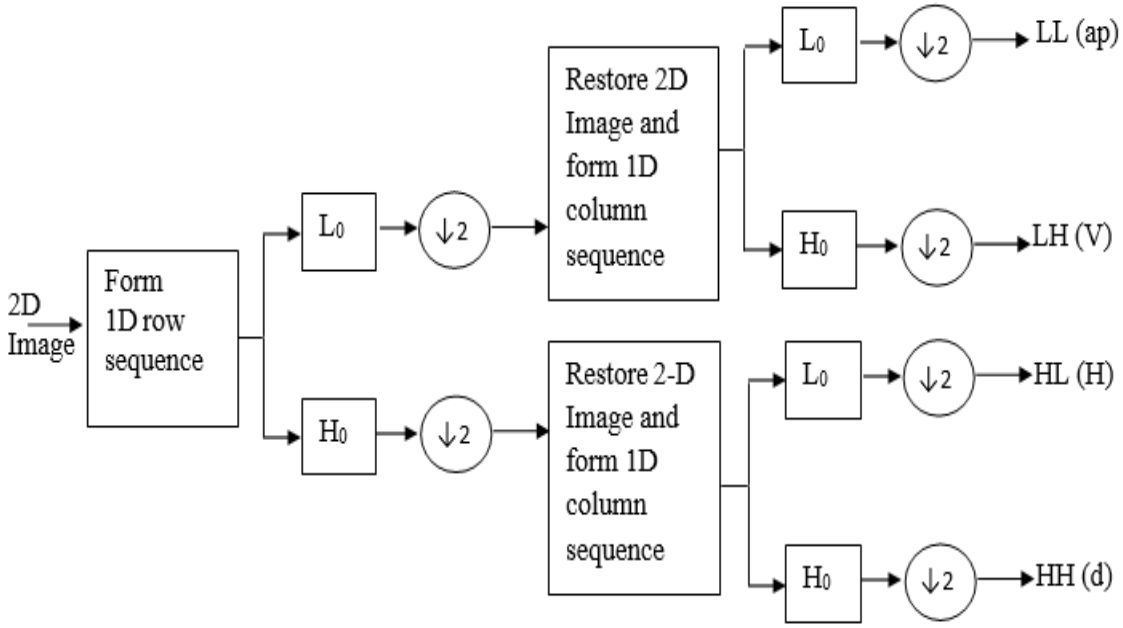


Figure IV.15: Single-level analysis filter bank for 2D DWT [53]

1, 2, 3: Decomposition Levels

H: Bands of High Frequency

L: Bands of Low Frequency

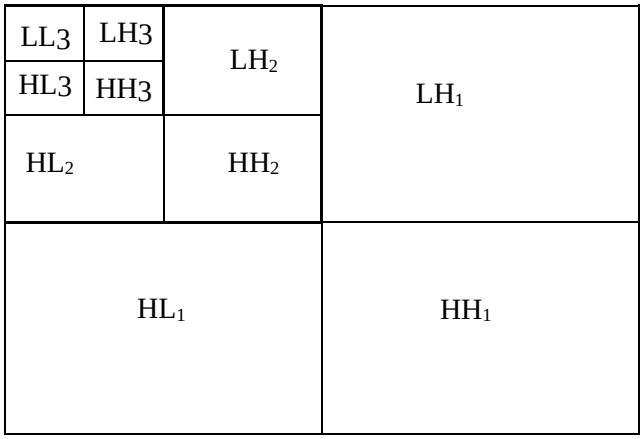


Figure IV.16: Three-level decomposition of 2D-DWT [55]

The parent image is subdivided into four progeny images, with each decomposition. The dimensions of each sub-image are proportional to one-fourth that of the parent image. The synthesised filter bank resembles the analysis filter bank in design, except it includes the production filters L1 and H1.

Alternately, the separated wavelets may be regarded as tensor results of scaling functions and 1D wavelets. Consider the one-dimensional wavelet denoted by φ(x), which is associated with the 1D scaled function φ. Then, the following definitions apply to three two-dimensional wavelets that correspond to three sub-images:

$$\begin{cases} \psi^V(x,y) = \varphi(x)\psi(y) \rightarrow LH \\ \psi^H(x,y) = \varphi(y)\psi(x) \rightarrow HL \\ \psi^D(x,y) = \psi(x)\psi(y) \rightarrow HH \end{cases} \quad (4.16)$$

The essential features at different resolution levels are highlighted using the 2D-DWT. Visualising the processed signal through 2D-DWT provides an overview of its characteristics at various scales and levels of detail. Finally, we obtained 4 images with dimensions of 28*28, as shown in Figure IV.17.

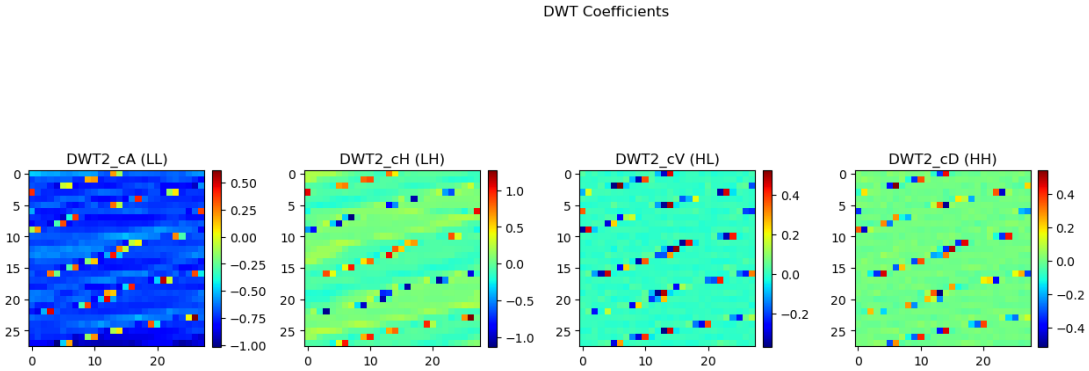


Figure IV.17: Treatment with 2D-DWT and visualisation of the results.

VI.4.3.1 Data segmentation

Data preprocessing initiates at the database level to tailor the dataset for our specific problem. Each ECG recording, comprising 65536 samples, undergoes further segmentation according to the following relation:

$$N=[(S-L)/H] +1 \quad (4.17)$$

Where:

N is the number total of segments

S represents the total number of samples (65536*162)

L denotes the length of each segment (3136)

H signifies Jump length (3136/4 = 784)

Figure VI.18 offers a detailed examination of the segmented output, providing an illustrative example of the signal segmentation process. This segmentation serves a dual purpose: augmenting the dataset's size and refining information accuracy. Thus, this procedure yields a total of 12960 images.

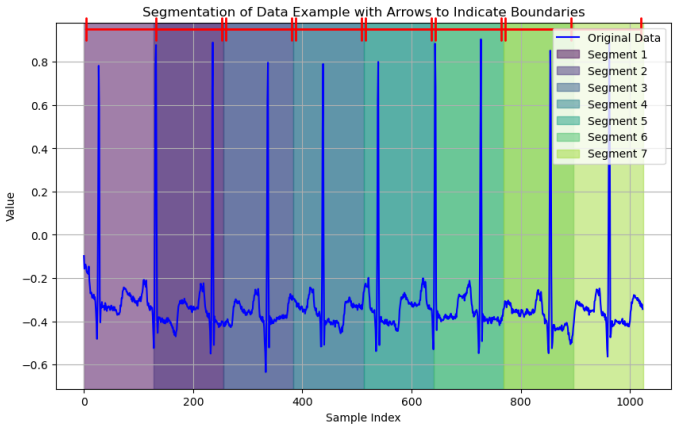


Figure: VI.18: Signal segmentation example

Table VI.13 and Figure VI.19 present the distribution of a cardiac image dataset categorised into three classes: Cardiac ARR with 7680 images, CHF with 2400 images, and NSR with 2880 images. The total number of images across all classes amounts to 12960.

Table VI.13: Images distribution

No	Class	Images
1	Cardiac Arrhythmia (ARR)	7680
2	Congestive Heart Failure (CHF)	2400
3	Normal Sinus Rhythm (NSR).	2880
Total		12960

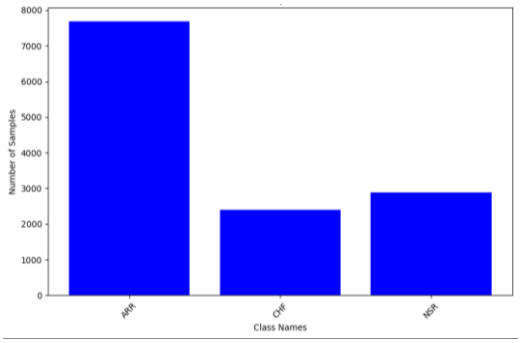


Figure: VI.19: Database distribution

VI.4.3.2 2D-DWT test on a single signal

Transforming a 1D signal into a 2D representation with the 2D-DWT involves wavelet packet decomposition. This process splits the signal into frequency and time domains, creating a 2D matrix. Each node in the resulting tree-like structure represents a specific frequency-time region of the signal, enabling detailed analysis across different time

intervals and frequencies. This 2D representation offers enhanced flexibility for feature extraction, denoising, and classification as shown in Figure VI.20.

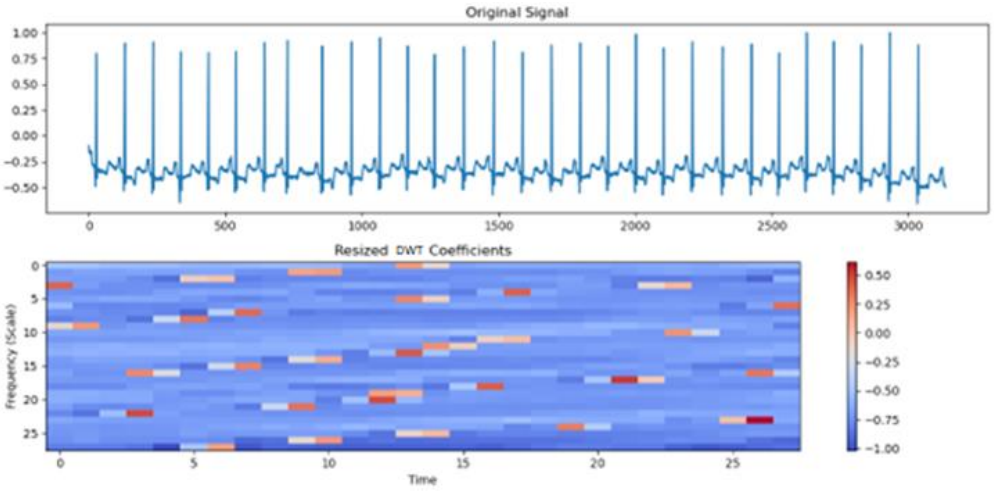
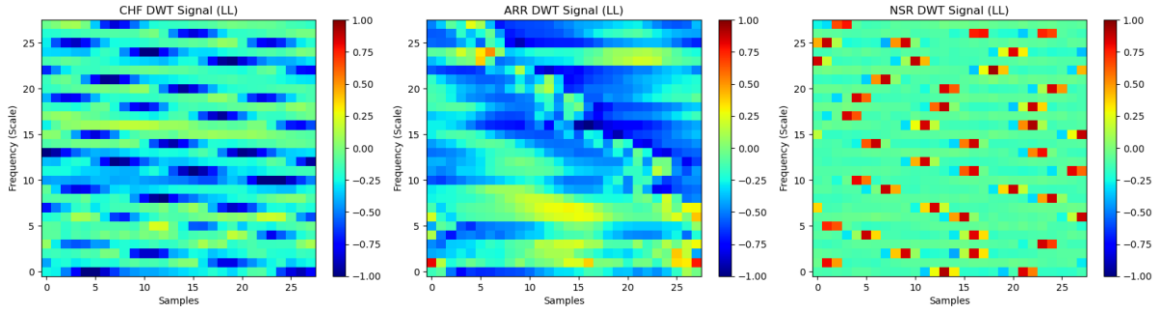


Figure: VI.20: 1D to 2D using 2D-DWT

VI.4.3.3 Display a sample image from CHF ARR NSR Class

The visualisation of heart signal data after a 2-DWT, as shown in Figure VI.21, offers a deepened understanding of the distinct patterns associated with CHF, ARR, and NSR. The 2-DWT process uncovers subtle, yet crucial time-frequency characteristics within the cardiac signals, revealing the specific nature of each condition. CHF patterns may display unique energy distributions related to heart dysfunction, while ARR patterns could highlight erratic behaviours indicative of arrhythmias. NSR signals, in contrast, typically show a regular and structured energy distribution, reflecting normal heart rhythm.

Each pattern's unique characteristics are critical for accurate diagnosis and understanding of the underlying cardiac condition. The 2-DWT not only facilitates this intricate visualisation but also enhances the diagnostic process by providing clear, interpretable data that correlate directly with physiological health states.



a- CHF b- ARR c- NSR

Figure: VI.21: CHF, ARR and NSR Class

The resulting images, with dimensions of 28x28x1, are used as inputs to the proposed 2D CNN classification model.

The new database is segregated into three distinct partitions: one earmarked for training, covering 80% of the data; the second designated for validation, accounting for 10% of the data; and the third reserved for testing, also comprising 10% of the data, as illustrated in Figure VI.22.

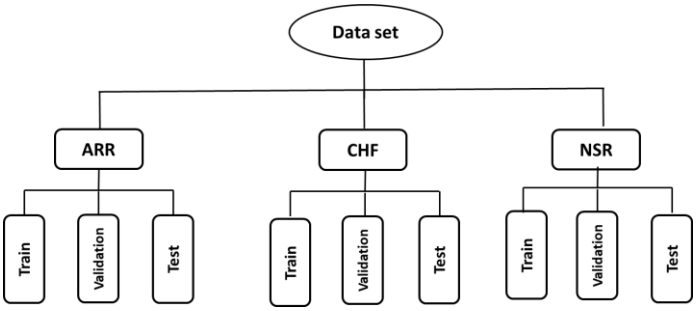


Figure VI.22: Basic data distribution.

IV.4.4 Proposed CNN architecture

The architecture of the proposed Convolutional Neural Network (CNN) model, as illustrated in Figure VI.23, is specifically designed to process input images of dimensions 28×28×1. This model comprises multiple layers that collectively focus on robust feature extraction and efficient classification. The network begins with an input layer that feeds into the first 2-D convolutional layer equipped with 32 filters of size 3×3, using ReLU activation to introduce non-linearity. Post-convolution, the network implements a batch normalisation layer to stabilise learning and speed up the training. This is followed by an average pooling layer with a 2×2 window to reduce spatial dimensions while retaining important features. Subsequent layers include two more convolutional layers, each followed by a ReLU activation function and batch normalisation, with the second and third convolutional layers having 16 filters each. After each convolutional layer, another average pooling step down-samples the feature maps, leading to a flattening layer that converts the 3D feature maps into a 1D array. This array feeds into a dense layer of 64 units with a ReLU activation to capture more complex relations within the data. To mitigate the risk of overfitting, a dropout layer with a rate of 0.2 is applied. Finally, a dense output layer with three units utilises a softmax activation function to achieve multi-class classification. The entire model is constructed sequentially, ensuring a smooth flow of tensors from input to output, and is designed to efficiently handle the classification task for ECG images.

The training of the proposed model is executed using predefined parameters and ECG images. During this training, the model assimilates features and refines its learnable parameters. Post-training, the model demonstrates proficiency in classifying heart abnormalities and stands ready to categorise ECG images into three distinct classes: NSR, ARR and CHF. The comprehensive analysis, including layer specifications and configurations, of the trained network for the proposed CNN model is meticulously presented in Table VI.14.

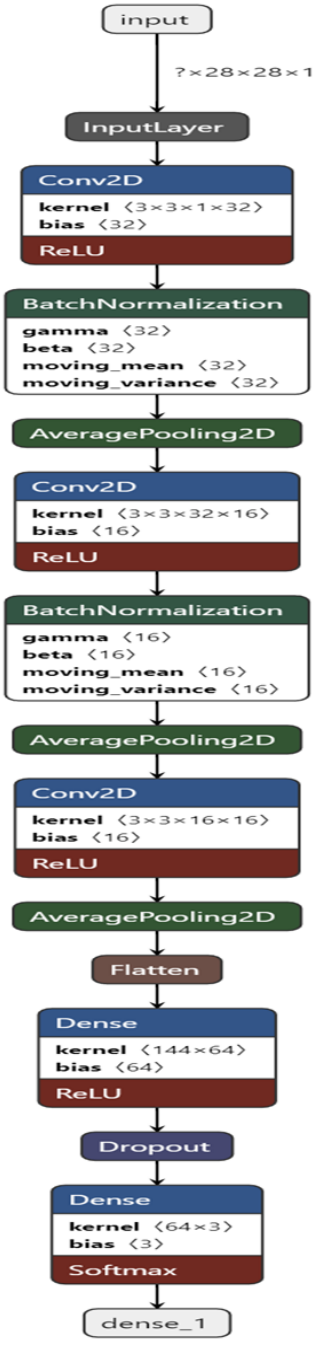


Figure VI.23: proposed 2D-CNN architecture

Table VI.14: Analysis of the Layers in the proposed CNN Model

Layer numbers	Type	Name	Properties	Input size	Output size
0	**Input**	Input layer	/	(28, 28, 1)	/
1	**Convolutional**	Conv2d	32 filters, 3x3 kernel, ReLU activation, Stride (1,1), Padding 'valid'	(28, 28, 1)	(26, 26, 32)
2	**Batch Normalization**	Batch_normalization	/	(26, 26, 32)	(26, 26, 32)
3	**Average Pooling**	Average_pooling2d	2x2 pool size, stride (2,2)	(26, 26, 32)	(13, 13, 32)
4	**Convolutional**	Conv2d_1	16 filters, 3x3 kernel, ReLU activation, stride (1,1), padding 'same'	(13, 13, 32)	(13, 13, 16)
5	**Batch Normalization**	Batch_normalization_1	/	(13, 13, 16)	(13, 13, 16)
6	**Average Pooling**	Average_pooling2d_1	2x2 pool size, stride (2,2)	(13, 13, 16)	(6, 6, 16)
7	**Convolutional**	Conv2d_2	16 filters, 3x3 kernel, ReLU activation, stride (1,1), padding 'same'	(6, 6, 16)	(6, 6, 16)
8	**Average Pooling**	Average_pooling2d_2	2x2 pool size, stride (2,2)	(6, 6, 16)	(3, 3, 16)
9	**Flatten**	Flatten	/	(3, 3, 16)	144
10	**Dense**	Dense	64 units, ReLU activation	144	64
11	**Dropout**	Dropout	0.2 dropout rate	64	64
12	**Output**	Dense_1	3 units, Softmax activation	64	3

IV.4.5 CNN model evaluation

A streamlined 2D Convolutional Neural Network (CNN) model, configured with a compact (28, 28,1) input size, has been strategically employed for optimal efficiency. Tailored for embedded system deployment, this lightweight model ensures rapid and precise predictions.

The architectural design is visually depicted in Figure VI.23, offering insight into the model's structure. The computational efficiency of a CNN is intrinsically tied to the number of parameters it encompasses, and the proposed model strikes a judicious balance between complexity and performance.

The dataset was randomly partitioned into training (80%), validation (10%), and test (10%) sets, ensuring a distribution of images across each category.as seen in Figure VI.24

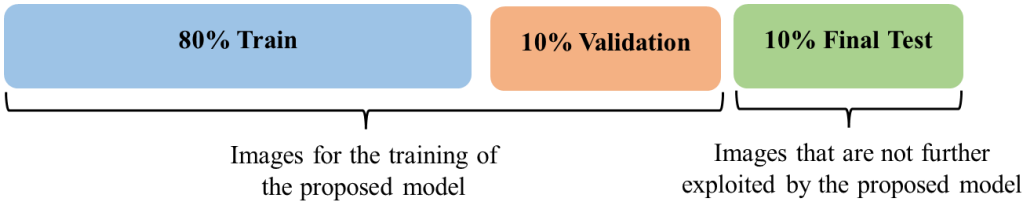


Figure VI.24: Dataset partitioning into training, validation and test

The CNN model was implemented on a standard laptop using Python programming language within the Jupyter Notebook environment. To ensure the robustness and generalisability of the model, we employed 5-fold cross-validation. Each fold of the dataset underwent training for 250 epochs to adequately converge to the optimal solution. The training was conducted using a batch size of 128 to balance computational efficiency with model performance. We utilised the Adam optimizer, renowned for its adaptive learning rate capabilities, set initially at 0.00007. This configuration helps in fine-tuning the model parameters effectively while avoiding local minima in the loss landscape.

Figure VI.25 visually encapsulates the training and validation accuracy, as well as the loss over epochs. Remarkably, there is a clear positive correlation between accuracy and the number of epochs, indicating enhanced performance with prolonged training. In contrast, the loss exhibits an inverse relationship, steadily diminishing as the epochs progress. These insights underscore the dynamic learning process of the model and validate its efficacy in discerning intricate patterns within the data.

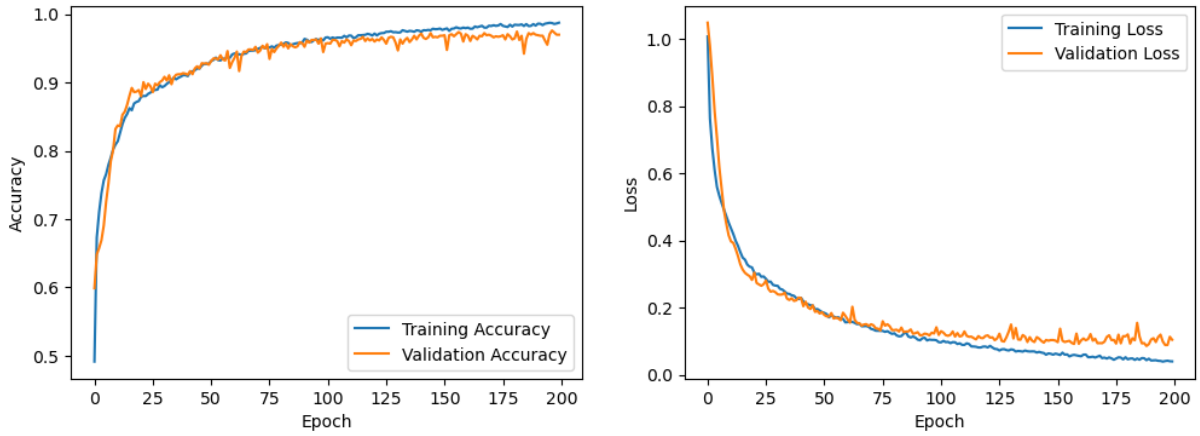


Figure VI.25: Accuracy and losses graphs.

The performance measurements of the experiments are calculated based on the following equations:

$$Accuracy = (TP+TN)/(TP+FP+FN+TN) \quad (4.18)$$

$$Recall = TP/(TP+FN) \quad (4.19)$$

$$Precision = TP/(TP+FP) \quad (4.20)$$

$$F1\ score = (2x\ Recall\ x\ Precision)/(Recall+Precision) \quad (4.21)$$

Table VI.15 provides a detailed breakdown of classification metrics across five different folds. It measures Accuracy, Loss, Precision, Recall, and F1-score for each fold.

Table VI.15: Performance measurement values obtained for each fold of the proposed model.

	Accuracy	**Loss**	**Precision**	**Recall**	**F1-score**
Fold-1	0.97377	0.07035	0.96853	0.9695	0.96901
Fold-2	0.96528	0.10085	0.9569	0.96432	0.96051
Fold-3	0.96952	0.08758	0.96178	0.96766	0.96461
Fold-4	0.97184	0.08428	0.96603	0.97104	0.9685
Fold-5	0.97453	0.07304	0.97445	0.96515	0.96963
Mean	0.970988	0.08322	0.965538	0.967534	0.9666452
Std	0.0037332	0.0122497	0.0066587	0.0028366	0.003858

The results indicate a high level of consistency in model performance, with Accuracy ranging from 96.528% to 97.737%, Precision from 96.853% to 97.445%, Recall from 96.432% to 97.104%, and F1-scores between 96.501% and 96.963%. The table also presents the mean and standard deviation for each metric, providing a summary of the overall performance. The mean values are 97.098% for Accuracy, 0.08322 for Loss, 96.553% for Precision, 96.753% for Recall, and 96.645% for the F1-score. The standard deviations are relatively low, indicating minor variations across folds, which suggests that the model's performance is stable.

IV.4.5.1 Model with Clean Signal

Table VI.16 presents a classification report for the clean signals that encapsulates the performance metrics of the proposed classification model. For the three classes under consideration (ARR, CHF, and NSR), the model demonstrates notable precision (0.99 for classes ARR and NSR; 0.98 for class CHF), indicative of its accuracy in correctly labelling positive instances. The recall metrics are equally impressive, with class ARR at 0.99, class CHF at 0.97, and class NSR achieving a perfect score of 1.00, highlighting the model's capability to identify all pertinent cases. The F1-scores, which synthesise precision and recall, maintain a consistently high level across all classes (0.99 for classes ARR and NSR, and 0.98 for class CHF).

Table VI.16: Classification report (clean signals)

	Precision	**Recall**	**F1-Score**	**Support**
ARR	0.99	0.99	0.99	7680
CHF	0.98	0.97	0.98	2400
NSR	0.99	1.00	0.99	2880
Accuracy			0.99	12960
Macro Avg	0.99	0.99	0.99	12960
Weighted Avg	0.99	0.99	0.99	12960

The 'support' figures denote the actual number of cases in the dataset for each class, amounting to 7680 for class ARR, 2400 for class CHF, and 2880 for class NSR. With an overall model accuracy of 0.99, the effectiveness of the model across all classes is evident. The macro and weighted averages, both standing at 0.99 for precision, recall, and F1-score, account for any class imbalance through the weighted metric, thus underscoring the model's consistent and robust performance across varied classes.

The provided confusion matrix in Figure VI.26 visually represents the performance of the proposed classification model on the clean signal, depicted as percentages. The matrix shows a high diagonal concentration of values, indicating accurate predictions. Specifically, the model correctly identified 99.10% of the ARR class, 96.96% of the CHF class, and 99.65% of the NSR class, with only minimal confusion between classes, as seen by the low off-diagonal percentages (0.52% and 0.38% for ARR, 2.96% and 0.08% for CHF, and 0.28% and 0.07% for NSR). These results affirm the model's exceptional capability to discriminate between the classes with high precision in a controlled, noise-free environment.

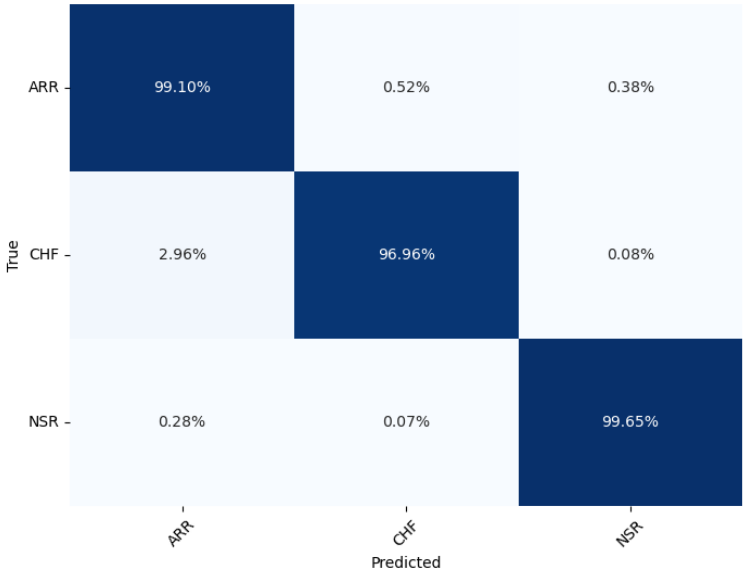


Figure VI.26: Confusion matrix for the clean signals

IV.4.5.2 Model with Noisy Signal

Table VI.17 presents a classification report for the noisy signals for the proposed model, providing key metrics that indicate the model's performance. The precision scores, which reflect the model's accuracy in predicting each class, are notably high (0.99 for classes ARR and NSR, and 0.98 for class CHF). Recall scores, indicating the model's ability to capture all relevant instances, are similarly high (0.99 for class ARR, a perfect 1.00 for class NSR, and slightly lower at 0.96 for class CHF). The F1-scores, which represent the harmonic mean of precision and recall, maintain this trend of excellence (0.99 for classes ARR and NSR, and 0.97 for class CHF), confirming the model's balanced precision and sensitivity.

Table VI.17: Classification report (Noisy signals)

	Precision	Recall	F1-Score	Support
ARR	0.99	0.99	0.99	7680
CHF	0.98	0.96	0.97	2400
NSR	0.99	1.00	0.99	2880
Accuracy			0.99	12960
Macro Avg	0.99	0.98	0.98	12960
Weighted Avg	0.99	0.99	0.99	12960

The support values show the number of true instances for each class within the dataset, highlighting the model's robustness given the sizeable number of instances evaluated. The overall model accuracy is reported at 0.99, underscoring its high level of correctness across all predictions. Both macro and weighted average scores across all classes are at 0.98 and 0.99, respectively, which account for class distribution and demonstrate the model's strong performance metrics across the board.

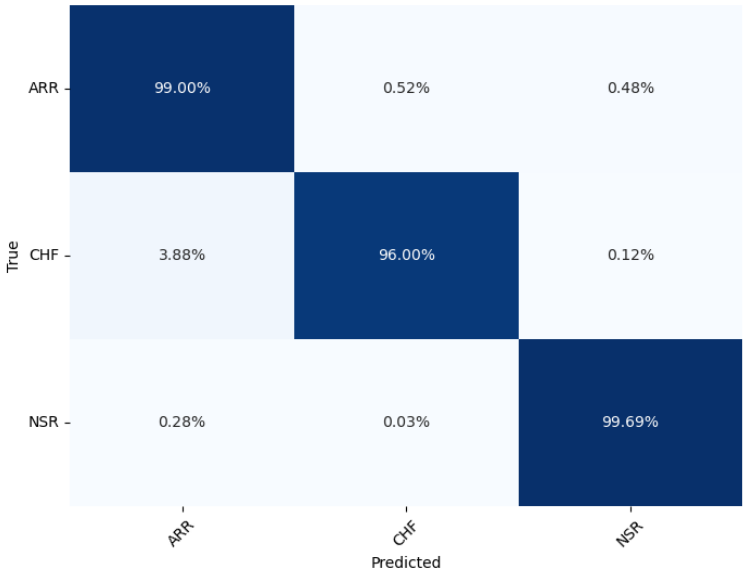


Figure VI.27: Confusion matrix for the noisy signals.

The confusion matrix in Figure VI.27 highlights the effectiveness of the proposed classification model when faced with AWGN noise. In this study, we included unfiltered signals using the proposed PSO-DWT method. However, a 2D-DWT-based approach directly processed these signals during the feature extraction phase. (It is worth noting that the filtering process is done in conjunction with the feature extraction process using 2D-DWT.) The matrix reveals that the model accurately identified 99.00% of ARR cases and 96.00% of CHF cases, along with 99.69% of NSR cases, displaying its high accuracy in

distinguishing between true class labels amid low 2D-DWT noise during the feature extraction phase. Minimal misclassification, as indicated by low off-diagonal values, indicates that introducing noise and bypassing PSO-DWT filtering had little effect on the model's ability to discriminate between classes. This confirms the strong performance of the model in low-noise environments, maintaining high accuracy for the ARR and NSR classifications and only a slight decrease in accuracy for the CHF class, even without PSO-DWT filtering. This result confirms the power and effectiveness of the model in accurately classifying conditions.

IV.4.5.3 Model with Denoised Signal

Table VI.18 delineates the classification report for the denoised signal using the proposed model. The report details the precision, recall, and F1-score for three distinct classes (ARR, CHF, and NSR), alongside the support, which is the actual count of instances per class. Class ARR exhibits a precision of 0.93 and recall of 0.98, resulting in an F1-score of 0.96. Class CHF shows slightly higher precision at 0.95 but a lower recall of 0.93, with an F1-score of 0.94. Class NSR maintains the highest precision of 0.97 but a notably lower recall of 0.86, culminating in an F1-score of 0.91. The overall accuracy of the model stands at 0.94, indicating a high level of correctness across all classifications. The macro average, which calculates the unweighted mean of precision, recall, and F1-score, is 0.95, 0.92, and 0.94, respectively. The weighted average, which considers the support, aligns with the macro averages, suggesting the model performs consistently well across classes of varying sizes. This robust performance, particularly in a denoised environment, underscores the model's effectiveness in signal classification.

Table VI.18: Classification report (denoised signal)

	Precision	**Recall**	**F1-Score**	**Support**
ARR	0.93	0.98	0.96	7680
CHF	0.95	0.93	0.94	2400
NSR	0.97	0.86	0.91	2880
Accuracy			0.94	12960
Macro Avg	0.95	0.92	0.94	12960
Weighted Avg	0.95	0.94	0.94	12960

Figure VI.28 presents the confusion matrix for the proposed classification model applied to a PSO-DWT-denoised dataset, displayed in percentages. This matrix evaluates the model's performance in correctly predicting the classes ARR, CHF, and NSR. For ARR, the model has an impressive true positive rate of 98.05%, with minimal confusion with other classes.

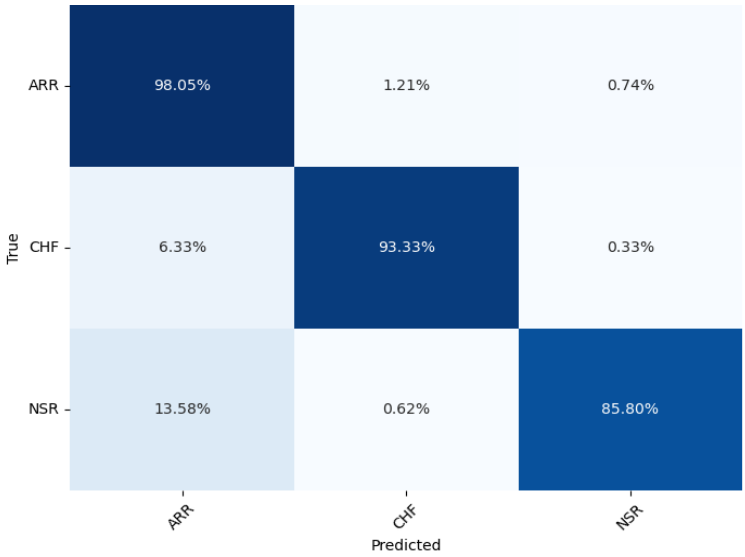


Figure VI.28: Confusion matrix for the denoised signal

CHF predictions are accurate at 93.33%, albeit with a higher misclassification rate with ARR and NSR. Notably, the model shows a considerable rate of misclassification for NSR, with only 85.80% correctly identified and a significant 13.58% misidentified as ARR. These percentages demonstrate the model's strong ability to accurately classify ARR and CHF in a denoised setting, while indicating a need for improvement in the classification of NSR, possibly due to similarities in denoised characteristics between NSR and ARR signals within the dataset.

VI.4.5.4 Result and discussion

In the evaluation of the proposed classification model designed to identify three distinct conditions ARR, CHF, and NSR, three datasets were analysed through confusion matrices: a clean set, a set with added AWGN noise, and a set that underwent a PSO-DWT-denoising process. In the clean set, the system exhibited high classification accuracy, with ARR, CHF, and NSR correctly identified 99.10%, 96.96%, and 99.65% of the time, respectively, indicating a strong baseline performance. Upon the introduction of AWGN noise, the system, leveraging a feature extraction process that utilises the 2D-DWT,

maintained high accuracy rates (99.00% for ARR, 96.00% for CHF, and 99.69% for NSR), demonstrating the model's robustness against noise interference.

However, the application of PSO-DWT-denoising led to a marked decrease in the model's accuracy, most notably in the NSR condition, which saw a decline to 85.80%. This dual-stage denoising, first on the 1D signal and subsequently on the 2D matrix during feature extraction resulted in significant information loss, particularly affecting the NSR classification. The PSO-WT method, while effective in noise reduction for ARR and CHF, exhibited limitations for the NSR class, suggesting a necessity for model refinement in the feature extraction and denoising techniques to improve NSR detection. The overall findings indicate a robust classification system for ARR and CHF even in noisy conditions but highlight a critical area for improvement in NSR classification, which is essential for ensuring reliability in medical diagnostic applications.

VI.5 Conclusion

This chapter underscores the substantial progress achieved through the integration of optimisation algorithms specifically PSO with WT and GA with WT in mitigating noise in ECG signals, particularly from PLI and WGN. These methodologies significantly enhance signal clarity and surpass existing state-of-the-art denoising techniques. The empirical evidence provided vividly demonstrates the practical effectiveness of both PSO-WT and GA-WT, marking a major advancement in refining ECG signal processing to improve the accuracy of medical diagnoses and analyses.

Furthermore, when these denoising techniques are incorporated as preprocessing steps within the proposed CNN model for classifying ECG signals, their utility is considerably magnified. This integration not only streamlines the overall classification process but also ensures a more accurate and precise solution to identifying and categorizing cardiac anomalies. This dual approach of noise reduction and enhanced classification establishes a robust framework for future developments in cardiac health monitoring and diagnostic technologies.

Chapter V

Design and Implementation of an IoT-based ECG Signal Monitoring System

V.1 Introduction

In the changing world of healthcare, incorporating IoT technologies represents a step forward in improving real time health monitoring, particularly in the area of cardiac health. This research utilises the ESP32 microcontroller along with AD8232 ECG sensor technology to develop an IoT-based system for monitoring ECG signals. This groundbreaking system enables the remote transmission of vital cardiac data to healthcare professionals effectively, addressing key gaps in patient care by leveraging the widespread connectivity of the Internet. In this chapter, we delve into the steps required to put together programme and launch the suggested IoT solution. Important tasks involve setting up the ESP32 microcontroller, incorporating the AD8232 sensor, and using Node RED, a visual programming environment that simplifies the creation of complex IoT workflows. By implementing this system, healthcare providers can keep track of patient's heart health instantly, ensuring timely interventions and enhanced patient monitoring.

V.2 Proposed approach for ECG signal monitoring

Figure V.1, illustrates the streamlined workflow of the proposed automated ECG diagnostic system.

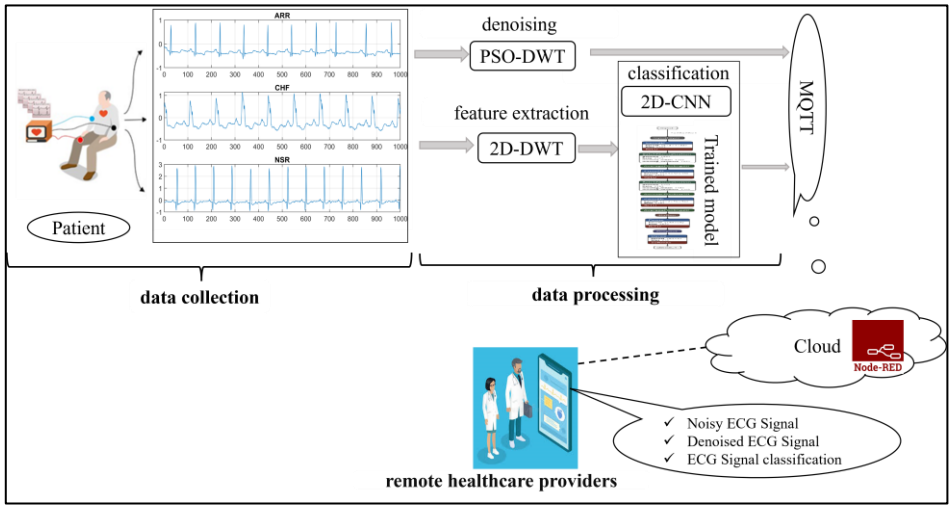


Figure V.1: Architecture of the proposed approach for ECG signal monitoring

Initially, ECG data is meticulously gathered from a patient and subsequently undergoes a rigorous processing phase, where noise is significantly reduced to enhance signal clarity. The refinement continues with the implementation of a 2D DWT, a proposed technique employed to meticulously extract defining features from the ECG signals.

These critical features are then input into a 2D convolutional neural network, which has been expertly trained to accurately identify and classify the ECG patterns into one of three critical categories: arrhythmia, normal sinus rhythm, or congestive heart failure. The culmination of this process is the secure transmission of diagnostic results to the cloud, ensuring immediate accessibility for healthcare providers and fostering prompt and informed medical decision-making.

V.3 Experimental circuit

In the development of the proposed health monitoring system, as depicted in Figure V.2, we employed an ESP32 microcontroller paired with an AD8232 heart rate sensor. This setup is designed to capture the heart's electrical activity through electrodes strategically placed on the trunk and limbs. The AD8232 is pivotal in this system; it acts to amplify the delicate cardiac signals to a level suitable for digital processing. The ESP32 microcontroller subsequently processes these signals, facilitating their analysis. This configuration not only allows for the precise monitoring of the electrical activities of the heart but also supports continuous analysis of cardiac functions. Such capabilities are indispensable for IoT-based healthcare applications, enabling them to deliver real-time insights into patient care. This system's continuous monitoring feature is particularly crucial in managing chronic conditions such as arrhythmia and heart failure, where timely data can significantly influence the effectiveness of the interventions deployed.

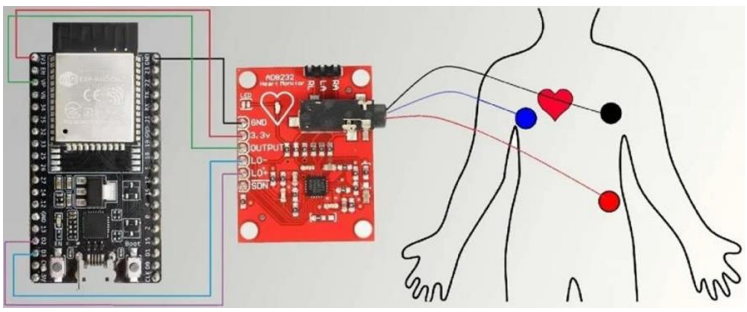


Figure V.2: Experimental Circuit for ECG Signal Collection

V.3.1 Essential components:

V.3.1.1 The ESP32-S3:

The ESP32-S3 development board is characterised as follows:

- **Equipped with ESP32-S3 SoC:** Designed for Wi-Fi and Bluetooth applications.
- **ADC (Analogue-to-Digital Converter):** converts analogue signals to digital values for processing.
- **Processor:** Dual-core XTensa LX7 microprocessor, capable of running up to 240 MHz
- **Memory:** Comes with 512 KB of internal SRAM.
- **I/O Peripherals Support:** Includes SPI, I2S, I2C, PWM, RMT, ADC, UART, SD/MMC host, and TWAI™ for versatile hardware interfacing.
- **GPIOs:** Features 45 programmable GPIOs.
- **Storage:** Includes an 8 MB flash memory and supports larger, high-speed octal SPI flash and PSRAM.
- **Cache:** Configurable data and instruction cache.
- **AI Acceleration Support:** Offers AI acceleration for neural network computing and signal processing, accessible through ESP-DSP and ESP-NN libraries.

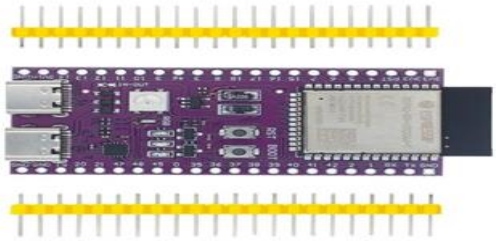


Figure V.3: The ESP32-S3

For wireless connectivity, the ESP32-S3 supports 2.4 GHz Wi-Fi (802.11 b/g/n) and Bluetooth 5 (LE), which includes long-range support through Coded PHY and advertisement extension. It also supports higher transmission speeds and data throughput with a 2 Mbps PHY.

Security features are robust on the ESP32-S3, providing AES-XTS-based flash encryption, RSA-based secure boot, digital signature, HMAC, and a “World Controller” peripheral that enables isolated execution environments for trusted computing.

The ESP32-S3 is supported by the ESP-IDF platform, which provides a mature software environment for application development, including rigorous testing and regular updates.

V.3.1.2 The AD8232 sensor:

The AD8232 is an integrated signal conditioning block for ECG and other biopotential measurement applications. It is designed to extract, amplify, and filter small biopotential signals in the presence of noisy conditions. Here are some of its key technical characteristics:

The AD8232 is configured for a single lead heart rate monitoring, making it an ideal choice for portable ECG applications.



Figure V.4: The AD8232 sensor

V.3.1.3 Jumper Wires and Breadboard: For making connections between the ESP32 and the AD8232 sensor.

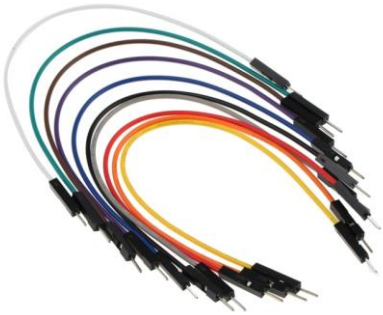


Figure V.5: Figure Jumper Wires

V.3.1.4 Connections:

- The OUTPUT pin of the AD8232 is linked to an analog input on the ESP32, facilitating the capture of ECG signals.
- Ground and power (3.3V) connections are also established between the ESP32 and the AD8232.

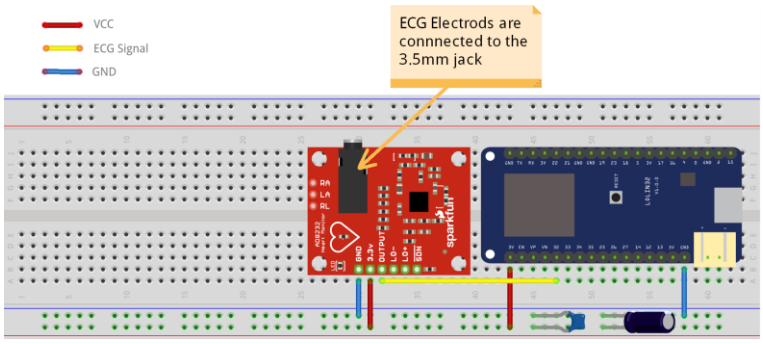
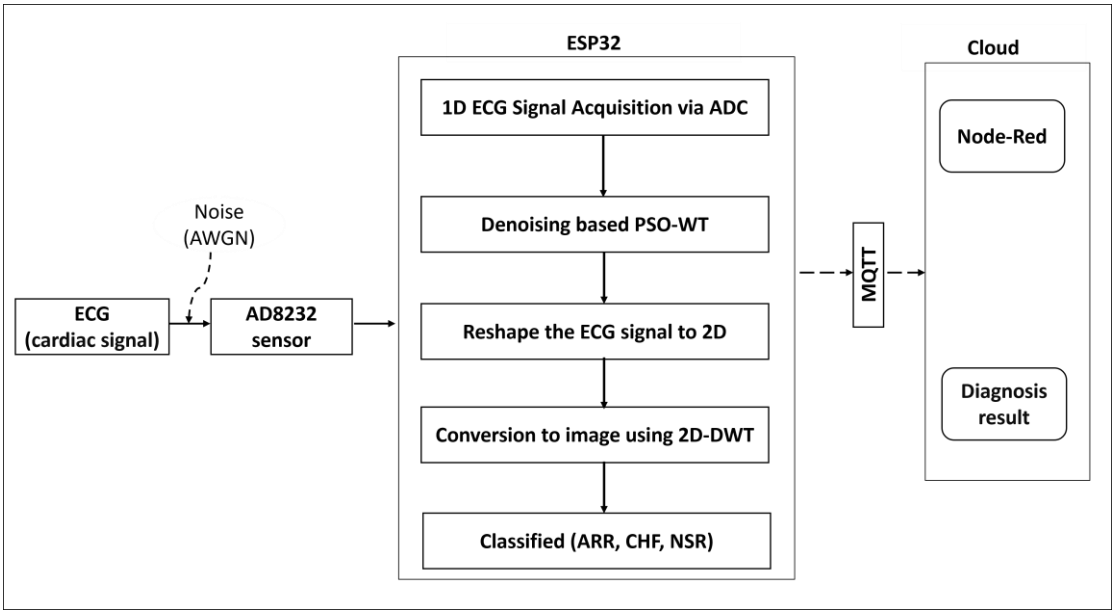


Figure V.6: IoT ECG Monitoring Breadboard

Figure V.6 showcases a breadboard setup for ECG data collection using an ESP32 microcontroller. Color-coded wires organise the circuit: red for power (VCC), yellow for the ECG signal, and blue for ground (GND). The ECG sensor with a 3.5mm jack for electrodes is on the left, while the ESP32 on the right processes the signals. This setup is crucial for developing health monitoring prototypes.

FigureV.7 illustrates the proposed Block Diagram, a sophisticated healthcare optimisation system that skilfully marries IoT's detailed data capture with AI's leading-edge analytics. Using the AD8232 sensor, the system adeptly collects cardiac signals, which commonly include AWGN noise. The AI component employs PSO-WT for effective signal enhancement, stripping away noise and improving clarity. The denoised signal is then transformed into a two-dimensional representation through 2D-DWT, facilitating the precise extraction of vital features and the detection of irregularities via a finely-tuned 2D-CNN model.



FigureV.7: Block diagram of the healthcare improvement system based on IoT and AI

These processes are proficiently executed on an ESP32 board, which ensures optimal efficiency due to its powerful processing capabilities and low power consumption. Subsequently, the MQTT (Message Queuing Telemetry Transport) protocol takes over, providing a secure and reliable means for transmitting the data to the cloud. This protocol is especially valued for its lightweight nature and effective data flow management in IoT applications. Once in the cloud, the data is managed and analyzed by Node-RED, a flexible, flow-based programming tool that facilitates the easy construction of data processing workflows. Node-RED parses the incoming data streams to extract meaningful patterns and trends, which are essential for generating in-depth, actionable diagnostic insights.

Designed to enhance rapid response capabilities and prioritize personalized patient care, this system significantly improves the speed and accuracy of decision-making in healthcare settings. By integrating these cutting-edge technologies, the system not only streamlines the diagnostic process but also ensures that patient data is handled securely and efficiently, ultimately supporting advanced health monitoring solutions.

V.3.2 Software Implementation:

V.3.2.1 Programming the ESP32:

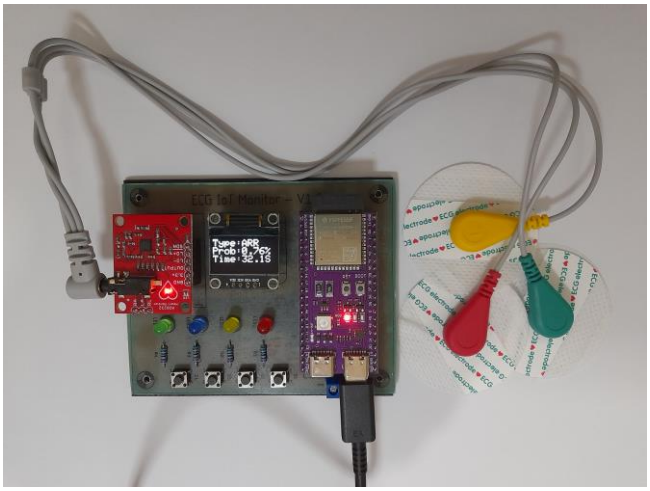
- Utilise the Arduino IDE, configuring it to support the ESP32.
- Develop a sketch to read the ECG signals from the AD8232, leveraging the analog-to-digital converter (ADC) of the ESP32.
- Integrate Wi-Fi and MQTT protocols to enable the ESP32 to transmit the ECG data wirelessly to a Node-RED server.

It is important to note that the program for ECG signal preprocessing, including the use of the WT (WaveLib) library, and classification according to the proposed model, was implemented on the ESP32 board. Following this, the results are displayed in Node-RED.

V.3 Developed Electronic Board

In this section, we explore the features of a compact ECG monitoring system, as depicted in Figure V.8. This system is equipped with a small, user-friendly display that allows for real-time visualization of ECG data. It includes an array of operational buttons and LED status indicators that enhance user interaction and provide clear feedback on the

device’s status. The system utilises color-coded electrode leads—red, yellow, and green, which connect to skin-adherent electrodes designed to capture the heart's electrical signals accurately. The device's portable design makes it ideal for patient-operated cardiac monitoring outside traditional clinical environments. Its ease of use not only facilitates routine health management but also empowers patients to actively participate in their cardiac health monitoring. This portable ECG monitor stands out as a valuable tool for continuous cardiac surveillance, potentially reducing the need for frequent clinical visits and allowing for early detection of arrhythmic events.



FigureV.8: The Developed Electronic Board

V.4 Hardware implementation

The proposed system comprises two primary components. The first part involves signal extraction, achieved through the acquisition node, which collects the ECG signal from the human body utilising an AD8232 sensor (Figure V.2). The second part focuses on preprocessing the classified signal, where signal denoising is conducted using the proposed PSO-WT method. Additionally, 2D-DWT is employed for feature extraction, and finally, a CNN model is implemented, all on the ESP32 board.

V.4.1 Acquire and test data

After downloading the proposed implemented models, we conducted real human tests to validate the effectiveness of our models.

In this line of research, one of the essential steps is to create the development environment, which involves installing the Arduino IDE and selecting a DWT library

compatible with the ESP platform. Next, the DWT algorithm is implemented, followed by the implementation of the CNN model. We employed a TinyML approach to facilitate deep learning inference on edge devices.

V.4.2 TensorFlow Lite Model

TinyML applications can be effectively deployed across a range of embedded architectures using TensorFlow Lite (TFLite) [161]. In this project, we utilized TinyML to adapt our initially Keras-trained 2D-CNN TensorFlow model for deployment on the ESP32 microcontroller by converting it into the TensorFlow Lite format (. tflite). This conversion was performed using the TensorFlow Lite Converter, a tool that not only transforms the model from the Protocol Buffer (. pb) format to the more compact TensorFlow Lite Flat Buffer (. tflite) format but also incorporates input quantisation.

Input quantisation significantly reduces the model's memory footprint, which is crucial for its deployment on microcontrollers like the ESP32, known for their limited code memory capacity. This streamlined process ensures that the deployed models are both memory efficient and performance-optimized, making them suitable for real-time applications in edge devices. The use of TFlite thus facilitates the seamless integration of advanced machine learning models into embedded systems, enabling sophisticated computational tasks directly on-device without the need for constant connectivity.

V.4.3 Node-RED Server

IBM introduced the Node-RED server in 2013 as an open-source platform. This versatile tool serves to bridge the gap between the Internet and various applications, APIs, online services, and devices by enabling the linking of predefined nodes or blocks of code to execute tasks directly [162]. Built on JavaScript, a widely used and accessible programming language, Node-RED facilitates swift and straightforward connection of streams through its diverse board nodes. Users can effortlessly deploy their creations in their preferred runtime environments using the web browser-based editor provided by Node-RED, which utilises the JSON file format to save created streams. Importing and exporting these streams for sharing purposes is straightforward.

V.4.3.1 Account Creation on FlowFuse for Node-RED Integration

As delineated in Figure V.9, the process for establishing a user account on FlowFuse, a requisite step to access Node-RED for IoT simulations, commences with the methodical submission of user credentials. This entails entering a unique username, the user's full legal name, a verified email address, and a password of high complexity. The user must then specify the nature of their engagement with the FlowFuse platform, with options like 'Educational Use' indicating a focus on academic pursuits within Node-RED's simulation environment. The subsequent acceptance of FlowFuse's terms, followed by an email verification, culminates in the creation of the user account. This essential procedure paves the way for users to seamlessly navigate into the Node-RED interface and embark on sophisticated IoT modelling and simulation tasks.

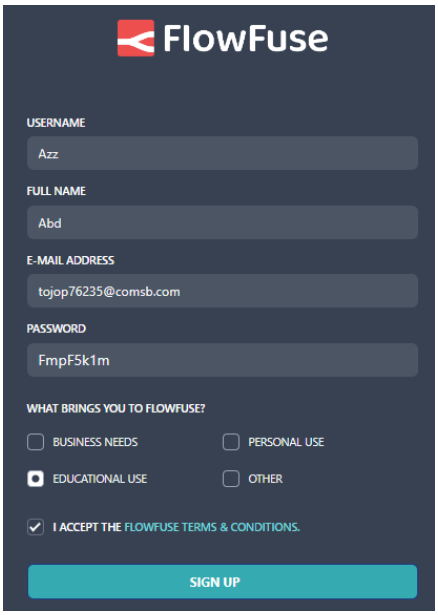


Figure V.9: FlowFuse_account

V.4.3.2 Node-RED Editor

The Node-RED editor window consists of four components (Figure V.10):

- The header at the top.
- The palette on the left.
- The main workspace in the centre.
- The sidebar on the right.

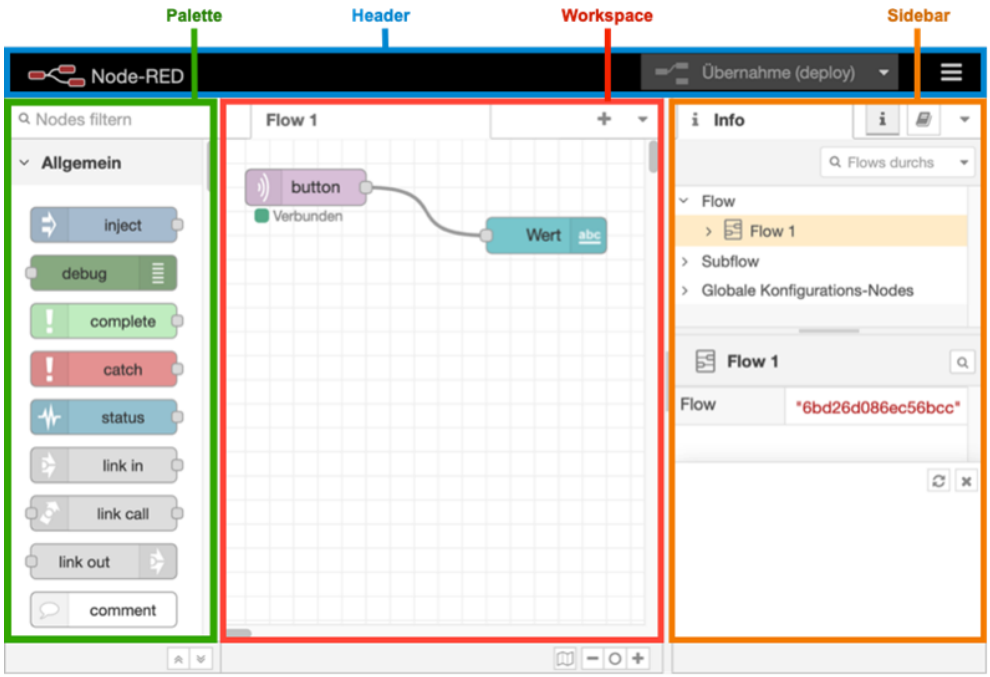


Figure V.10: Node RED Editor

V.4.3.3 Header

The header contains the deploy button, the main menu, and the user menu.

V.4.3.4 Palette

The palette includes all installed and available nodes for use. The palette manager can be utilised to install new nodes. Figure V.11 showcases some modules (sets of nodes) available in Node-RED, such as:

Dashboard: A module that provides a set of nodes (text, gauge, graphs, LED, etc.) in Node-RED to quickly create a real-time data dashboard (to display the status of multiple services).

Input/Outputs: Contains nodes that offer ways to send/receive data over the same set of protocols (e.g., serial, MQTT, HTTP, etc.).

Function: Contains a series of nodes supporting processing functions. This ranges from a simple delay node to a switch node, to a programmable function node that can be adapted to almost any programming need.

Storage: Nodes in this module can be used to read/write data from/to a file or a database (file, MySQL, etc.).

Social: "Social media" nodes support interactions with email, Twitter, Facebook, etc. These nodes allow sending or receiving emails, notifications, tweets.

Nodes are created when a flow is deployed; they can send and receive messages while the flow is running and are deleted when the next flow is deployed. They consist of an HTML file and a JavaScript file. The HTML file dictates what the node should look like, how many inputs/outputs it should use. The JavaScript file is responsible for how the node should function.

V.4.3.5 Workspace

The main workspace is where flows are developed by dragging nodes from the palette and connecting them together.

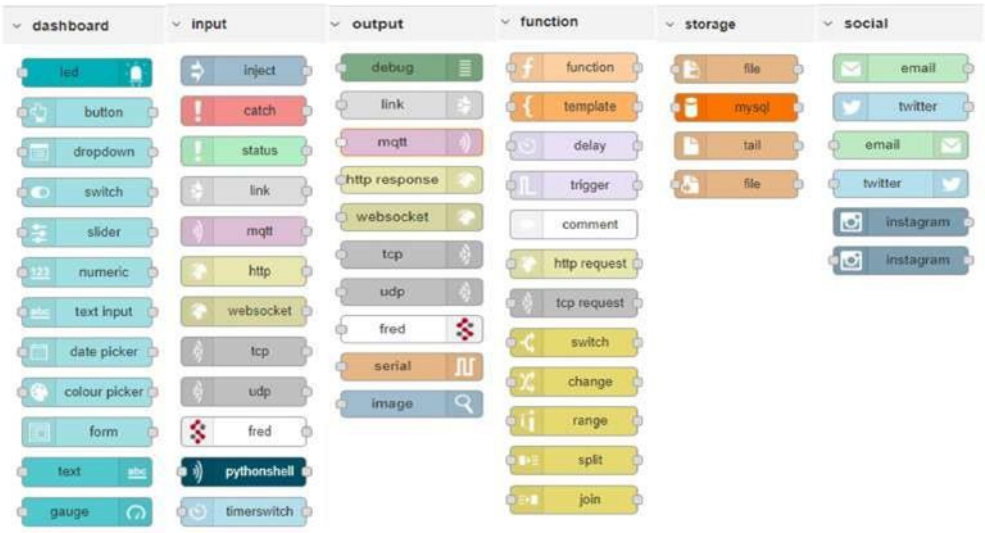


Figure V.11: Examples of nodes that can be found in Node-RED

V.4.3.6 Sidebar

The sidebar contains panels that provide several useful tools within the editor, where:
The info bar displays more information about the currently selected node (a summary of its properties and help texts for the node).
The debug bar shows messages passed to the debug nodes in the flow, as well as some execution log messages.
The configuration nodes bar provides a list of all configuration nodes organized by their scope.
The context bar displays the contents of the context data storage.
Some nodes offer their own sidebar panels, such as node-red-dashboard.

V.4.3.7 Setting Up Node-RED

To set up Node-RED, follow the steps outlined below:

- Install and initiate Node-RED on a suitable platform, such as a Raspberry Pi, a PC, or a cloud server.
- Configure MQTT nodes within Node-RED to subscribe to the topics published by the ESP32.
- Process and visualises the incoming ECG data using Node-RED's function and dashboard nodes.

V.4.3.8 Node-RED Workflow

Figure V.12 outlines a structured workflow for managing ECG data using an ESP32 microcontroller, implemented via the Node-RED programming environment. Initially, raw ECG signals, which typically contain significant noise, are captured and processed through a specific formatting function. This initial processing step transforms these signals into a graphical format, depicted as the 'Noisy Plot,' which visually represents the unfiltered electrical activity of the heart.

Simultaneously, a parallel processing stream applies a noise reduction technique to these raw signals. Post noise-reduction, these signals are formatted using the same function as the raw data to ensure consistency in data handling, resulting in what is referred to as the 'Denoised Plot.' This visual comparison between the 'Noisy' and 'Denoised' plots allows for immediate visual assessment of the noise reduction efficacy.

The final component of this workflow is a sophisticated classification mechanism. This system evaluates the denoised ECG signals and categorizes them into predefined classes based on specific signal characteristics. These categories typically correspond to various cardiac conditions, enabling rapid diagnostic assessments.

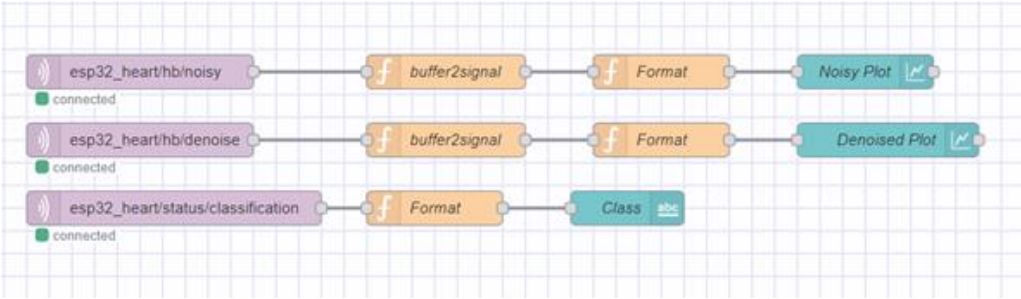


Figure V.12: Workflow for ECG Signal Processing with ESP32 using Node-RED

V.4.3.9 Data Flow:

- The ESP32 continuously reads ECG data from the AD8232 sensor and sends this information over Wi-Fi using MQTT.
- Node-RED receives the data, processes it, and displays it on a real-time dashboard.
- Alerts can be generated based on specific criteria, such as abnormal heart rates, and historical data can be stored in a database for further analysis.

V.5 Diagnostic results

In Figure V.13, we present the diagnostic results obtained using our advanced implemented methodology for monitoring cardiac signals. The left part of the figure depicts a practical application scenario where the developed device is installed on a patient, with data transferred to a laptop. This setup effectively captures the heart signal, which is then processed and displayed in the graphs on the right. The first graph, titled "Heartbeat (noisy)," displays the original signal with a noticeable level of noise. Next, the “Heartbeat (Denoising)” graph below shows the signal after applying the proposed noise reduction technique, highlighting a smoother and more stable waveform. The classification box on the far-right labels the processed signal as “NSR (Normal Sinus Rhythm),” validating the normal heart rhythm after analysis. Collectively, these visual images underscore the efficacy of the proposed method not only in enhancing signal quality through noise suppression but also in accurate signal classification, crucial for reliable detection of heart disease in contemporary healthcare monitoring systems.

In the Node-RED window, two ECG signals are displayed: the first represents the noisy signal captured by the ADC, while the second illustrates the signal after undergoing denoising through the proposed PSO-WT method. These signals are received directly within the Node-RED interface. Additionally, the classification results obtained from the CNN model are presented alongside these signals, providing real-time diagnostic insights within the same interface. This setup offers valuable capabilities for remote healthcare providers to assess patient conditions efficiently and accurately.



Figure V.13: Example of a diagnostic for a person

The data presented in Figure V.14 illustrates a detailed breakdown of execution times for the various stages of the signal processing workflow implemented in this study. A summary of the critical steps and their respective durations are as follows:

```
19:17:41.408 -> DWT2 transform
19:17:41.408 -> Predict with cnn2d model
19:17:42.062 -> Output vector = [ 1.00 0.00 0.00 ]
19:17:42.062 -> Predicted : 0 -> ARR
19:17:42.062 -> Total Execution time       :32018545 us
19:17:42.062 ->    - ADC Aquisition time   :31360274 us
19:17:42.062 ->    - Scaling time          :376 us
19:17:42.062 ->    - Denoising time        :12289 us
19:17:42.062 ->    - DWT2D compute time    :2265 us
19:17:42.062 ->    - Model Prediction time :643341 us
19:17:42.106 -> ********************************************
```

Figure V.14: Detailed Steps and Execution Times

- **Discrete Wavelet Transform (2D DWT):** The initial transformation of the data using the 2D DWT was executed promptly, taking only 0.02 seconds. This efficiency demonstrates the computational effectiveness of the wavelet transform implementation.
- **Convolutional Neural Network (CNN) Prediction:** The core predictive analysis using a 2D CNN model was computed in 0.64 seconds. The rapid processing at this stage is indicative of the model's optimization and the suitability of the architecture for real-time analysis.
- **Output Vector:** The model output a vector [1.00 0.00 0.00], indicating a strong confidence in the first class, which in the context of this study, corresponds to an arrhythmic event (ARR).
- **Total Execution Time:** The complete pipeline from data acquisition to producing a prediction result was 32 seconds.

- **Analog-to-Digital Conversion (ADC):** The most substantial portion of the execution time was consumed by the ADC process, accounting for approximately 31 seconds. This suggests that the data acquisition phase is the primary bottleneck in the current setup.
- **Other Preprocessing Steps:** Additional preprocessing steps, including scaling and denoising, were completed efficiently, totalling approximately 0.13 seconds. These figures reinforce the overall efficiency of the data preprocessing workflow.

From these results, it is evident that the major challenge in the system's performance lies in the data acquisition phase. While the downstream processes, such as the DWT2D computation and CNN prediction, are highly optimized, the ADC process dominates the execution time. Addressing this bottleneck could significantly improve the system's responsiveness, making it more viable for real-time applications. Future work will focus on exploring alternative ADC methods, enhancing parallel processing capabilities, and investigating advanced hardware solutions to alleviate this limitation.

V.6 Conclusion

In conclusion, this chapter presents a comprehensive IoT-based ECG monitoring system that utilises the robust ESP32, the precise AD8232 sensor, and the adaptable Node-RED for efficient real-time heart health tracking. Beyond its foundational strengths, the system incorporates sophisticated denoising techniques like PSO-WT and 2D-WT for meticulous feature extraction, complemented by a 2D-CNN model for accurate ECG signal classification, all seamlessly integrated on the board. Future developments, aiming for enriched data analytics, more intuitive user interfaces, and the addition of diverse health sensors, promise to evolve this setup into an all-encompassing home health monitoring ecosystem. This fusion of IoT with advanced analytical and diagnostic techniques signifies a significant advancement in healthcare technology, offering the potential for enhanced health management and an improved quality of life through innovative home-based health solutions.

Chapter VI

General Conclusion and Perspectives

The research conducted in this thesis aimed to explore the potential of IoT and AI in optimising clinical workflows within various intensive care units and services focused on cardiovascular diseases. Specifically, it sought to enhance predictive capabilities and personalise patient treatments by integrating AI and IoT interventions, utilising available databases such as ECG signals and AI components. The study underscored the growing interest in these technologies within healthcare, particularly in cardiology.

Addressing the challenge of noise interception in ECG signals emerged as a key focus, vital for ensuring the accuracy and reliability of data. Through the utilisation of advanced signal processing techniques and machine learning algorithms, the research aimed to attenuate noise interference and augment the efficacy of AI and IoT interventions, particularly within intensive care units specialising in cardiovascular diseases.

The research provided a nuanced interpretation of results through qualitative and quantitative analyses, drawing from theoretical frameworks and empirical observations. Innovative denoising techniques tailored for ECG signals were developed, integrating advanced signal processing and AI algorithms such as PSO-WT and GA-WT hybrid systems to optimize wavelet transform parameters. These methods aimed to effectively reduce noise interference, thereby enhancing ECG data accuracy and reliability for further analysis. Experimental findings demonstrate that the PSO-WT technique outperforms existing methods in terms of SNR, particularly at 60 Hz, with acceptable performance at 50 Hz. For instance, applying the PSO-WT technique to an ECG signal at an input SNR of 10 dB resulted in an output SNR of 27.47 dB at 60 Hz, significantly improving signal quality suitable for clinical diagnosis. Moreover, the proposed method exhibits promising efficiency in the presence of WGN, highlighting its relevance for IoT applications and RF transmission.

Furthermore, the thesis substantially improves healthcare monitoring systems by focusing on the classification of denoised ECG signals, aiming to elevate accuracy in cardiac anomaly detection, facilitate reliable diagnoses, and enhance overall efficacy of healthcare

monitoring. Using the proposed model, precision scores were remarkably high (0.99 for ARR and NSR, and 0.98 for CHF), recall scores were similarly high (0.99 for ARR, 1.00 for NSR, and slightly lower at 0.96 for CHF), and F1 scores-maintained excellence (0.99 for ARR and NSR, and 0.97 for CHF), confirming balanced accuracy and sensitivity of the model.

Moreover, an IoT-based ECG monitoring system was implemented using ESP32 and deep learning CNN, integrating advanced technologies to enhance remote patient monitoring capabilities and diagnostic accuracy. The results of this research are included in smart e-health applications and smart homes, such as the use of wearable devices integrated with sensors for remote monitoring, further advancing the accessibility and effectiveness of healthcare services

In our forthcoming endeavours, we aim to broaden the applicability of the proposed approach to embedded systems with high computational resources, such as FPGA, enhancing its suitability for IoT-based applications. We will explore Particle Swarm Optimisation Variants, Hybrid Approaches, and Reinforcement Learning techniques to optimise and maximise its performance on embedded systems. Additionally, thorough evaluations in real e-health applications will focus on its effectiveness in filtering ECG signals amidst high-frequency noise, influenced by both hardware and environmental factors. Expanding its scope to encompass biomedical signals like EEG and PCG, we plan to utilise modern optimisation algorithms to fine-tune all WT parameters and implement this method on an FPGA board, facilitating its integration into future medical applications.

Bibliography

[1] S. Tuli, N. Basumatary, S.S. Gill, M. Kahani, R.C. Arya, G.S. Wander, R. Buyya, HealthFog: An ensemble deep learning based Smart Healthcare System for Automatic Diagnosis of Heart Diseases in integrated IoT and fog computing environments, Futur. Gener. Comput. Syst. 104 (2020) 187–200.

[2] B. Bengherbia, M.R.A. Berkani, Z. Achir, A. Tobbal, M. Rebiai, M. Maazouz, Real-Time Smart System for ECG Monitoring Using a One-Dimensional Convolutional Neural Network, in: 2022 Int. Conf. Theor. Appl. Comput. Sci. Eng., 2022: pp. 32–37.

[3] A. Abdallah, B. Billel, A. Nail, S. Abdelkerim, ECG Signal Denoising Based on Wavelet Transform and Genetic Algorithm, in: 2023 Int. Conf. Adv. Electron. Control Commun. Syst., 2023: pp. 1–6. https://doi.org/10.1109/ICAECCS56710.2023.10105043.

[4] Y. Huang, H. Li, X. Yu, A novel time representation input based on deep learning for ECG classification, Biomed. Signal Process. Control. 83 (2023) 104628.

[5] S. Chatterjee, R.S. Thakur, R.N. Yadav, L. Gupta, D.K. Raghuvanshi, Review of noise removal techniques in ECG signals, IET Signal Process. 14 (2020) 569–590.

[6] S. Boda, M. Mahadevappa, P.K. Dutta, A hybrid method for removal of power line interference and baseline wander in ECG signals using EMD and EWT, Biomed. Signal Process. Control. 67 (2021) 102466. https://doi.org/https://doi.org/10.1016/j.bspc.2021.102466.

[7] M. Pham, Y. Mengistu, H. Do, W. Sheng, Delivering home healthcare through a cloud-based smart home environment (CoSHE), Futur. Gener. Comput. Syst. 81 (2018) 129–140.

[8] M.Z. Uddin, A wearable sensor-based activity prediction system to facilitate edge computing in smart healthcare system, J. Parallel Distrib. Comput. 123 (2019) 46–53.

[9] M. Devarajan, V. Subramaniyaswamy, V. Vijayakumar, L. Ravi, Fog-assisted personalized healthcare-support system for remote patients with diabetes, J. Ambient Intell. Humaniz. Comput. 10 (2019) 3747–3760.

[10] S. Sareen, S.K. Gupta, S.K. Sood, An intelligent and secure system for predicting and preventing Zika virus outbreak using Fog computing, Enterp. Inf. Syst. 11 (2017) 1436–1456.

[11] A.A. Abdellatif, A. Mohamed, C.F. Chiasserini, M. Tlili, A. Erbad, Edge computing for smart health: Context-aware approaches, opportunities, and challenges, IEEE Netw. 33 (2019) 196–203.

[12] G. Muhammad, S.K.M.M. Rahman, A. Alelaiwi, A. Alamri, Smart health solution integrating IoT and cloud: A case study of voice pathology monitoring, IEEE Commun. Mag. 55 (2017) 69–73.

[13] M. Bansal, B. Gandhi, IoT & big data in smart healthcare (ECG monitoring), in: 2019 Int. Conf. Mach. Learn. Big Data, Cloud Parallel Comput., 2019: pp. 390–396.

[14] P. Rajpurkar, E. Chen, O. Banerjee, E.J. Topol, AI in health and medicine, Nat. Med. 28 (2022) 31–38.

[15] N.C. Taher, I. Mallat, N. Agoulmine, N. El-Mawass, An IoT-Cloud based solution for real-time and batch processing of big data: Application in healthcare, in: 2019 3rd Int. Conf. Bio-Engineering Smart Technol., 2019: pp. 1–8.

[16] M. Akay, Biomedical signal processing, Academic press, 2012.

[17] D. Mahmood, H.N. Riaz, H. Nisar, Introduction to Non-Invasive Biomedical Signals for Healthcare, in: Adv. Non-Invasive Biomed. Signal Sens. Process. with Mach. Learn., Springer, 2023: pp. 1–24.

[18] M. Kim, S. Jang, D. Lee, S. Lee, J. Gwak, S.C. Jun, J.G. Kim, A comprehensive research setup for monitoring Alzheimer's disease using EEG, fNIRS, and Gait analysis, Biomed. Eng. Lett. (2023) 1–9.

[19] Z.A.A. Alyasseri, A.T. Khader, M.A. Al-Betar, Electroencephalogram signals denoising using various mother wavelet functions: A comparative analysis, in: ACM Int. Conf. Proceeding Ser., Association for Computing Machinery, 2017: pp. 100–105. https://doi.org/10.1145/3132300.3132313.

[20] S. Ismail, B. Ismail, I. Siddiqi, U. Akram, PCG classification through spectrogram using transfer learning, Biomed. Signal Process. Control. 79 (2023) 104075.

[21] W. Zeng, B. Su, C. Yuan, Y. Chen, Automatic detection of heart valve disorders using Teager--Kaiser energy operator, rational-dilation wavelet transform and convolutional neural networks with PCG signals, Artif. Intell. Rev. 56 (2023) 781–806.

[22] S. Ismail, B. Ismail, PCG signal classification using a hybrid multi round transfer learning classifier, Biocybern. Biomed. Eng. 43 (2023) 313–334.

[23] H. Altaheri, G. Muhammad, M. Alsulaiman, S.U. Amin, G.A. Altuwaijri, W. Abdul,

M.A. Bencherif, M. Faisal, Deep learning techniques for classification of electroencephalogram (EEG) motor imagery (MI) signals: A review, Neural Comput. Appl. 35 (2023) 14681–14722.

[24] P.K. Shukla, V. Roy, P.K. Shukla, A.K. Chaturvedi, A.K. Saxena, M. Maheshwari, P.R. Pal, An advanced EEG motion artifacts eradication algorithm, Comput. J. 66 (2023) 429–440.

[25] U. Amin, F.A. Nascimento, I. Karakis, D. Schomer, S.R. Benbadis, Normal variants and artifacts: importance in EEG interpretation, Epileptic Disord. 25 (2023) 591–648.

[26] J. Jeon, H. Cai, Wearable EEG-based construction hazard identification in virtual and real environments: A comparative study, Saf. Sci. 165 (2023) 106213.

[27] S.-N. Chiu, Y.-S. Chen, C.-C. Hsu, Y.-C. Hua, W.-C. Tseng, C.-W. Lu, M.-T. Lin, C.-A. Chen, M.-H. Wu, Y.-T. Chen, others, Changes of ECG parameters after BNT162b2 vaccine in the senior high school students, Eur. J. Pediatr. 182 (2023) 1155–1162.

[28] Y. Weiting, Z. Runjing, An improved self-adaptive filter based on LMS algorithm for filtering 50Hz interference in ECG signals, in: 2007 8th Int. Conf. Electron. Meas. Instruments, 2007: pp. 874–878. https://doi.org/10.1109/ICEMI.2007.4351057.

[29] S. Shadmand, B. Mashoufi, A new personalized ECG signal classification algorithm using Block-based Neural Network and Particle Swarm Optimization, Biomed. Signal Process. Control. 25 (2016) 12–23. https://doi.org/10.1016/j.bspc.2015.10.008.

[30] S. Farashi, A multiresolution time-dependent entropy method for QRS complex detection, Biomed. Signal Process. Control. 24 (2016) 63–71. https://doi.org/10.1016/j.bspc.2015.09.008.

[31] R. Tung, P. Zimetbaum, Use of the Electrocardiogram in Acute Myocardial Infarction, Card. Intensive Care. (2010) 106–109. https://doi.org/10.1016/B978-1-4160-3773-6.10011-4.

[32] H.W. Loh, C.P. Ooi, S.L. Oh, P.D. Barua, Y.R. Tan, F. Molinari, S. March, U.R. Acharya, D.S.S. Fung, Deep neural network technique for automated detection of ADHD and CD using ECG signal, Comput. Methods Programs Biomed. 241 (2023) 107775.

[33] A.H. Kashou, P.A. Noseworthy, T.J. Beckman, N.S. Anavekar, M.W. Cullen, K.B. Angstman, B.J. Sandefur, B.P. Shapiro, B.W. Wiley, A.M. Kates, others, ECG interpretation proficiency of healthcare professionals, Curr. Probl. Cardiol. (2023)

101924.

[34] T.V. Tai, M.P.N. Tan, N.M. Tri, N.V. Ha, T.T.T. Nguyen, A high sensitivity sqi with peak-amplitude difference variance for wearable ecg signals, in: 2023 5th Int. Conf. Bio-Engineering Smart Technol., 2023: pp. 1–4.

[35] N.A. Manlong, J. Rahul, M. Sora, ST Segment Analysis for Early Detection of Myocardial Infarction, Int. J. Comput. Sci. Eng. 6 (2018) 1500–1504.

[36] S. Chatterjee, R.S. Thakur, R.N. Yadav, L. Gupta, D.K. Raghuvanshi, Review of noise removal techniques in ECG signals, IET Signal Process. 14 (2020) 569–590. https://doi.org/10.1049/iet-spr.2020.0104.

[37] A. Azzouz, B. Bengherbia, P. Wira, N. Alaoui, A. Souahlia, The Effectiveness of Optimal Discrete Wavelet Transform Parameters Obtained Using the Genetic Algorithm for ECG Signal Denoising., Rev. d'Intelligence Artif. 37 (2023). https://doi.org/10.18280/ria.370602.

[38] C. Levkov, G. Mihov, R. Ivanov, I. Daskalov, I. Christov, I. Dotsinsky, Removal of power-line interference from the ECG: a review of the subtraction procedure, Biomed. Eng. Online. 4 (2005) 1–18.

[39] E.S.A. El-Dahshan, Genetic algorithm and wavelet hybrid scheme for ECG signal denoising, Telecommun. Syst. 46 (2011) 209–215. https://doi.org/10.1007/s11235-010-9286-2.

[40] J.J. Kok, M.J.G. van de Molengraft, Signal analysis, 2002.

[41] M. Vetterli, J. Kovacevic, V.K. Goyal, Signal processing: Fourier and wavelet representations, Fourier Wavelets. Org, a3. 1 (2012).

[42] D. Gabor, Theory of communication. Part 1: The analysis of information, J. Inst. Electr. Eng. III Radio Commun. Eng. 93 (1946) 429–441.

[43] J. Allen, Short term spectral analysis, synthesis, and modification by discrete Fourier transform, IEEE Trans. Acoust. 25 (1977) 235–238.

[44] I. Firoiu, Complex Wavelet Transform. Application to Denoising, Univ. Politech. Timisoara. (2010).

[45] A. Graps, An introduction to wavelets, IEEE Comput. Sci. Eng. 2 (1995) 50–61.

[46] R.J.E. Merry, Wavelet theory and applications: a literature study, (2005).

[47] O. Rioul, M. Vetterli, Wavelets and signal processing, IEEE Signal Process. Mag. 8 (1991) 14–38.

[48] W. Sweldens, Construction and Applications of wavelets in Numerical Analysis, PhD

thesis, Department of Computer Science, Katholieke Universiteit Leuven~…, 1994.

[49] M.G.E. Schneiders, Wavelets in control engineering, Master's Thesis, Eindhoven Univ. Technol. (2001) 38.

[50] S. Addison Paul, The illustrated wavelet transform handbook: introductory theory and applications in science, engineering, medicine and finance, Institute of Physics publishing, 2002.

[51] Y. Meyer, Ondelettes et op{é}rateurs, I Ondelettes. (1990).

[52] B. Jawerth, W. Sweldens, An overview of wavelet based multiresolution analyses, SIAM Rev. 36 (1994) 377–412.

[53] NAIMI HILAL, Wavelets Transform in the Medical Signal Processing, UNIVERSITY OF ZIANE ACHOUR DJELFA, 2016.

[54] G. Strang, T. Nguyen, Wavelets and filter banks, SIAM, 1996.

[55] C.E. Heil, D.F. Walnut, Continuous and discrete wavelet transforms, SIAM Rev. 31 (1989) 628–666.

[56] H. Nagendra, S. Mukherjee, V. Kumar, Application of wavelet techniques in ECG signal processing: an overview, Int. J. Eng. Sci. Technol. 3 (2011) 7432–7443.

[57] E.S.A. El-Dahshan, Genetic algorithm and wavelet hybrid scheme for ECG signal denoising, Telecommun. Syst. 46 (2011) 209–215. https://doi.org/10.1007/s11235-010-9286-2.

[58] F. Costa, S. Genovesi, M. Borgese, A. Michel, F.A. Dicandia, G. Manara, A review of RFID sensors, the new frontier of internet of things, Sensors. 21 (2021) 3138.

[59] K. Karboub, Contribution à l'amélioration des performances des services médicaux urgents appliquant l'IoT et l'intelligence artificielle, Université de Lorraine, 2022.

[60] E. Borgia, R. Bruno, M. Conti, D. Mascitti, A. Passarella, Mobile edge clouds for information-centric iot services, in: 2016 IEEE Symp. Comput. Commun., 2016: pp. 422–428.

[61] J. Gubbi, R. Buyya, S. Marusic, M. Palaniswami, Internet of Things (IoT): A vision, architectural elements, and future directions, Futur. Gener. Comput. Syst. 29 (2013) 1645–1660.

[62] D.G.S. Pivoto, L.F.F. de Almeida, R. da Rosa Righi, J.J.P.C. Rodrigues, A.B. Lugli, A.M. Alberti, Cyber-physical systems architectures for industrial internet of things applications in Industry 4.0: A literature review, J. Manuf. Syst. 58 (2021) 176–192.

[63] P.K. Malik, N. Bilandi, A. Gupta, others, Narrow band-IoT and long-range

technology of IoT smart communication: Designs and challenges, Comput. Ind. Eng. 172 (2022) 108572.

[64] D.S. Rajput, R. Gour, An IoT framework for healthcare monitoring systems, Int. J. Comput. Sci. Inf. Secur. 14 (2016).

[65] K. Kang, J. Lin, J. Zhang, BIM-and IoT-based monitoring framework for building performance management, J. Struct. Integr. Maint. 3 (2018) 254–261.

[66] N. Naik, Choice of effective messaging protocols for IoT systems: MQTT, CoAP, AMQP and HTTP, in: 2017 IEEE Int. Syst. Eng. Symp., 2017: pp. 1–7.

[67] M. Bansal, Priya, Performance comparison of MQTT and CoAP protocols in different simulation environments, Inven. Commun. Comput. Technol. Proc. ICICCT 2020. (2021) 549–560.

[68] Y. Chen, T. Kunz, Performance evaluation of IoT protocols under a constrained wireless access network, in: 2016 Int. Conf. Sel. Top. Mob. Wirel. Netw., 2016: pp. 1–7.

[69] M. Younan, E.H. Houssein, M. Elhoseny, A.A. Ali, Challenges and recommended technologies for the industrial internet of things: A comprehensive review, Measurement. 151 (2020) 107198.

[70] A. Protopsaltis, P. Sarigiannidis, D. Margounakis, A. Lytos, Data visualization in internet of things: tools, methodologies, and challenges, in: Proc. 15th Int. Conf. Availability, Reliab. Secur., 2020: pp. 1–11.

[71] X. Xu, S. Huang, Y. Chen, K. Browny, I. Halilovicy, W. Lu, TSAaaS: Time series analytics as a service on IoT, in: 2014 IEEE Int. Conf. Web Serv., 2014: pp. 249–256.

[72] L. Lan, R. Shi, B. Wang, L. Zhang, J. Shi, A lightweight time series main-memory database for IoT real-time services, in: Internet Veh. Technol. Serv. Towar. Smart Cities 6th Int. Conf. IOV 2019, Kaohsiung, Taiwan, Novemb. 18--21, 2019, Proc. 6, 2020: pp. 220–236.

[73] F. Gessert, W. Wingerath, S. Friedrich, N. Ritter, NoSQL database systems: a survey and decision guidance, Comput. Sci. Dev. 32 (2017) 353–365.

[74] M. Stonebraker, Errors in database systems, eventual consistency, and the cap theorem, Commun. ACM, BLOG@ ACM. (2010).

[75] R. Patra, M. Bhattacharya, S. Mukherjee, IoT-based computational frameworks in disease prediction and healthcare management: Strategies, challenges, and potential, IoT Healthc. Ambient Assist. Living. (2021) 17–41.

[76] M. Zhang, M. Luo, R. Nie, Y. Zhang, Technical attributes, health attribute, consumer attributes and their roles in adoption intention of healthcare wearable technology, Int. J. Med. Inform. 108 (2017) 97–109.

[77] S. Mishra, B.K. Mishra, H.K. Tripathy, A. Dutta, Analysis of the role and scope of big data analytics with IoT in health care domain, in: Handb. Data Sci. Approaches Biomed. Eng., Elsevier, 2020: pp. 1–23.

[78] S.G. Zen, M. Dachyar, Intensive care unit (ICU) patient monitoring improvement using Internet of Things (IoT) based on BPR approach, in: Proc. 11th Annu. Int. Conf. Ind. Eng. Oper. Manag., 2021: pp. 1572–1583.

[79] L. Blonde, K. Khunti, S.B. Harris, C. Meizinger, N.S. Skolnik, Interpretation and impact of real-world clinical data for the practicing clinician, Adv. Ther. 35 (2018) 1763–1774.

[80] I. Subramanian, S. Verma, S. Kumar, A. Jere, K. Anamika, Multi-omics data integration, interpretation, and its application, Bioinform. Biol. Insights. 14 (2020) 1177932219899051.

[81] N. Mehta, A. Pandit, S. Shukla, Transforming healthcare with big data analytics and artificial intelligence: A systematic mapping study, J. Biomed. Inform. 100 (2019) 103311.

[82] L. Bote-Curiel, S. Munoz-Romero, A. Gerrero-Curieses, J.L. Rojo-Álvarez, Deep learning and big data in healthcare: a double review for critical beginners, Appl. Sci. 9 (2019) 2331.

[83] R. Williams, E. Kontopantelis, I. Buchan, N. Peek, Clinical code set engineering for reusing EHR data for research: a review, J. Biomed. Inform. 70 (2017) 1–13.

[84] C.S. Kruse, A. Stein, H. Thomas, H. Kaur, The use of electronic health records to support population health: a systematic review of the literature, J. Med. Syst. 42 (2018) 1–16.

[85] S.A. Senthilkumar, B.K. Rai, A.A. Meshram, A. Gunasekaran, S. Chandrakumarmangalam, Big data in healthcare management: a review of literature, Am. J. Theor. Appl. Bus. 4 (2018) 57–69.

[86] S. Dash, S.K. Shakyawar, M. Sharma, S. Kaushik, Big data in healthcare: management, analysis and future prospects, J. Big Data. 6 (2019) 1–25.

[87] R. Miotto, F. Wang, S. Wang, X. Jiang, J.T. Dudley, Deep learning for healthcare: review, opportunities and challenges, Brief. Bioinform. 19 (2018) 1236–1246.

[88] L.P. Malasinghe, N. Ramzan, K. Dahal, Remote patient monitoring: a comprehensive study, J. Ambient Intell. Humaniz. Comput. 10 (2019) 57–76.

[89] B. Noah, M.S. Keller, S. Mosadeghi, L. Stein, S. Johl, S. Delshad, V.C. Tashjian, D. Lew, J.T. Kwan, A. Jusufagic, others, Impact of remote patient monitoring on clinical outcomes: an updated meta-analysis of randomized controlled trials, NPJ Digit. Med. 1 (2018) 20172.

[90] L.H. Schwamm, N. Chumbler, E. Brown, G.C. Fonarow, D. Berube, K. Nystrom, R. Suter, M. Zavala, D. Polsky, K. Radhakrishnan, others, Recommendations for the implementation of telehealth in cardiovascular and stroke care: a policy statement from the American Heart Association, Circulation. 135 (2017) e24--e44.

[91] D. Apiletti, E. Baralis, G. Bruno, T. Cerquitelli, Real-time analysis of physiological data to support medical applications, IEEE Trans. Inf. Technol. Biomed. 13 (2009) 313–321.

[92] M. Al-Khafajiy, T. Baker, C. Chalmers, M. Asim, H. Kolivand, M. Fahim, A. Waraich, Remote health monitoring of elderly through wearable sensors, Multimed. Tools Appl. 78 (2019) 24681–24706.

[93] H. Mora, D. Gil, R. Munoz Terol, J. Azor'\in, J. Szymanski, An IoT-based computational framework for healthcare monitoring in mobile environments, Sensors. 17 (2017) 2302.

[94] S. Lee, C. Vinegoni, P.F. Feruglio, L. Fexon, R. Gorbatov, M. Pivoravov, A. Sbarbati, M. Nahrendorf, R. Weissleder, Real-time in vivo imaging of the beating mouse heart at microscopic resolution, Nat. Commun. 3 (2012) 1054.

[95] J. Dyro, Clinical engineering handbook, Elsevier, 2004.

[96] S. Moradian, M.K. Krzyzanowska, R. Maguire, P.P. Morita, V. Kukreti, J. Avery, G. Liu, J. Cafazzo, D. Howell, others, Usability evaluation of a mobile phone--based system for remote monitoring and management of chemotherapy-related side effects in cancer patients: mixed-methods study, JMIR Cancer. 4 (2018) e10932.

[97] N. El-Rashidy, S. El-Sappagh, S.M.R. Islam, H. M. El-Bakry, S. Abdelrazek, Mobile health in remote patient monitoring for chronic diseases: Principles, trends, and challenges, Diagnostics. 11 (2021) 607.

[98] M.G. Dickinson, L.A. Allen, N.A. Albert, T. DiSalvo, G.A. Ewald, A.R. Vest, D.J. Whellan, M.R. Zile, M.M. Givertz, Remote monitoring of patients with heart failure: a white paper from the Heart Failure Society of America Scientific Statements

Committee, J. Card. Fail. 24 (2018) 682–694.

[99] M.A. Uddin, A. Stranieri, I. Gondal, V. Balasubramanian, Continuous patient monitoring with a patient centric agent: A block architecture, IEEE Access. 6 (2018) 32700–32726.

[100] S. Khalilpourazari, S. Khalilpourazary, Optimization of production time in the multi-pass milling process via a Robust Grey Wolf Optimizer, Neural Comput. Appl. 29 (2018) 1321–1336.

[101] R. Faturechi, E. Miller-Hooks, A mathematical framework for quantifying and optimizing protective actions for civil infrastructure systems, Comput. Civ. Infrastruct. Eng. 29 (2014) 572–589.

[102] Y. Zhang, L. Wang, Y. Gao, J. Chen, X. Shi, Noise reduction in Doppler ultrasound signals using an adaptive decomposition algorithm, Med. Eng. Phys. 29 (2007) 699–707.

[103] S. Khalilpourazari, A. Arshadi Khamseh, Bi-objective emergency blood supply chain network design in earthquake considering earthquake magnitude: a comprehensive study with real world application, Ann. Oper. Res. 283 (2019) 355–393.

[104] W. Zhang, Z. Lin, X. Liu, Short-term offshore wind power forecasting - A hybrid model based on Discrete Wavelet Transform (DWT), Seasonal Autoregressive Integrated Moving Average (SARIMA), and deep-learning-based Long Short-Term Memory (LSTM), Renew. Energy. 185 (2022) 611–628. https://doi.org/10.1016/j.renene.2021.12.100.

[105] M. Rouis, S. Sbaa, N.E. Benhassine, The effectiveness of the choice of criteria on the stationary and non-stationary noise removal in the phonocardiogram (PCG) signal using discrete wavelet transform, Biomed. Tech. 65 (2020) 353–366. https://doi.org/10.1515/bmt-2019-0197.

[106] Z.A.A. Alyasseri, A.T. Khader, M.A. Al-Betar, Electroencephalogram signals denoising using various mother wavelet functions: A comparative analysis, ACM Int. Conf. Proceeding Ser. Part F1313 (2017) 100–105. https://doi.org/10.1145/3132300.3132313.

[107] C. Sawant, H.T. Patii, Wavelet based ECG signal de-noising, in: 1st Int. Conf. Networks Soft Comput. ICNSC 2014 - Proc., 2014: pp. 20–24. https://doi.org/10.1109/CNSC.2014.6906684.

[108] M. Rakshit, S. Das, An efficient ECG denoising methodology using empirical mode

decomposition and adaptive switching mean filter, Biomed. Signal Process. Control. 40 (2018) 140–148. https://doi.org/10.1016/j.bspc.2017.09.020.

[109] D.L. Donoho, J.M. Johnstone, Ideal spatial adaptation by wavelet shrinkage, Biometrika. 81 (1994) 425–455. https://doi.org/10.1093/biomet/81.3.425.

[110] B.N. Singh, A.K. Tiwari, Optimal selection of wavelet basis function applied to ECG signal denoising, Digit. Signal Process. 16 (2006) 275–287. https://doi.org/10.1016/j.dsp.2005.12.003.

[111] A. Azzouz, B. Bengherbia, P. Wira, N. Alaoui, A. Souahlia, M. Maazouz, H. Hentabeli, An efficient ECG signals denoising technique based on the combination of particle swarm optimisation and wavelet transform, Heliyon. (2024) e26171. https://doi.org/https://doi.org/10.1016/j.heliyon.2024.e26171.

[112] Z.A.A. Alyasseri, A.T. Khader, M.A. Al-Betar, A.K. Abasi, S.N. Makhadmeh, EEG Signals Denoising Using Optimal Wavelet Transform Hybridized with Efficient Metaheuristic Methods, IEEE Access. 8 (2020) 10584–10605. https://doi.org/10.1109/ACCESS.2019.2962658.

[113] B.N. Singh, A.K. Tiwari, Optimal selection of wavelet basis function applied to ECG signal denoising, Digit. Signal Process. A Rev. J. 16 (2006) 275–287. https://doi.org/10.1016/j.dsp.2005.12.003.

[114] D.L. Donoho, De-noising by soft-thresholding, IEEE Trans. Inf. Theory. 41 (1995) 613–627. https://doi.org/10.1109/18.382009.

[115] L.-K. Shark, C. Yu, Design of optimal shift-invariant orthonormal wavelet filter banks via genetic algorithm, Signal Processing. 83 (2003) 2579–2591.

[116] A.R.F. da Silva, Evolutionary-based methods for adaptive signal representation, Signal Processing. 81 (2001) 927–944.

[117] R. Poli, J. Kennedy, T. Blackwell, Quantification & Assessment of the chemical form of residual gadolinium in the brain, Swarm Intell. 1 (2007) 33–57. https://doi.org/10.1007/s11721-007-0002-0.

[118] D. Wang, D. Tan, L. Liu, Particle swarm optimization algorithm: an overview, Soft Comput. 22 (2018) 387–408. https://doi.org/10.1007/s00500-016-2474-6.

[119] Healthcare data, volume glo (n.d.).

[120] S. Shilo, H. Rossman, E. Segal, Axes of a revolution: challenges and promises of big data in healthcare, Nat. Med. 26 (2020) 29–38.

[121] A. Kaplan, M. Haenlein, Siri, Siri, in my hand: Who's the fairest in the land? On the

interpretations, illustrations, and implications of artificial intelligence, Bus. Horiz. 62 (2019) 15–25.

[122] A. Burkov, The hundred-page machine learning book, Andriy Burkov Quebec City, QC, Canada, 2019.

[123] B. Mahesh, Machine learning algorithms-a review, Int. J. Sci. Res. (IJSR).[Internet]. 9 (2020) 381–386.

[124] A. Voulodimos, N. Doulamis, A. Doulamis, E. Protopapadakis, others, Deep learning for computer vision: A brief review, Comput. Intell. Neurosci. 2018 (2018).

[125] X.-W. Chen, X. Lin, Big data deep learning: challenges and perspectives, IEEE Access. 2 (2014) 514–525.

[126] W. Wang, M. Zhang, G. Chen, H. V Jagadish, B.C. Ooi, K.-L. Tan, Database meets deep learning: Challenges and opportunities, ACM Sigmod Rec. 45 (2016) 17–22.

[127] T.O. Ayodele, Types of machine learning algorithms, New Adv. Mach. Learn. 3 (2010) 1–5.

[128] A.K. Jain, J. Mao, K.M. Mohiuddin, Artificial neural networks: A tutorial, Computer (Long. Beach. Calif). 29 (1996) 31–44.

[129] M. Chen, U. Challita, W. Saad, C. Yin, M. Debbah, Artificial neural networks-based machine learning for wireless networks: A tutorial, IEEE Commun. Surv. Tutorials. 21 (2019) 3039–3071.

[130] F. Emmert-Streib, Z. Yang, H. Feng, S. Tripathi, M. Dehmer, An introductory review of deep learning for prediction models with big data, Front. Artif. Intell. 3 (2020) 4.

[131] S. Sharma, S. Sharma, A. Athaiya, Activation functions in neural networks, Towar. Data Sci. 6 (2017) 310–316.

[132] K. Fukushima, A self-organizing neural network model for a mechanism of pattern recognition unaffected by shift in position, Biol, Cybern. 36 (1980) 193–202.

[133] A. Krizhevsky, I. Sutskever, G.E. Hinton, Imagenet classification with deep convolutional neural networks, Adv. Neural Inf. Process. Syst. 25 (2012).

[134] M. Vakalopoulou, S. Christodoulidis, N. Burgos, O. Colliot, V. Lepetit, Deep learning: basics and convolutional neural networks (CNNs), Mach. Learn. Brain Disord. (2023) 77–115.

[135] A. Araujo, W. Norris, J. Sim, Computing receptive fields of convolutional neural networks, Distill. 4 (2019) e21.

[136] Y. LeCun, B. Boser, J.S. Denker, D. Henderson, R.E. Howard, W. Hubbard, L.D.

Jackel, Backpropagation applied to handwritten zip code recognition, Neural Comput. 1 (1989) 541–551.

[137] Y. GAFOUR, Apprentissage automatique pour une classification des images basée sur les descripteurs, Université Djillali Liabes, 2020.

[138] T. Fawcett, R.O.C. Graphs, Notes and practical considerations for data mining researchers, Hewlett-Packard Co. (2003).

[139] M.A. Kabir, C. Shahnaz, Denoising of ECG signals based on noise reduction algorithms in EMD and wavelet domains, Biomed. Signal Process. Control. 7 (2012) 481–489. https://doi.org/10.1016/j.bspc.2011.11.003.

[140] MIT-BIH database, (2023). http://www.physionet.org/physiobank/database/mitdb (accessed September 15, 2023).

[141] V. Prasad, P. Siddaiah, B.P. Rao, A new wavelet based method for denoising of biological signals, Int. J. Comput. Sci. Netw. Secur. 8 (2008) 238–244.

[142] S. Kumar, D. Panigrahy, P.K. Sahu, Denoising of Electrocardiogram (ECG) signal by using empirical mode decomposition (EMD) with non-local mean (NLM) technique, Biocybern. Biomed. Eng. 38 (2018) 297–312. https://doi.org/10.1016/j.bbe.2018.01.005.

[143] S.L. Joshi, R.A. Vatti, R. V Tornekar, A survey on ECG signal denoising techniques, in: 2013 Int. Conf. Commun. Syst. Netw. Technol., 2013: pp. 60–64. https://doi.org/10.1109/CSNT.2013.22.

[144] B.H. Tracey, E.L. Miller, Nonlocal means denoising of ECG signals, IEEE Trans. Biomed. Eng. 59 (2012) 2383–2386. https://doi.org/10.1109/TBME.2012.2208964.

[145] S. Samadi, M.B. Shamsollahi, ECG noise reduction using empirical mode decomposition based on combination of instantaneous half period and soft-thresholding, Middle East Conf. Biomed. Eng. MECBME. (2014) 244–248. https://doi.org/10.1109/MECBME.2014.6783250.

[146] A. Chacko, S. Ari, Denoising of ECG signals using Empirical Mode Decomposition based technique, IEEE-International Conf. Adv. Eng. Sci. Manag. ICAESM-2012. 2 (2012) 6–9.

[147] M. Rakshit, S. Das, An efficient ECG denoising methodology using empirical mode decomposition and adaptive switching mean filter, Biomed. Signal Process. Control. 40 (2018) 140–148. https://doi.org/10.1016/j.bspc.2017.09.020.

[148] R.N. Vargas, A.C.P. Veiga, Electrocardiogram signal denoising by clustering and soft

thresholding, IET Signal Process. 12 (2018) 1165–1171. https://doi.org/10.1049/iet-spr.2018.5162.

[149] G. Han, Z. Xu, Electrocardiogram signal denoising based on a new improved wavelet thresholding, Rev. Sci. Instrum. 87 (2016) 1–7. https://doi.org/10.1063/1.4960411.

[150] L. Condat, A direct algorithm for 1-D total variation denoising, IEEE Signal Process. Lett. 20 (2013) 1054–1057. https://doi.org/10.1109/LSP.2013.2278339.

[151] R.N. Vargas, A.C.P. Veiga, Electrocardiogram signal denoising by a new noise variation estimate, Res. Biomed. Eng. 36 (2020) 13–20. https://doi.org/10.1007/s42600-019-00033-y.

[152] R.R. Sharma, R.B. Pachori, Baseline wander and power line interference removal from ECG signals using eigenvalue decomposition, Biomed. Signal Process. Control. 45 (2018) 33–49. https://doi.org/10.1016/j.bspc.2018.05.002.

[153] M.R. Keshtkaran, Z. Yang, A fast, robust algorithm for power line interference cancellation in neural recording, J. Neural Eng. 11 (2014) 1–18. https://doi.org/10.1088/1741-2560/11/2/026017.

[154] S. Agrawal, A. Gupta, Fractal and EMD based removal of baseline wander and powerline interference from ECG signals, Comput. Biol. Med. 43 (2013) 1889–1899. https://doi.org/http://dx.doi.org/10.1016/j.compbiomed.2013.07.030.

[155] R.N. Vargas, A.C.P. Veiga, Electrocardiogram signal denoising by a new noise variation estimate, Res. Biomed. Eng. 36 (2020) 13–20. https://doi.org/10.1007/s42600-019-00033-y.

[156] M. Garc'\ia, M. Mart'\inez-Iniesta, J. Ródenas, J.J. Rieta, R. Alcaraz, A novel wavelet-based filtering strategy to remove powerline interference from electrocardiograms with atrial fibrillation, Physiol. Meas. 39 (2018) 115006.

[157] L. Condat, A direct algorithm for 1-D total variation denoising, IEEE Signal Process. Lett. 20 (2013) 1054–1057. https://doi.org/10.1109/LSP.2013.2278339.

[158] S. Agrawal, A. Gupta, Fractal and EMD based removal of baseline wander and powerline interference from ECG signals, Comput. Biol. Med. 43 (2013) 1889–1899. https://doi.org/10.1016/j.compbiomed.2013.07.030.

[159] S.G. Mallat, A theory for multiresolution signal decomposition: the wavelet representation, IEEE Trans. Pattern Anal. Mach. Intell. 11 (1989) 674–693.

[160] O.K. Al-Shaykh, I. Moccagatta, H. Chen, JPEG-2000: A new still image compression standard, in: Conf. Rec. Thirty-Second Asilomar Conf. Signals, Syst. Comput. (Cat.

No. 98CH36284), 1998: pp. 99–103.

[161] P.P. Ray, A review on TinyML: State-of-the-art and prospects, J. King Saud Univ. Inf. Sci. 34 (2022) 1595–1623.

[162] Node-RED, (2024) [Online]. https://nodered.org/ (accessed February 20, 2024).